Thesis

Theoretical Study of Scanning Tunneling Microscopy
based on
## First-Principles Electronic Structure Calculation

第一原理的な電子状態計算に基づく
走査トンネル顕微鏡の理論的研究

Katsuyoshi Kobayashi

小林 功佳

Department of Physics
Faculty of Science
University of Tokyo

March 1994

Thesis

Theoretical Study of Scanning Tunneling Microscopy based on First-Principles Electronic Structure Calculation

Katsuyoshi Kobayashi

Department of Physics
Faculty of Science
University of Tokyo

March 1994

Acknowledgments

Contents

1

Chapter 1

Introduction

Scanning tunneling microscopy (STM) invented by Binnig and Rohrer has provided great progress in surface science[1]. The STM has made it possible for the first time to obtain direct images of surfaces with atomic resolution. A famous application of the STM is the determination of the atomic structure of Si(111)7×7 surface[2]. By a detailed comparison between experimental and theoretical STM images, the dimer-adatom-stacking fault (DAS) model[3] was established as the structure of this complicated surface [4]. Nowadays, the STM is used in various fields of surface science and is opening a revolutionary stage[5,6].

One of the distinctive features of the STM is an ability to obtain a real-space image of surfaces. This has enlarged application fields of the STM not only to ordered surfaces but also to such irregular structures as surfaces with local defects, surface steps, and surfaces adsorbed with adatoms and molecules[7]-[13]. The STM is effectively used in the study of crystal growth on atomic level[14]-[19]. Furthermore, it is surprising that STM images can be obtained even in air[20] and in aqueous solution[21] with atomic resolution. This has made it possible to apply the STM to the study of electrochemistry[22] and biology[23]-[28]. Atomic images can be obtained even for insulating surfaces by means of force between surfaces and tips. This method is called atomic force microscopy (AFM)[29]. The STM image is obtained also by light emission from the tunneling junction[30]-[32] and by nonlinear response in laser-assisted tunneling[33,34]. Recently, by using the STM tip as a tool like a *pincette*, surface modification on the

atomic level has come true[35]-[44].

Though the STM provides atomic images of surfaces, interpretation of the images is not trivial. Tersoff and Hamann showed that the STM observes not the atomic structure of surfaces but the electronic states near the Fermi level[45]. Their result is quite reasonable, because the STM is based on the tunneling process of electrons. This fact has been evidently demonstrated by the STM images of graphite surface[46]-[49] and Si(111)$\sqrt{3}\times\sqrt{3}$-Ag surface[50,51]. An extension of the Tersoff and Hamann's theory means that local density of states (LDOS) of a surface is obtained by varying bias voltage with keeping the STM tip at a position over the surface. This method is named local tunneling spectroscopy (LTS) or, more generally, scanning tunneling spectroscopy (STS). The STM is an unique and fundamentally important method for obtaining information of surface wavefunctions on the atomic level.

The Tersoff and Hamann's theory has succeeded in qualitative interpretations of STM images on various surfaces, but there are some effects which are neglected in their theory. Among them, effect of tip is important. Since an apex of an actual tip is formed of several atoms, atomic and electronic structure of the tip may influence STM images. Lang, using a single atom tip attached to a jellium surface, showed that STM images change qualitatively depending on kind of the tip atom[52]-[58]. Chen investigated the case that wavefunction of the tip is not s-wave[59]-[62]. Ciraci et $al.$ calculated electronic structure of systems consisting of the single atom tip and a surface, and investigated influence of the tip on the electronic states of the sample surface[63]-[66].

For investigating the effect of the electronic and atomic structure of actual tips explicitly, a method for calculating STM images has been developed [67]-[74]. This method is based on the first-principles calculation of the electronic structure of the tip as well as of the sample surface. The method was applied first to graphite surface, and it was clarified that an interference effect of the tip and surface wavefunctions is essential for the appearance of anomalous STM images observed on graphite surface[67]-[71]. In this thesis, this method is described, and the STM images and STS

spectra of graphite surface are discussed in detail. This method was also applied to a study of the negative differential resistance (NDR) observed on Si(111)$\sqrt{3}\times\sqrt{3}$-B surface[75,76]. From calculations of the STS spectra on this surface, it has been clarified that, as well as a defect level of the sample surface, a tunnel-active orbital of the tip is necessary for the appearance of the NDR[72,73]. In this thesis, a detail is presented.

STM images of organic molecules weakly adsorbed on surfaces show strange and interesting properties. In the STM of liquid crystals adsorbed on graphite surface, the image of the liquid crystals disappears completely, and the image of the underlayer graphite is observed at a certain bias voltage[77]. This "transparency" effect has been explained by a resonant tunneling effect[77] or by a matching of phase shift of the surface wavefunctions[78]. For transition-metal dichalcogenides[79,80] and graphite intercalation compounds (GIC's)[81]-[83], it has not been settled yet whether first or second layer is observed in their STM images.

In the case of lattice-mismatched systems between adsorbed layers and substrates, modulated structures with long periods often appear in STM images. The "moiré pattern" has been observed on the surfaces of monolayer graphite on metal substrates[84] and transition-metal dichalcogenides[85]-[87]. The observations of the modulated structure in the STM suggest that electronic structure of the overlayers is perturbed by influence of substrates and changed into one different from an isolated layer. In this thesis, electronic structure of the monolayer graphite on TiC(111) surface is investigated and the STM image with the modulated structure is discussed.

Organization of the present thesis is as follows. In chapter 2, a brief review of theories of the STM is presented. In chapter 3, the method for calculating the electronic structure and the STM image is shown, which is applied to the bulk graphite surface and the Si(111)$\sqrt{3}\times\sqrt{3}$-B surface in chapter 4 and 5, respectively. The electronic structure and STM image of the monolayer graphite on TiC(111) surface is presented in chapter 6. Finally, conclusions of the present thesis are stated in chapter 7.

Chapter 2

Brief review of theory of STM

Principle of the STM is quite simple. When a tip is put close to a sample surface, electrons in the tip jump into the sample by the tunneling effect. The tunneling current I is roughly estimated as

$$I \propto \exp(-2\lambda d), \tag{2.1}$$

where

$$\lambda \equiv \sqrt{\frac{2mW}{\hbar}}, \tag{2.2}$$

and d is the distance between the tip and the sample. In the above, m and W are mass of an electron and work function of the sample, respectively. By virtue of the exponential dependence of the tunneling current on tip-sample distance, the tunneling current in scanning the tip over the sample surface is very sensitive to unevenness of the sample surface. This property makes it possible to obtain a surface image with atomic resolution.

The question "What is observed by the STM ?" was answered by Tersoff and Hamann[45]. They assumed a spherical tip model and considered only the s-wave for the tip wavefunction like

$$\psi_\mu(\mathbf{r}) \sim \frac{1}{|\mathbf{r} - \mathbf{r}_0|} \exp(-\kappa|\mathbf{r} - \mathbf{r}_0|), \tag{2.3}$$

where $\mathbf{r}_0$ is the center of the spherical tip. Using Bardeen's formula[88] for the tunneling current, the tunneling current I for small bias voltage V is given as

$$I \propto V\rho(\mathbf{r}_0, E_F), \tag{2.4}$$

$\times 10^8$

TIP SAMPLE

PIEZO
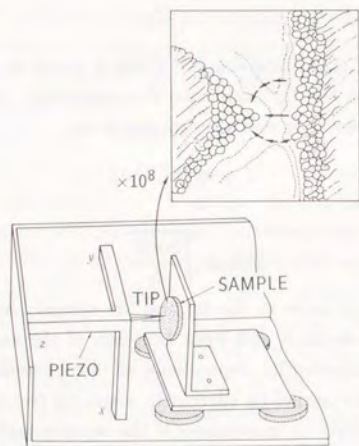
Figure 2.1: Schematic picture of STM.

$$\rho(\mathbf{r}, E) \equiv \sum_i |\Psi_i(\mathbf{r})|^2 \delta(E - E_i). \qquad (2.5)$$

In the above, $\rho(\mathbf{r}, E)$, $\Psi_i(\mathbf{r})$, and E_F are local density of states (LDOS) of surface, surface wavefunction with energy E_i, and Fermi energy, respectively. By scanning the tip over the sample surface, namely, by moving the tip center $\mathbf{r}_0$, a map of the surface LDOS can be obtained. This is the interpretation of STM image in the Tersoff-Hamann's theory.

If electronic structure of the tip can be ignored, a simple extension of the Tersoff-Hamann's formula for a finite bias voltage is given as

$$\frac{dI(V)}{dV} \propto \rho(\mathbf{r}_0, E_F + eV), \qquad (2.6)$$

and therefore

$$I(V) \propto \int_{E_F}^{E_F+eV} dE \rho(\mathbf{r}_0, E). \qquad (2.7)$$

Equation (2.6) means that, by fixing the tip position at a point over the surface and by varying the bias voltage, a local spectrum of the surface is obtained. This method is termed scanning tunneling spectroscopy (STS). The formula derived by Tersoff and Hamann implies that the STM observes not the atomic image but the electronic states of surface. This fact has been evidently demonstrated by the STM image of graphite surface. The STS provides information on kind of atoms adsorbed on surfaces and is useful for the study of surface chemistry[7]-[13].

Though the Tersoff and Hamann's theory has succeeded in qualitative interpretation of STM images and STS spectra of many surfaces, there are some important effects neglected in their theory. The effect of tip is often crucial. Since an apex of an actual tip consists of several atoms, the atomic and electronic structure of the tip may influence the STM and STS. For investigating the effect of the electronic and atomic structure of the tip, we need to go back to the Bardeen's formula.

When the tip-sample distance is large enough to look upon the tip-sample interaction as a small perturbation, the tunneling current is given by Bardeen as[88]

$$I = \frac{2\pi e}{\hbar} \sum_{\mu, \nu} \{f(E_\mu) - f(E_\nu)\} |M_{\mu\nu}|^2 \delta(E_\mu - E_\nu + eV), \qquad (2.8)$$

$$M_{\mu\nu} \equiv \frac{\hbar^2}{2m} \int_S d\mathbf{S} \cdot (\psi_\mu^* \nabla \psi_\nu - \psi_\nu \nabla \psi_\mu^*), \qquad (2.9)$$

where f is Fermi distribution function, and ψ_μ and ψ_ν are wavefunctions of the sample surface and the tip, respectively. The integration is performed over an arbitrary plane S which divides the tunneling gap into the tip and sample regions. The wavefunctions ψ_μ, ψ_ν are eigenfunctions of the isolated sample and tip system, and are solved independently.

Using the Bardeen's formula, Lang investigated STM images of an individual atom with a realistic single-atom tip[52]-[58]. Lang modeled both the tip and the sample surface with an atom adsorbed on an jellium surface. Figure 2.2(a) shows the corrugation of sample surfaces calculated with a Na atom tip. The corrugation is much large for the Na adatom sample than for the S adatom sample, because density of states (DOS) at the Fermi level is larger for the Na sample than the S sample. In the case of He sample surface, the corrugation curve shows negative displacement. This means that the STM image shows a dark spot at the position of He atom. Lang compared the tip displacement with LDOS at the Fermi level and total electronic charge density. Figure 2.2(b) shows the comparison for the Na adatom sample with the Na atom tip. Agreement among the three curves is very good. For the case of the Na sample surface with the Na tip, the STM image can be approximated by the surface LDOS and total charge density.

However, not all STM images observed are explained in terms of the surface LDOS. For example, the corrugation of such metal surfaces as Au, Al, and Cu calculated by the surface LDOS is too small to distinguish individual atoms, but atomic images of these surfaces are actually obtained in experiments. Chen explained this contradiction by considering that actually used tip is such metals with d orbital as W, Pt, and Ir. Chen extended the Tersoff-Hamann theory to non s-wave tip, and found a derivative rule[59]-[62]. The derivative rule means that, for example, first and second derivative of the surface LDOS are obtained by p- and d-wave of the tip wavefunction, respectively. Using the derivative rule, Chen showed that the corrugation of metal surfaces with the d-wave tip is enhanced by a factor of 20 com-
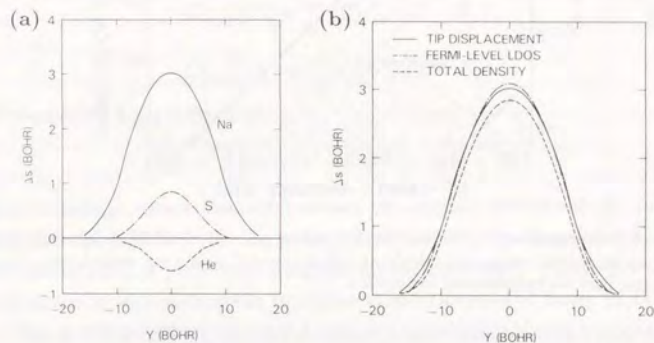

Figure 2.2: (a) Change in tip distance Δs vs. lateral separation Y in constant current mode calculated by Lang[53]. Tip adatom is Na, and sample adatoms are Na, S, and He. (b) Comparison of the tip-displacement curve from (a) with contours of constant LDOS at the Fermi level and total electronic charge density for the Na adatom sample and tip.
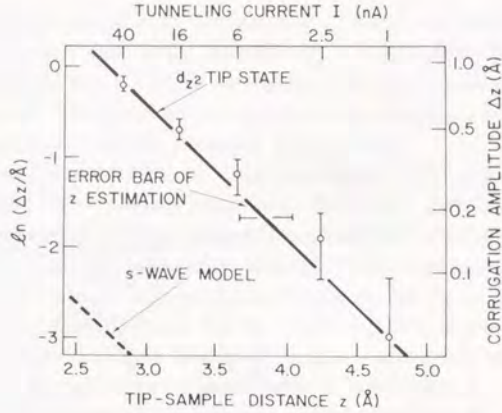
Figure 2.3: Corrugation amplitude of Al(111) surface given by Chen[61]. Solid and dashed curve are theoretical corrugation calculated with d-wave and s-wave tip, respectively. Circles with error bars are experimental corrugation.

pared with one estimated with the surface LDOS[61]. Figure 2.3 shows the corrugation calculated by Chen using the d-wave tip. The calculated result explains well the experimental one.

The above theoretical works are based on the single-atom tip model. For investigating effects of more realistic tip than the single-atom tip, it is useful to model the tip protrusion with a cluster of several atoms. In this case, it is convenient to express the Bardeen's formula with linear combination of atomic orbitals (LCAO)[89]. When the wavefunctions are expanded in terms of surface atomic orbital ϕ_p and tip atomic orbital χ_q as

$$\psi_\mu = \sum_{i,p} a_{ip}^\mu \phi_p(\mathbf{r} - \mathbf{R}_i), \tag{2.10}$$

$$\psi_\nu = \sum_{j,q} a_{jq}^\nu \chi_q(\mathbf{r} - \mathbf{R}_j), \tag{2.11}$$

the tunneling current shown in eq. (2.8) is rewritten as (see Appendix A)

$$I(V) = \frac{2\pi e}{\hbar} \int_{-\infty}^{\infty} dE \{ f(E) - f(E - eV) \}$$

$$\times \sum_{i,i'} \sum_{j,j'} \sum_{p,p'} \sum_{q,q'} G_{ip,i'p'}^{S}(E) G_{j'q',jq}^{T}(E - eV) C_{ipjq} C_{i'p'j'q'}^*. \tag{2.12}$$

In the above, p and q denote sort of the atomic orbitals centered at $\mathbf{R}_i$ and $\mathbf{R}_j$. $G_{ip,i'p'}^{S}(E)$ and $G_{jq,j'p'}^{T}(E)$ are imaginary part of the Green's functions of the surface and the tip defined respectively as

$$G_{ip,i'p'}^{S}(E) \equiv \sum_\mu a_{ip}^{\mu*} a_{i'p'}^{\mu} \delta(E - E_\mu), \tag{2.13}$$

$$G_{j'q',jq}^{T}(E) \equiv \sum_\nu a_{j'q'}^{\nu*} a_{jq}^{\nu} \delta(E - E_\nu). \tag{2.14}$$

The quantity C_{ipjq} defined as

$$C_{ipjq} \equiv \int_{\Omega_T} d\mathbf{r} \phi_p^*(\mathbf{r} - \mathbf{R}_i) V_T(\mathbf{r}) \chi_q(\mathbf{r} - \mathbf{R}_j), \tag{2.15}$$

is a tunneling matrix element between the atomic orbitals of the surface and the tip, and $V_T(\mathbf{r})$ is the potential part of the tip Hamiltonian. The volume integral is performed over the tip region Ω_T[89]. Figure 2.4 shows a diagram for calculating the tunneling current expressed in eq. (2.12).

This method was applied first to graphite surface as shown in this thesis [67]-[70]. The calculated STM image reproduced well experimental one. It was also found that amount of the current tunneling from the apex atom of the tip to the sample is considerably larger than that from the atoms in second layer of the tip[71]. It was concluded that the large sphere-model picture for the tip proposed by Tersoff and Hamann neglecting the atomic structure is not valid, and most of the tunneling current flows through the apex atom of the tip.

This result means that the STM and STS is sensitive to the atomic and electronic structure of the tip apex. Actually, effects of the tip are evident in the anomalous STM images of graphite surface[67]-[71], where it has been found that an interference effect between the tip and surface wavefunctions is essential for the appearance of the anomalous images. In the STS also, there are some cases where the tip effect is essentially important[68]. In
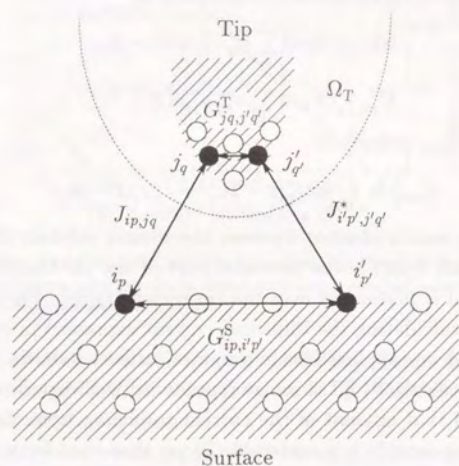
Figure 2.4: Diagram for calculating the tunneling current shown in eq. (2.12)

the STS of Si(111)$\sqrt{3} \times \sqrt{3}$-B surface, the negative differential resistance (NDR) was observed[75,76]. The NDR cannot be explained by the Tersoff and Hamann's theory, because the LDOS is always positive. A simulation taking into account the electronic structure of the tip showed that the NDR is caused by a resonant-tunneling effect between two levels; one is localized at a defect site of the sample surface and the other is a tunnel-active orbital of the tip[72,73].

A disadvantage of the LCAO formalism is that the surface wavefunction is not accurately expressed in the vacuum region. To improve the representation of the tail part of the surface wavefunction, a connected-vacuum-tail (CVT) method was proposed, and was applied to Si(100) surfaces[90,91].

When the tip-surface distance is short, the Bardeen's formalism is not valid. In such a case, tip and sample surface should be treated as a combined system[63]-[66]. This approach is important for investigating the electron tunneling in a high electric field and the atom transfer between tip and sample[92]-[98]. These problems should be solved in future.

Chapter 3

Method of calculation of electronic structure and STM image

3.1 Band calculation

In this thesis, STM images and STS spectra are calculated based on first-principles calculations of the electronic structure for surfaces and tips. For this purpose, the discrete variational $X\alpha$ (DV-$X\alpha$) method with the LCAO basis is employed[99]-[102]. This method is a kind of first-principles methods based on the density functional formalism[103,104], where calculations of the electronic states are reduced to solving the Kohn-Sham equation self-consistently with the local density approximation (LDA) expressed in the atomic unit as

$$\{-\frac{1}{2}\nabla^2 - \sum_m \frac{Z_m}{|\mathbf{r} - \mathbf{R}_m|} + \int \frac{\rho(\mathbf{r}')}{|\mathbf{r} - \mathbf{r}'|} d\mathbf{r}' + V_{\mathrm{XC}}[\rho(\mathbf{r})]\}\psi_n(\mathbf{r}) = \varepsilon_n \psi_n(\mathbf{r}), \quad (3.1)$$

where Z_m is the nuclear charge of an atom situated at a site $\mathbf{R}_m$. V_{XC} is the local exchange-correlation potential which is expressed in the $X\alpha$ form as

$$V_{\mathrm{XC}}[\rho(\mathbf{r})] = -3\alpha(\frac{3\rho(\mathbf{r})}{8\pi})^{1/3}, \quad (3.2)$$

where α is taken to be 0.7. The charge density $\rho(\mathbf{r})$ is calculated from the wavefunctions as

$$\rho(\mathbf{r}) = \sum_n^{\prime} |\psi_n(\mathbf{r})|^2. \quad (3.3)$$

In the above, the prime denotes that the sum is taken over occupies states.

In the LCAO scheme, the wavefunction is expanded in terms of atomic orbitals $\phi_{m\mu}(\mathbf{r})$ as

$$\psi_n(\mathbf{r}) = \sum_{m\mu} C_{n,m\mu}\phi_{m\mu}(\mathbf{r} - \mathbf{R}_m), \qquad (3.4)$$

where μ expresses kind of the atomic orbital.

The atomic orbitals are obtained by solving the Kohn-Sham equation for the atom. In the atom, the charge density is spherically averaged around center of the atom, and the Kohn-Sham equation is reduced into an one-dimensional differential equation for radial wavefunction, which is solved numerically.

Using the above atomic orbital bases, matrix elements of the Hamiltonian in the Kohn-Sham equation are calculated. In this procedure, three-dimensional integration takes much computational time. In the DV-Xα method, the integration is performed by summing up values at pseudo-random sampling points. The sampling points are distributed according to the Fermi distribution function around the atomic sites and to the constant distribution in the interatomic regions. About 300 points per atom are found to be enough to evaluate the matrix elements. This method makes it possible to evaluate the matrix element with much shorter computational time than that by the analytical method using gaussian basis functions and, therefore, it is suitable for performing electronic structure calculations of rather large systems with many atoms in an unit cell.

A shortcoming of this method is lack in a subtle accuracy to evaluate a total energy of the system. This prevents determination of stable structure of the system. However, it is accurate enough to discuss band structures fixing the atomic positions, and is employed in this thesis.

3.2 STM calculation

For calculating the tunneling current in the STM and STS, the simplest method is the use of the Tersoff and Hamann's formula and its extension shown in eqs. (2.6) and (2.7). The STM images and STS spectra are obtained from only LDOS of sample surface. However, for investigating the effects of tip, these formulae are inadequate, and the tunneling current should be calculated by the formula shown in eq. (2.12). In this thesis, the calculation of the STM and STS using eq. (2.12) have been performed for bulk graphite and Si(111)$\sqrt{3} \times \sqrt{3}$-B surface.

The Green's functions of the sample and tip in eq. (2.12) are obtained from results of the first-principles band calculations or cluster calculations described above. The tunneling matrix element in eq. (2.15) is calculated analytically by fitting both the atomic orbitals of the surface and tip, and the potential of the tip with several gaussian type orbitals. From five to eight gaussians are used for fitting an atomic orbital.

Most experimental STM images are taken in constant current mode, where topographies of surfaces are obtained by variation of the tip height during a scan with fixing amount of the tunneling current. However, it takes much computational time to calculate an STM image by the constant current mode. Therefore, STM images in this thesis are calculated by variable current mode, where the topographies are obtained by variation of the tunneling current in scanning the tip on a plane over a sample surface. STM images in the constant current mode and in the variable current mode do not differ qualitatively[71].

In the case of the bulk graphite surface, various models for the tip are employed. First, a simple model consisting of only two s-waves like a H_2 molecule is used. Calculated STM images show a drastic effect of the tip. By an analytical calculation, it is proved that this result is caused by an interference effect between the surface and tip wavefunctions. To confirm that this effect occurs actually, STM images are calculated with realistic tip clusters such as $W_{10}[111]$, $W_{14}[110]$, and $Pt_{10}[111]$. The structures of these clusters are assumed to be the same as those quarried out from their bulk forms. Electronic structure of these clusters are calculated by the DV-Xα method.

In the case of the Si(111)$\sqrt{3} \times \sqrt{3}$-B surface, a cluster is used as the model for the surface, and its electronic structure is solved by the DV-Xα method. For the model of the tip, the $W_{10}[111]$, $W_{14}[110]$, and $Pt_{10}[111]$ clusters are used.

In the case of the monolayer graphite on TiC(111) surface, the tunneling current is evaluated from the simple formula with the surface LDOS shown in eqs. (2.6) and (2.7). This is because effects of the tip are not important in STM images of this surface. Influence of the tip would appear quantitatively in such values as corrugation.

Chapter 4

STM and STS of bulk graphite surface

4.1 Introduction

Since the first report by Binnig *et al.*[105], there have been accumulated a number of works on the STM image of graphite surface. This is because an atomically smooth surface of graphite can be easily prepared. The atomic image of graphite surface can be readily obtained by the STM even in air[20] and in water[21] as well as by the AFM[106]. Graphite is often used as a standard specimen for the STM apparatus.

Graphite is a prototype of layered materials and have been studied extensively. Figure 4.1 shows atomic structure and first Brillouin zone of graphite. In-plane atomic structure of graphite forms a honeycomb lattice organized of strong C-C bond. Compared with the in-plane bond, interlayer binding is negligibly weak. This results in the highly anisotropic properties of graphite.

Electronic structure of graphite can be understood, in the first-order approximation, by a single-layer model neglecting the interlayer interaction [107]. Figure 4.2 shows a band structure of the single-layer graphite. The valence bands of the two-dimensional graphite consist of two kinds of bands. One is σ band which is constituted by the sp^2 hybridization of $2s$ and $2p$ orbitals. Remaining $2p$ orbital is made up into π band. The bonding and anti-bonding π band touch at the K points of Brillouin zone. At zero temperature, the bonding π band is completely occupied with electrons and

(a)

(b)

a : 2.456 Å
c : 6.696 Å

● A CARBONS
○ B CARBONS
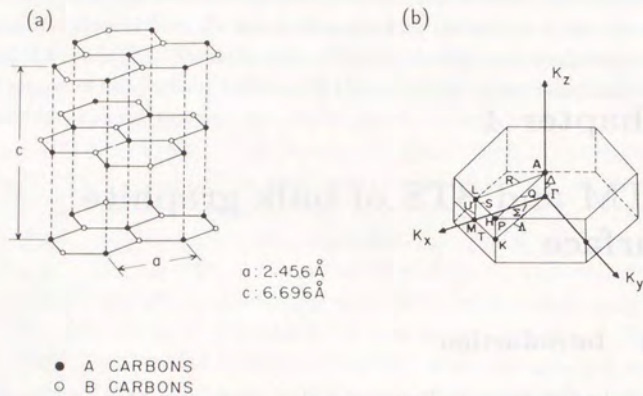
Figure 4.1: (a) atomic structure and (b) Brillouin zone of graphite[109].

the anti-bonding π band is completely empty. Density of states (DOS) of the π bands is also shown in Fig. 4.3. Corresponding to the linear dispersion near the K point, the DOS shows a liner feature near the Fermi level. The DOS diverges logarithmically at energies ± 1, corresponding to the van Hove singularity at the M point of the π band. The DOS is constant at the top and bottom, showing the two-dimensional character. The two-dimensional graphite is a zero-gap semiconductor.

When the interlayer interaction is introduced for describing the three-dimensional graphite, the bonding and the anti-bonding π band are mixed into the electron- and hole-like bands. The electronic structure of a real graphite is semimetal, which is evident in the transport and magnetic properties[108]-[113].

The importance of the interlayer interaction is obvious in the STM image of graphite. Figure 4.4(a) shows an experimental STM image of graphite surface. The STM image is formed of a triangular-lattice structure which is different from one expected from the honeycomb atomic structure. The bright spots in the STM image are β site, where α and β site denote inequiv-
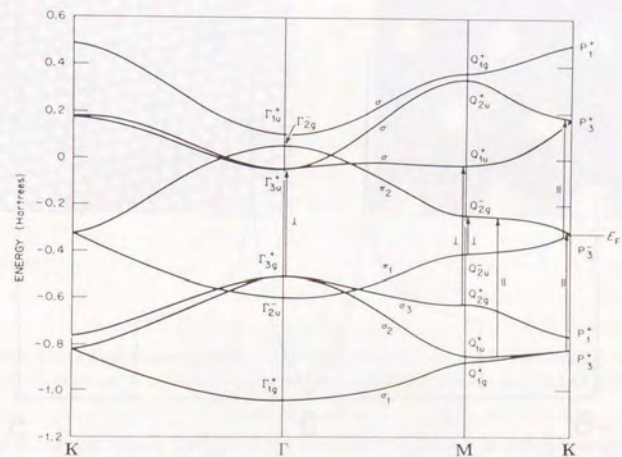
Figure 4.2: Band structure of graphite calculated by Painter and Ellis[107]
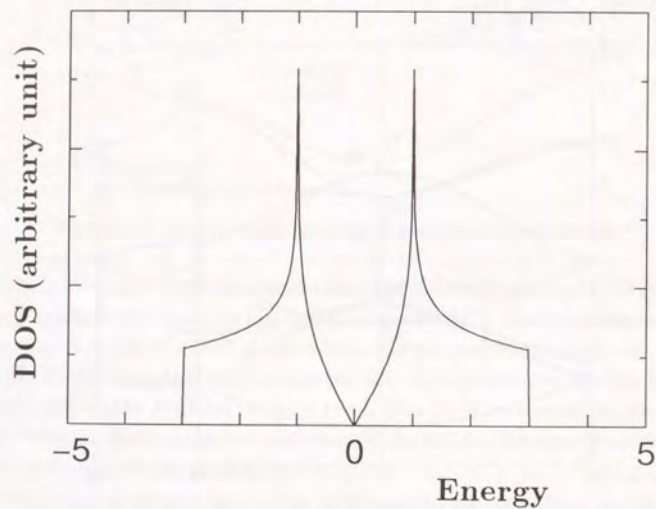
Figure 4.3: DOS of π bands of graphite calculated with a simple tight-binding model. The energy scale is shown in unit of π-orbital transfer energy.
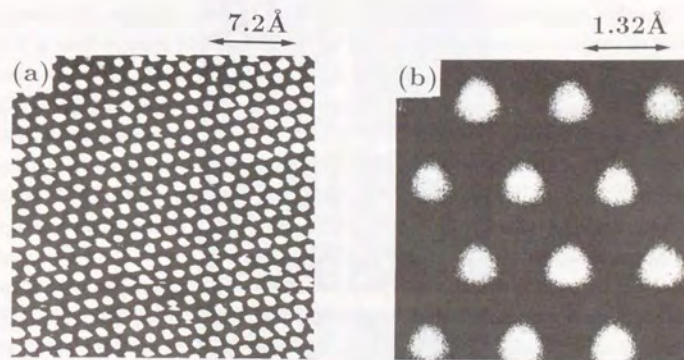
Figure 4.4: (a) Typical experimental STM image of pristine graphite surface[122]. (b) Theoretical STM image of pristine graphite surface calculated with the surface LDOS[48].

alent C atoms which have and do not have C atoms in neighboring layers just above and below them, respectively. This result was rather strange at first sight, but has been explained simply by the fact that the STM does not observe the geometric structure of surfaces but the electronic structure near the Fermi level[46]-[49]. Figure 4.4(b) shows the STM image calculated by Tománek and Louie with the surface LDOS using eq. (2.7). The theoretical image reproduces well the experimental one.

The STM image of graphite shows several strange properties. Corrugation in the STM image of graphite is anomalously large. For this fact, two explanations have been proposed. One is the nodal structure of the wavefunctions of graphite at the Fermi level[114]. The other is an elastic

deformation of the graphite layer by the tip during a scan[115,116]. It has not been settled yet which is more responsible for the anomalous corrugation.

Another remarkable feature in the STM image of graphite is the observations of various anomalous images[117,118]. The STM images near a local defect[119] and a step edge[120,121] show superstructures. On the terrace of graphite surface, drastically deformed patterns are often observed. Figure 4.5 shows examples of the anomalous STM image observed on graphite surface. They are like an array of ridges and have no trace of the atomic structure of graphite. Mizes *et al.* explained these anomalous STM images by a multiple-tip effect[122]. The multiple-tip effect appears when a sample surface is scanned by a tip with several microscopic apexes. The STM image observed by such a tip shows superposition of identical images with a lateral shift corresponding to the distance between the apexes[120],[123]-[125]. Mizes *et al.* extended the Tersoff and Hamann's theory and explained the anomalous image phenomenolagically by simple superposition of the normal images. However, their explanation is based on a phenomenological argument, and microscopic origin of the anomalous images is not clear.

In this chapter, STM images of graphite surface are presented. They are calculated with a direct consideration of the tip wavefunctions by use of the cluster models. An important result is that the anomalous images are not explained by simple superposition, and that an interference effect of the wavefunctions between the surface and the tip is indispensable.

4.2 H_2 tip

First, STM images of graphite surface are calculated by using the bonding and anti-bonding orbital of a hydrogen molecule for the model of the tip orbital. They are the simplest orbitals which do not have the spherical symmetry assumed in the Tersoff and Hamann's theory. Of course, these models are too simple and unrealistic, but they are useful for investigating qualitatively what happens when the tip does not have the spherical symmetry. As shown later, results obtained by the H_2 tip are confirmed
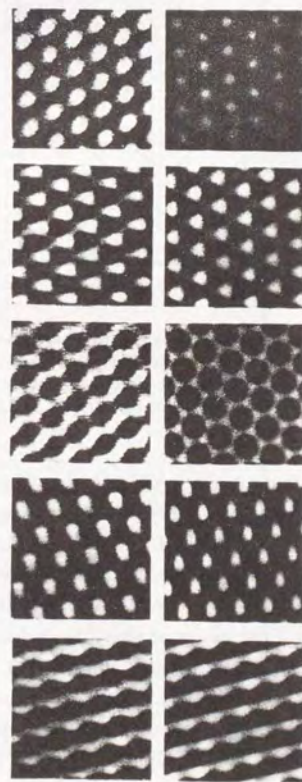
Figure 4.5: Anomalous STM images of graphite surface by Mizes *et al.*[122]. The figures in the left-hand column are experimental images. The figures in the right-hand column are calculated images corresponding to the left-hand experimental ones.
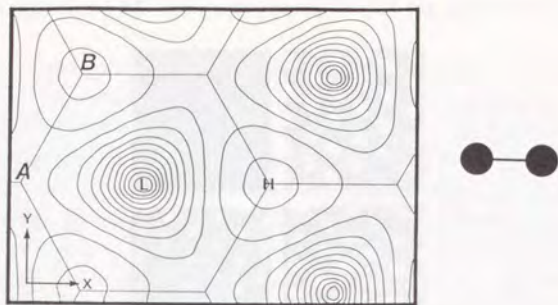
Figure 4.6: Calculated STM image of graphite surface when tip wavefunction is the bonding orbital. The tip is situated 2.6 Å above the graphite surface. Axis of the tip orbital is parallel to the x-axis. A and B denote the α and the β site of graphite lattice. H and L are the largest and the smallest region of the tunneling current. At the right hand side of the image, the H_2 tip is shown in the same scale.

by calculations using more realistic tip models. The tunneling current is calculated by the formula in eq. (2.12). The electronic structure of graphite is calculated by the DV-Xα method. The band calculation is performed for a three-dimensional bulk graphite, because the electronic structure of a graphite surface is not so different from that of a bulk graphite.

Figure 4.6 shows an STM image of graphite surface calculated with the bonding orbital of the H_2 tip. The tip is situated 2.6 Å above the graphite surface. Direction of the H_2 molecule is parallel to the x-axis shown in the figure. Peaks of the tunneling current form a triangular lattice consisting of the β site of graphite. This is almost the same as the normal image shown in Fig. 4.4. Influence of the non-spherical tip appears in a slight elongation along the direction of the tip axis. The scarce influence of the tip asymmetry is mainly due to the non-nodal character of the bonding orbital.

In the case of a nodal tip wavefunction, the STM image is changed drasti-
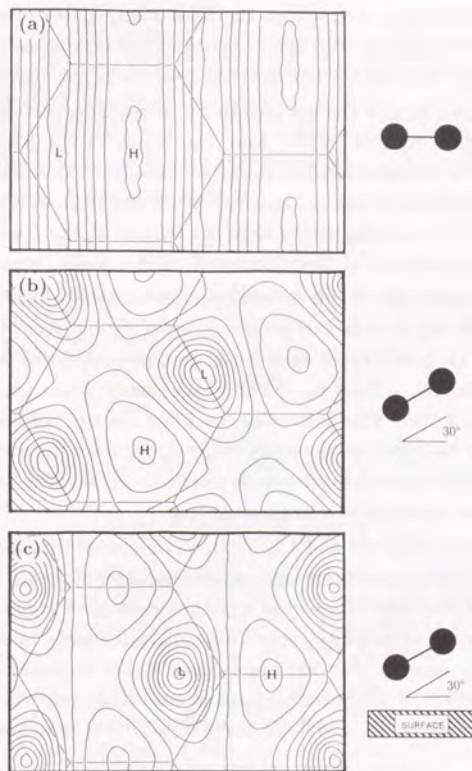

Figure 4.7: Calculated STM image of graphite surface when the tip wavefunction is the anti-bonding orbital. Angles between the tip axis and the x-axis in the figure is 0° for (a) and (c), and 30° for (b). Angles between the tip axis and the surface is 0° for (a) and (b), and 30° for (c). At the right hand side of the images, the H_2 tip is shown in the same scale.

cally. Figure 4.7 shows the STM images of graphite surface calculated with the anti-bonding orbital of the H_2 tip. When the axis of the tip is parallel to the x-axis as shown in Fig. 4.7(a), the STM image shows a stripe pattern. Most of the contour lines run from the top to the bottom perpendicular to the x-axis, and the β site is not the peak position of the tunneling current.

The obtained images change sensitively to the direction of the H_2 axis. When the tip is rotated by 30° from the x-axis in the plain parallel to the surface, the triangular-lattice image is obtained as shown in Fig. 4.7(b). This image is similar to one in Fig. 4.6, but is different from it in points that the peaks of the tunneling current are not located at the β site of graphite and that the direction of the elongation of the peaks, which shows the deviation from the three-fold symmetry, is not parallel but perpendicular to the H_2 axis.

When the H_2 axis is tilted against the graphite surface by 30° with keeping parallel to the x-axis, the STM image shows a triangular lattice as shown in Fig. 4.7(c). This is because, by tiling the tip, the contribution to the tunneling current from the atom of the tip far from the surface becomes smaller than that from the other atom nearer to the surface. In such a case, the tip can be regarded as a single-atom one.

By comparing Figs. 4.6 and 4.7, it can be concluded that the STM image of graphite surface depends strongly on the character of the tip wavefunction and, different from the Mizes *et al.*'s phenomenological argument[122], the anomalous image of graphite cannot be explained simply by superposition of the normal images. For the appearance of the anomalous images, an interference effect of the wavefunctions is essentially important. This can be shown directly by an analytical calculation shown as follows.

4.3 Three waves approximation

Any wavefunction ψ_S of a surface tailing into vacuum can be expanded in terms of two-dimensional plane waves multiplied by a decaying factor $F(z)$

as

$$\psi_S = e^{i\mathbf{k}_\parallel \cdot \mathbf{r}_\parallel} \sum_{\mathbf{G}_\parallel} A(\mathbf{G}_\parallel) e^{i\mathbf{G}_\parallel \cdot \mathbf{r}_\parallel} F(z), \tag{4.1}$$

where $\mathbf{k}_\parallel = (k_x, k_y)$, $\mathbf{G}_\parallel = (G_x, G_y)$, and $\mathbf{r}_\parallel = (x, y)$ are a two-dimensional wave vector, a reciprocal lattice vector, and the coordinate parallel to the surface. Since the Fermi level of graphite is located at the K point in the two-dimensional Brillouin zone and the components with a large lateral momentum decay faster in the vacuum region, the STM image of graphite consists mainly of three waves given by

$$\mathbf{k}_\parallel + \mathbf{G}_\parallel = (0, -\frac{\sqrt{3}}{3}), (\pm\frac{1}{2}, \frac{\sqrt{3}}{6}), \tag{4.2}$$

in an unit of the primitive reciprocal lattice vector. By this simplification, the tunneling current I with the H_2 tip is calculated as (see Appendix B)

$$I \propto I_S \pm I_T, \tag{4.3}$$

where

$$I_S \equiv 3 + 2\cos(\frac{x_0}{2} + \frac{\sqrt{3}}{2}y_0)\cos(\frac{d_x}{4} + \frac{\sqrt{3}}{4}d_y)$$

$$+2\cos(\frac{x_0}{2} - \frac{\sqrt{3}}{2}y_0)\cos(\frac{d_x}{4} - \frac{\sqrt{3}}{4}d_y)$$

$$+ 2\cos x_0 \cos\frac{d_x}{2}, \tag{4.4}$$

$$I_T \equiv 2\cos\frac{d_x}{2}\cos(\frac{\sqrt{3}}{6}d_y) + \cos(\frac{2\sqrt{3}}{3}d_y)$$

$$+2\cos(\frac{x_0}{2} + \frac{\sqrt{3}}{2}y_0)\cos(\frac{d_x}{4} - \frac{\sqrt{3}}{12}d_y)$$

$$+2\cos(\frac{x_0}{2} - \frac{\sqrt{3}}{2}y_0)\cos(\frac{d_x}{4} + \frac{\sqrt{3}}{12}d_y)$$

$$+ 2\cos x_0 \cos(\frac{\sqrt{3}}{6}d_y), \tag{4.5}$$

where (x_0, y_0) and (d_x, d_y) are center of the H_2 molecule and displacement of a hydrogen atom measured from the other atom of H_2, respectively. The sign $+$ or $-$ in eq. (4.3) indicates the bonding or the anti-bonding orbital

of H_2. The term I_S is a simple sum of the contributions from each atom of H_2. The term I_T is an off-diagonal one caused by interference of the surface and tip wavefunctions.

From eqs. (4.4) and (4.5), it is easily shown that the tunneling current for the anti-bonding orbital is a function of only x_0 for a special case with $d_y = 0$. This corresponds to the situation of Fig. 4.7(a), and explains the stripe pattern.

When the tip is rotated by 30° in the surface plane, the tunneling current for the anti-bonding orbital is expressed in a form as

$$I = A + B \cos \frac{y_0'}{2} \cos \frac{\sqrt{3}}{2} x_0' + C \cos y_0', \qquad (4.6)$$

where A, B and C are functions of only the tip length d and can be regarded as constants in scanning the tip over the surface. The x' and the y' axis are defined as ones parallel and perpendicular to the tip axis, respectively. The form of the tunneling current in eq. (4.6) is the same as that calculated with the bonding orbital with $d_y = 0$, which is written as

$$I = A' + B' \cos \frac{x_0}{2} \cos \frac{\sqrt{3}}{2} y_0 + C' \cos x_0. \qquad (4.7)$$

This explains the triangular-lattice image obtained with the anti-bonding orbital shown in Fig. 4.7(b). Furthermore, the interchange of x_0-axis and y_0-axis between eq. (4.6) and eq. (4.7) explains the direction of the elongation deviated from the three fold symmetry in Fig. 4.7(b); the elongation is not parallel but perpendicular to the tip axis.

Since the results obtained by this analytical calculation do not depend on the parameter d which is the separation of the two atoms in H_2 molecule, the essential features would be unchanged for a realistic tip if the orbital active in tunneling has a nodal structure. For a realistic tip such as tungsten, this condition would be realized when the tunneling current flows through the d_{xz} ($z \perp$ surface) orbital localized on an apex atom of protrusion of the tip. This has been verified by performing a calculation with an use of a realistic model for the tip as shown in the next paragraph.

[1 1 1]
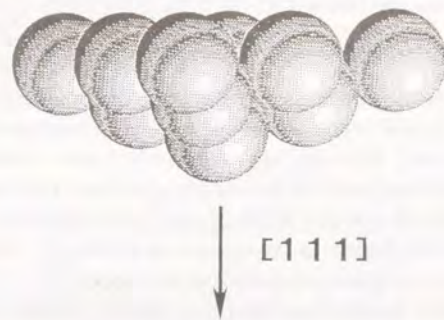
Figure 4.8: W_{10} cluster used as a model of tip.

4.4 First-principles calculation of STM image

In actual experiments of the STM, such metals as tungsten and platinum are used as materials for the tip. The microscopic structure of the tip apex is not characterized except for a few cases using field ion microscopy (FIM)[126,127]. Therefore, various clusters are used as the model of the tip in the first-principles calculation of the STM image of graphite. Results presented here are calculated with a W_{10}[111] cluster, because it is a most dull tip and is expected to be most stable. Figure 4.8 shows the W_{10}[111] cluster, the apex of which is aligned to [111] direction of the bulk crystal. The electronic structure of the tip is calculated by the DV-Xα method. Since discrete energy levels are obtained by a cluster calculation, the tunneling conductance obtained by differentiating the tunneling current shows a spiky spectrum. This singular structure of the tunneling conductance is unrealistic, because the apex of an actual tip is not an isolated cluster but attaches to the bulk part of the tip. Interaction between the cluster and

the bulk part broadens the energy width of the cluster levels. This effect is included by replacing the δ function in the tip Green's function of eq. (2.14) with a Lorentzian function as

$$G_{j'q',jq}^{\mathrm{T}}(E) = \sum_{\nu} a_{j'q'}^{\nu*} a_{jq}^{\nu} \frac{\Delta_{\nu}^2/\pi}{(E-E_{\nu})^2 + \Delta_{\nu}^2}. \qquad (4.8)$$

This replacement is convenient for calculating the tunneling conductance, because an analytical expression for the tunneling conductance is obtained by the replacement. The tunneling conductance can be calculated without a numerical differentiation of the tunneling current with respect to the bias voltage. The broadening width Δ_{ν} can be determined by the Green's function methods[128,129]. In the present calculation, Δ_{ν} is not calculated but assumed as a constant parameter for simplicity.

The calculated conductance images of graphite surface are shown in Fig. 4.9. The surface bias voltage is (a) 0.0, (b) −0.6, and (c) 0.6 eV. The energy width of the tip levels is assumed as 1.0 eV for (a) and 0.1 eV for (b), (c).

Figure 4.9(a) shows the triangular lattice similar to the LDOS image. When the energy width of the tip is large, the calculated STM images are normal one. This is because main component of the tip orbitals contributing to the tunneling conductance is the $d_{3z^2-r^2}$ type orbital of the apex atom. This orbital is axially symmetric around the axis normal to the surface. The calculated STM images are not changed by tilting the tip when the energy width Δ is large.

When the Δ is as small as the energy spacing of the cluster levels, anomalous images are obtained as shown in Figs. 4.9(b) and (c). In calculating these images, the three-fold-symmetry axis of the tip is not directed normal to the surface, but is slightly tilted by 7.5°. The stripe pattern is obtained in Fig. 4.9(b). The image in Fig. 4.9(c) is anomalous in a point that the minimum positions of the conductance are located not at the hollow site but at the atom site.

These images are similar to those obtained in the previous calculations using the H_2 molecule, but the origins of the anomalous images are different. In the previous calculations, the anomalous images were obtained by the
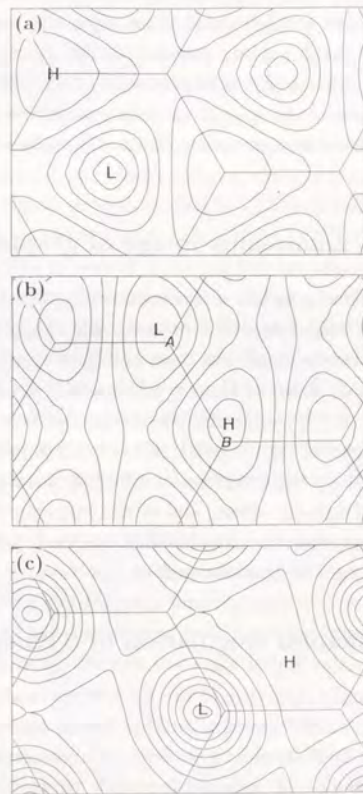
Figure 4.9: Calculated conductance images of graphite surface. The surface bias is taken as (a) 0.0, (b) −0.6, and (c) 0.6 eV. The energy width Δ of the tip levels is taken as 1.0 eV for (a) and 0.1 eV for (b),(c).

interference effect of the two atomic orbitals of the tip. This is a kind of the multiple-tip effect. In the present calculation, the anomalous images are obtained even with a single apex atom when the wavefunction of the tip contributing to the tunneling current has no $d_{3z^2-r^2}$ type component at the apex atom. This is not a multiple-tip effect. The latter origin of the anomalous images is the special electronic structure of the apex atom rather than the geometrical structure of the tip. Therefore, it is not the multiple-tip effect.

4.5 Origin of anomalous image of graphite

The STM image of the graphite surface has been calculated by Isshiki *et al.*[71] using various cluster models for the tip other than the $W_{10}[111]$ cluster, where the anomalous image has been obtained even with a large value for Δ, when the apex atom of the tip is removed and several atoms are active in tunneling. By investigating correlation between the STM images and the wavefunctions of tip in detail, it has been found that the anomalous image is caused by the interference effect of the wavefunctions. The mechanism is a multiple-tip effect, and is the same as the case of the H_2 tip. This is the most realistic and plausible mechanism for explaining the anomalous STM images of graphite surface.

4.6 First-principles calculation of STS spectrum

The microscopic atomic structure of the tip influences also on STS spectra of graphite surface. The extension of the Tersoff and Hamann's theory assuming a constant DOS for the tip leads to a simple result that a spectrum of the surface LDOS can be obtained from I-V characteristics in the STS as shown in eq. (2.6). However, the assumption of the constant DOS for the tip is rather simple, because most current flows through a few atoms of the tip apex. The electronic structure of the tip apex would be considerably different from that in a bulk metal. For example, if only one narrow level of the tip carries the tunneling current, the conductance spectrum is no longer proportional to the surface LDOS. In this case, the current spectrum itself is proportional to the surface LDOS. Actually, some phenomena have been observed where the non-constant behavior of the tip DOS is essentially important. The most evident example is the observation of a negative differential conductance (NDR) in the STS of $Si(111)\sqrt{3} \times \sqrt{3}$-B surface[75, 76] as shown in next chapter.

The STS spectra of graphite surface also depend on the atomic structure of the tip. Figure 4.10 shows conductance spectra of graphite surface calculated with various cluster models for the tip. The conductance is normalized by I/V. The model clusters used for the tip are (a) $W_{10}[111]$, (b) $W_{14}[110]$, and (c) $Pt_{10}[111]$. The figures of these clusters are shown in the right hand side of the corresponding spectrum. The tip-sample distance and the energy width Δ of the tip are taken as 2.6 Å and 1.0 eV, respectively. An experimental spectrum by Mizutani *et al.*[130] is also shown in the figures. From these figures, correlation of the spectrum and the apex profile of the tip is clear. For a dull tip such as the $W_{10}[111]$ cluster, difference between the STS spectra over the α and the β site of graphite surface is small. The sharper the apex profile of the tip, the larger the site difference of the STS spectra.

For a comparison, spectra calculated with an assumption that the tunneling conductance is proportional to the surface LDOS are shown in Fig. 4.11. This spectra can be regarded as a limiting case of the sharpest tip apex. It should be noted that, in contrast with the raw values of the tunneling conductance, the normalized one takes the larger value at the α site than at the β site.

In actual experiments, the apex of a sharp tip may be unstable, and atoms may be dissociated from the apex. Figure 4.12 shows STS spectra calculated with a $W_{13}[110]$ cluster model for the tip which is obtained by removing the apex atom of the $W_{14}[110]$ cluster. The tip-surface distance is taken as (a) 2.6 Å and (b) 5.3 Å. As seen in Fig. 4.12(a), for the tip without the apex atom, the normalized conductance at the β site is larger than that at the α site, which is different from the spectra obtained by the tip with the apex atom shown in Fig. 4.10. This is because when the tip-sample
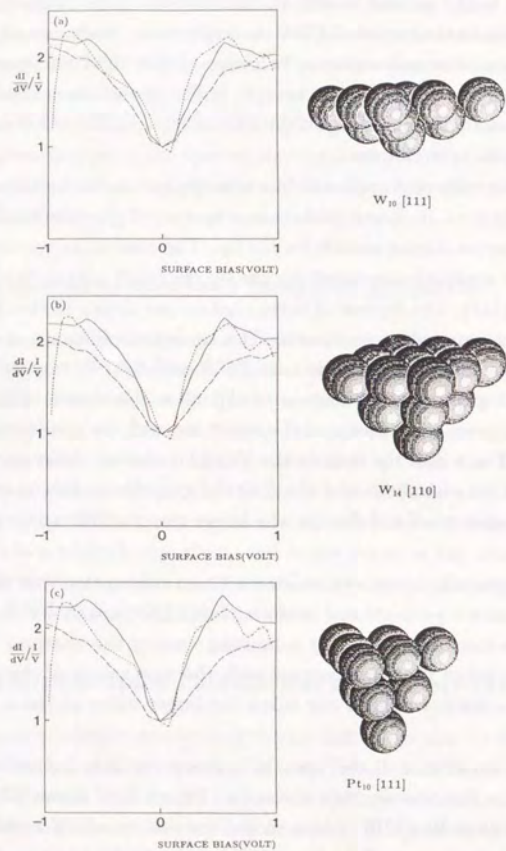
Figure 4.10: Normalized conductance spectra of graphite. Models for the tip are (a) $W_{10}[111]$, (b) $W_{14}[110]$, and (c) $Pt_{10}[111]$ cluster. The tip clusters are situated 2.6 Å above the α (solid lines) and the β (broken lines) site of graphite, respectively. The energy width Δ for the tip levels is infinitely large. An experimental spectrum by Mizutani *et al.*[130] is shown in each figure by a dotted line.
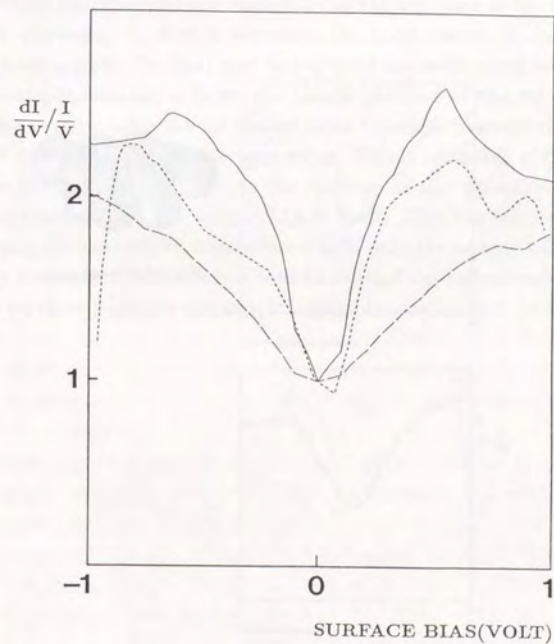
Figure 4.11: Normalized conductance spectra of graphite calculated with an assumption that the conductance is proportional to the LDOS of the surface.

(a)

$\frac{dI}{dV} / \frac{I}{V}$

2

1

−1   0   1

SURFACE BIAS(VOLT)

$W_{13}[110]$:Without Apex

(b)

$\frac{dI}{dV} / \frac{I}{V}$

2

1

−1   0   1

SURFACE BIAS(VOLT)
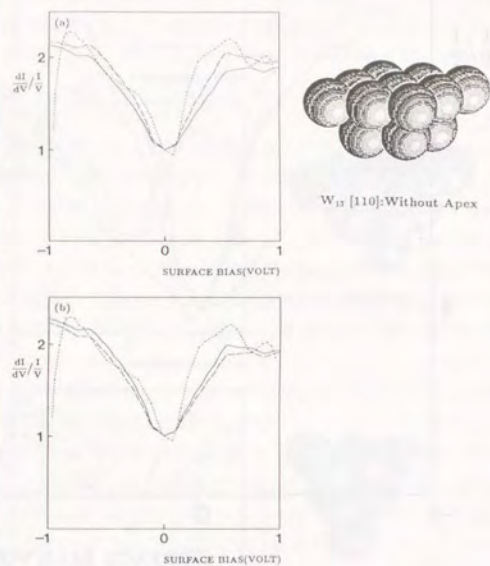
Figure 4.12: Normalized conductance spectra of graphite calculated with a $W_{13}[110]$ cluster. The tip-surface distances is (a) 2.6 Å and (b) 5.3 Å.

distance is short, more than one atoms of the tip are active in tunneling.

This multiple-tip effect is reduced as the tip-sample distance increases. The site dependence of the normalized conductance shown in Fig. 4.12(b) is the same as those in Fig. 4.10. This is because the number of the tip atoms which contribute to the tunneling current increases as the tip-sample distance increases. In such a situation, the grain nature of the atoms is smeared out, and the tip apex may be regarded as a continuous body. When the tip-sample distance is large, the lateral position of the tip where the tunneling current takes the maximum value coincides between the cases of tip with and without the single apex atom. This interchange of the spectra between the α and the β site as the increase of the tip-sample distance is not originated from the sample LDOS itself. This has been verified by calculating the normalized conductance with only the sample LDOS at 5.3 Å above the surface, where it has been found that dependence of the LDOS spectra on the tip-sample distance is negligibly small.

Chapter 5

STS of Si(111)$\sqrt{3} \times \sqrt{3}$-B/defect surface

5.1 Introduction

Recently, negative differential resistance (NDR) has been observed in the STS of Si(111)$\sqrt{3} \times \sqrt{3}$-B surface[75,76]. This phenomenon cannot be explained by the simple theory by Tersoff and Hamann. STS spectra of this surface have been calculated by the first-principles calculation taking a realistic tip-sample system into account[72,73]. In this chapter, calculated results are presented.

Si(111)$\sqrt{3} \times \sqrt{3}$-B surface itself has attracted much attention because of its unique structure. Most of column III elements such as Al, Ga, and In chemisorb on a 3-fold hollow site (B-T_4 site) of Si(111) surface. These surfaces are stabilized by eliminating the dangling bonds of the Si surface. For only B atom, however, the mechanism of stabilization is different from one stated above. Theoretical total-energy calculations[131]-[133] as well as experimental results[131]-[135] indicate that the B atom occupies a five-fold coordinated site on second atomic layer (B-S_5 site). Figure 5.1 shows the atomic and band structure of this surface calculated by the first-principles total-energy calculation[131]-[133]. A charge transfer from the top Si atom to the B atom is the mechanism of the stabilization. The uniqueness of the B atom results from the small covalent atomic radius comparing with the other column III elements.

The NDR has been observed in the STS spectra of this surface. Figure 5.2
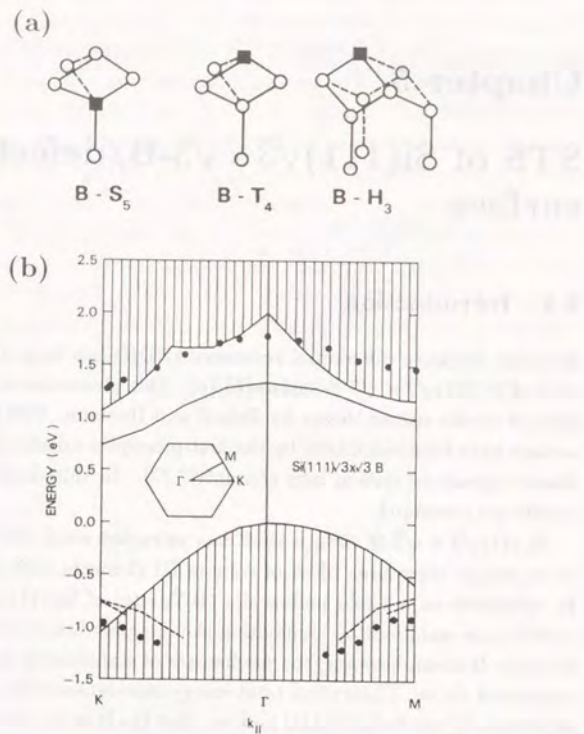
Figure 5.1: (a) The three possible positions of the B atom (square): B-S_5 is the substitutional position with a Si adatom directly above; B-T_4 is the adatom position above a second-layer Si atom; B-H_3 is the adatom position above an open hexagon of Si atoms. (b) Energy band for B-S_5 configuration of the Si(111)$\sqrt{3} \times \sqrt{3}$-B surface. Calculated surface states (full lines) and resonances (dashed lines) are compared to the results from photoemission and inverse photoemission experiments (dots). Projected bulk states are shaded. The surface Brillouin zone is shown as inset[133].
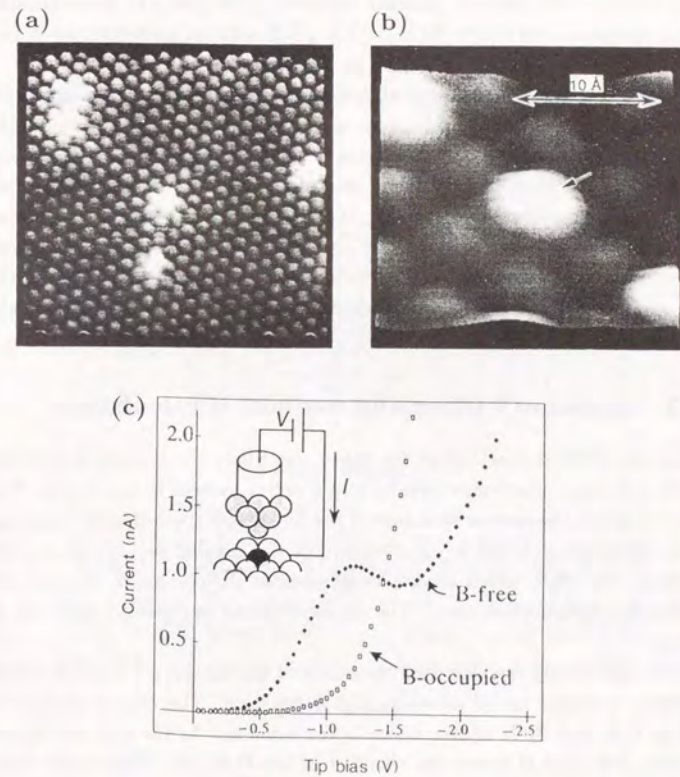
Figure 5.2: (a) Experimental STM image of Si(111)$\sqrt{3} \times \sqrt{3}$-B surface. Sample bias = 2 V. NDR is observed at the irregular white spots. (b) Localized defect site exhibiting NDR[75]. (c) Experimental STS spectra of Si(111)$\sqrt{3} \times \sqrt{3}$-B surface[76]. The B-free and B-occupied sites mean the defect and regular sites, respectively.

shows STM images and STS spectra on the Si(111)$\sqrt{3} \times \sqrt{3}$-B surface. The experimental observations indicate that the NDR seems to be associated with irregular sites of the Si(111)$\sqrt{3} \times \sqrt{3}$-B surface, possibly over defect sites where the B atom is replaced by a Si atom[75,76].

The appearance of the NDR should depend crucially on the microscopic electronic states of the tip, because a constant DOS of the tip inevitably leads to a positive differential resistance as shown in eq. (2.6). Therefore, theoretical calculations taking the electronic structure of the tip into account are necessary for discussing the NDR. In this chapter, calculated STM images and STS spectra of this surface are presented. They have been obtained by the first-principles electronic structure calculations of the tip-surface system. Based on the calculated results, a mechanism for the appearance of the NDR is discussed.

5.2 Model of surface and method of calculation

Since the NDR is observed at the defect site where the B atom is replaced with a Si atom, electronic structure of a defect system is calculated. Figure 5.3 shows the atomic structure of the Si(111)$\sqrt{3} \times \sqrt{3}$-B/defect system. The super cell is a $\sqrt{3} \times \sqrt{3}$ structure of the regular Si(111)$\sqrt{3} \times \sqrt{3}$-B surface. The B-S_5 site B atoms are situated at the corners of the unit cell indicated with dotted lines. The center B atom is replaced with the Si atom.

For calculating the electronic structure of the Si(111)$\sqrt{3} \times \sqrt{3}$-B/defect surface, a cluster model shown in Fig. 5.4 is used. The cluster consists of 78 Si, 6 B, and 51 H atoms, which is the same size as the unit cell shown in Fig. 5.3. The B atoms are situated in the B-S_5 site. The center B-S_5 site is occupied with a Si atom, which expresses a defect structure. The H atoms are used for eliminating the dangling bonds arising at boundary of the cluster. The position of these atoms is derived from the stable structures of this surface determined by the first-principles total-energy calculations[131]-[133]. The cluster models used for the tip are W$_{10}$[111], Pt$_{10}$[111], and W$_{14}$[110]. Electronic structure of the surface and tip clusters are calculated

Top View

Side View
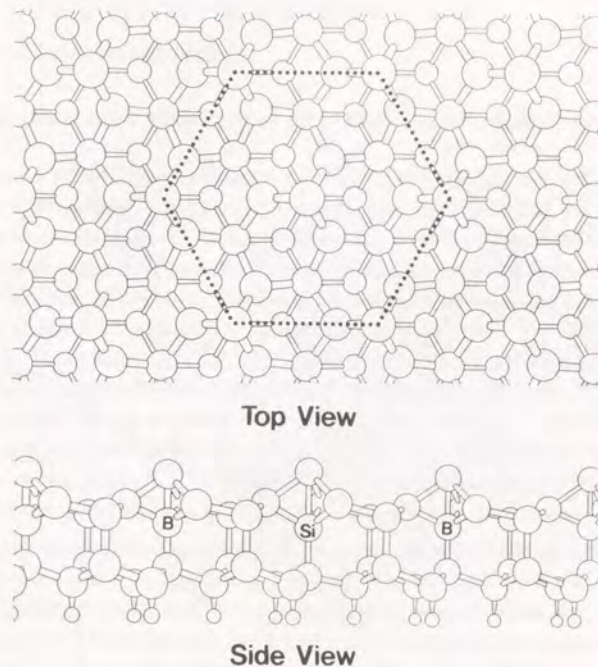
Figure 5.3: Structure model of Si(111)$\sqrt{3} \times \sqrt{3}$-B/defect surface. Unit cell is shown by the dotted lines.
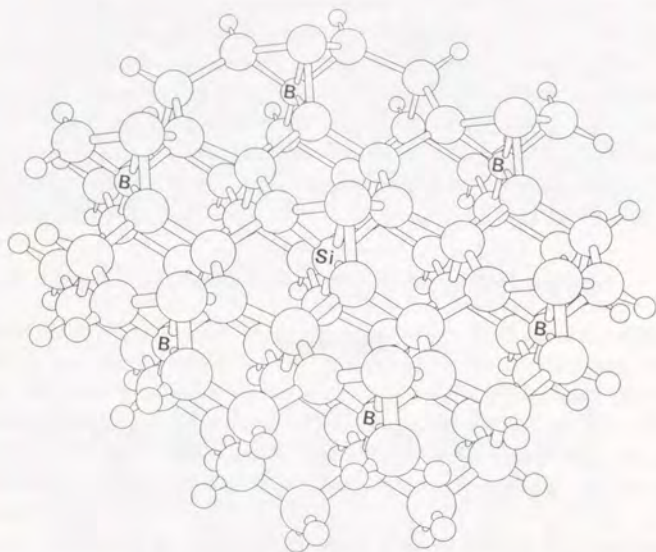
Figure 5.4: Cluster model $Si_{78}B_6H_{51}$ for $Si(111)\sqrt{3} \times \sqrt{3}$-B/defect surface. The cluster consists of 78 Si atoms, 6 B atoms, and 51 H atoms. The atoms denoted by B and Si are the boron atom at the B-S_5 site and the silicon atom at the defect site. The hydrogen atoms are added to eliminate the dangling bonds of the peripheral atoms.

by the DV-Xα-LCAO method. The tunneling current and conductance in the STM and STS are calculated by eq. (2.12).

5.3 Calculated result

5.3.1 Electronic structure of $Si(111)\sqrt{3} \times \sqrt{3}$-B/defect surface

Figure 5.5 shows a partial density of states (PDOS) of the cluster $Si_{78}B_6H_{51}$ at the adatom sites. Solid and broken lines show the PDOS's at the adatom Si site above the defect Si atom and above the B atom, respectively. Energy levels of the cluster around the Fermi level E_F are shown below the abscissa with the same energy scale. The PDOS is obtained by summing Lorentzian functions with a width of 0.3 eV centered at each level. The levels with energies lower than -1.2 eV and higher than $+1.8$ eV correspond to the valence and the conduction band of the bulk surface, respectively. The band gap is estimated at about 3 eV which is much larger than that obtained from the band calculation for the $Si(111)\sqrt{3} \times \sqrt{3}$-B surface without the defect shown in Fig. 5.1(b)[133]. The discrepancy is ascribed to the use of the cluster model and the LCAO basis in the present calculation.

In the gap region, dangling-bond states of the adatom Si appear. The four levels in the energy region between $+0.4$ eV and $+0.8$ eV are the dangling-bond states over the regular B sites, two of which are doubly degenerate. These dangling-bond levels are empty, since electrons in the dangling bond are donated to the B atom underneath. These feature are in good correspondence with the results of the band calculation[133].

The dangling-bond state of the Si adatom above the defect Si site is remarkably lowered. This level is occupied with an electron and becomes the Fermi level of the system. The PDOS at the adatom site over the defect shows a narrow peak centered at E_F. It has been verified that the features obtained in the present cluster calculation hold in a band calculation of the $Si(111)\sqrt{3} \times \sqrt{3}$-B/defect surface.

**Partial Density of States**
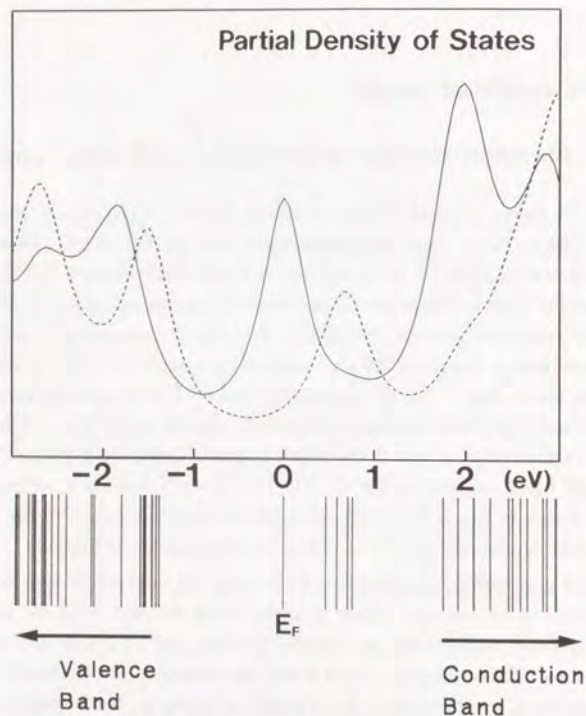
Figure 5.5: Level structure and partial density of states (PDOS) of the cluster $Si_{78}B_6H_{51}$. Solid and broken lines are the PDOS at the adatom sites above the defect Si atom and above the B atom, respectively. Energy levels of the cluster around the Fermi level E_F is shown below the abscissa with the same energy scale.

5.3.2 STM image and STS spectrum

Figure 5.6 shows calculated differential conductances dI/dV for the cluster model $Si_{78}B_6H_{51}$. The cluster model for the tip is $W_{10}[111]$. The conductance is calculated for the tip position at 2.6 Å directly above the adatoms (a) over the defect Si site and (b) over the regular B site. In the former case, the NDR appears around 2.2 V for the tip bias voltage, but does not appear in the latter case.

Figure 5.7 shows a contour map of the differential conductance fixing the tip bias at 2.2 V. The NDR appears only over a localized region around the defect site. Regions showing a strong tunneling conductance are located around the adatom sites over the regular B atoms. These features correspond well with the experimental images shown in Fig. 5.2[75,76]. However, it cannot be claimed here that the tip represented by the $W_{10}[111]$ model is a unique one reproducing the NDR feature. The experiments[75,76] show that the NDR is observed for a negative tip bias or even for both signs of the tip bias depending on the experimental condition. Such a variation of the experimental results indicates that the NDR can be induced by various types of tip states. The case presented here should be considered as a typical example.

5.3.3 Mechanism of NDR

Appearance of the NDR in the STS is closely related to the electronic structure of the tip as well as that of the sample surface. In the case of the $W_{10}[111]$ tip, it is found that more than half of the tunneling current flows through one level of the tip, which is located at an energy 1.5 eV above the E_F. This level has a dominant orbital character of $5d_{3z^2-r^2}$ of apex W atom. Hereafter, this level is labeled by L. A dominant contribution of this level to the tunneling conductance is clearly demonstrated in Fig. 5.6(a) which shows the calculated differential conductance assuming only the level L for the tip. Since, except for the half-occupied dangling-bond state, there is no level localized at the adatom over the defect B site in the energy gap of the $Si(111)\sqrt{3} \times \sqrt{3}$-B/defect surface, the qualitative structure of the tunneling
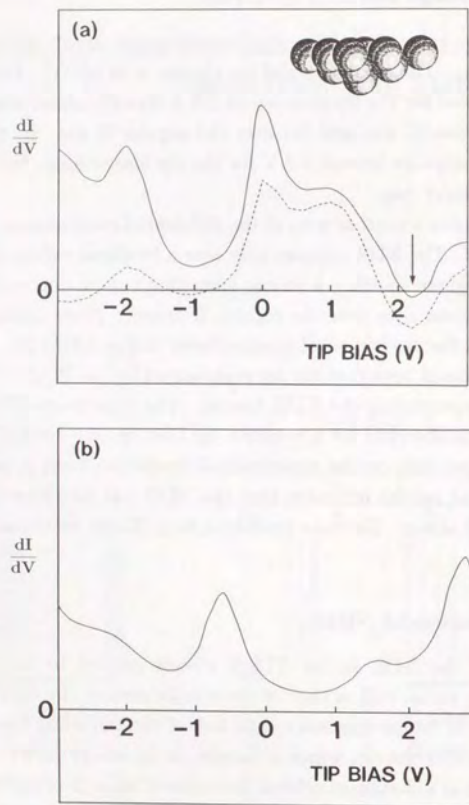
Figure 5.6: Calculated tunneling conductance of $Si(111)\sqrt{3} \times \sqrt{3}$-B/defect surface using the $Si_{78}B_6H_{51}$ and $W_{10}[111]$ cluster models for the surface and the tip, respectively. The tip is put above (a) the defect site and (b) the boron site. Broken line in the figure (a) shows the partial contribution of the tip level L.
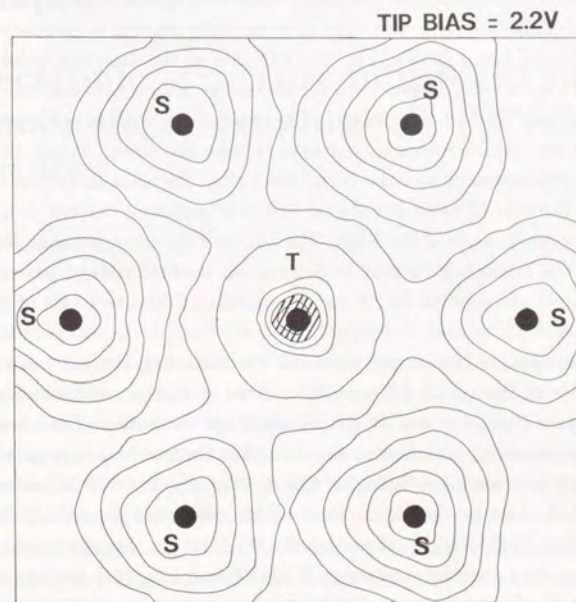
Figure 5.7: Contour map of the tunneling conductance when the tip bias voltage is 2.2 V. Closed circles show the positions of the adatoms. T and S denote the positions above the defect Si and the B atoms, respectively. Region of the NDR is shaded.

conductance is determined almost by the two levels, i.e., the dangling-bond state at the adatom over the defect site and the tunnel-active level L of the $W_{10}[111]$ tip.

In such a situation, the NDR is induced, because the tunneling current via these two levels takes the maximum value at a certain bias voltage. This is easily understood by a fact that the tunneling current is governed by a convolution of two LDOS's, i.e., the LDOS's of the dangling-bond state and of the tip level L integrated over an energy region between the Fermi energies of the tip and the surface. Therefore, in a small bias voltage, the tunneling current increases as the bias voltage increases. When the bias voltage much increases and the Fermi level offset becomes large, the convolution of the two LDOS's is reduced and the tunneling current decreases. This is the mechanism of the NDR. The bias voltage corresponding to maximum of the tunneling current is determined by four energy parameters, i.e., the positions relative to E_F and the widths of the two levels of the tip and surface.

Of course, there are contributions to the tunneling current from many other levels of the tip and the surface. Sum of such a residual tunneling current generally increases as the bias voltage increases. Therefore, the NDR is most easily observed in the case that the residual current is minimized. A favorable condition for this is that the two levels are narrow and located close to the Fermi level. This condition is satisfied for the $Si(111)\sqrt{3} \times \sqrt{3}$-B/defect surface and the $W_{10}[111]$ tip. Similar calculations of the tunneling conductance using $W_{14}[110]$ and $Pt_{10}[111]$ clusters as the models of tip do not show the NDR even for the same surface model. The absence of the NDR for these tip models is explained by an appearance of several tunnel-active orbitals in these tip states; an NDR by any one of the tunnel-active orbitals is overwhelmed by a positive contribution from the remaining tunnel-active orbitals. These results indicate importance of the electronic states of the tip for the appearance of NDR.

Chapter 6

Electronic structure and STM image of monolayer graphite on TiC(111) surface

6.1 Introduction

As shown in chapter 4, the STM image of graphite surface shows a triangular-lattice pattern which is different from one expected from the honeycomb-atomic structure of graphite lattice. This fact has been explained by the site difference of amplitude of the wavefunction near the Fermi level due to the interlayer interaction of graphite. The observation of the triangular-lattice image in the STM of graphite surface is a clear evidence for the fact that the STM observes the electronic structure of surfaces

Above discussion suggests that if surface of a single-layer graphite were observed by the STM, a honeycomb lattice image would be obtained. With such an expectation, STM image of monolayer graphite grown on TiC(111) surface has been taken. The obtained image showed, against the expectation, a triangular-lattice pattern similar to that of a bulk graphite surface[84]. Figure 6.1 shows experimental STM images of the monolayer graphite on TiC(111) surface. Period of the triangular pattern, however, is as long as 5 Å which is about twice of the lattice constant of bulk graphite. Furthermore, at a certain bias voltage, a moiré pattern has been observed, where amplitude of the triangular pattern is modulated with a longer period of about 21 A. Low-energy electron diffraction (LEED) study has shown that the

occupied state   10Å   unoccupied state
Sample Bias −700mV   Sample Bias +730mV
Graphite on TiC(111)
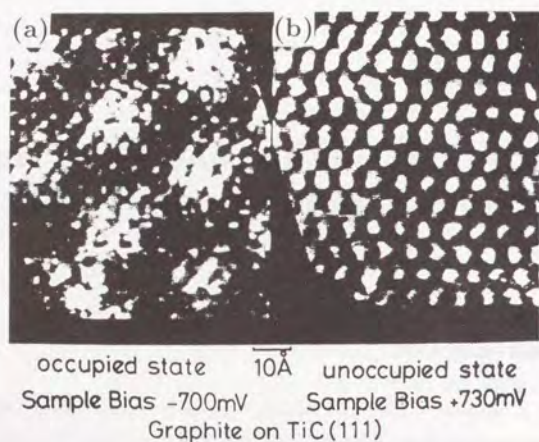
Figure 6.1: Experimental STM images of monolayer graphite on TiC(111) surface by Itoh *et al.*[84]. Sample bias voltage is (a) −700 mV and (b) 730 mV.

graphite layer is incommensurate with the substrate and that the periods of the superstructures observed in the STM image correspond to multiple-scattering diffraction spots[84]. The moiré pattern has been observed in the STM images of the monolayer graphite on other substrates such as Pt(111) surface[136]. The observation of the superstructure in the STM suggests that the electronic structure of the monolayer graphite is locally modulated by perturbation of the substrate.

The monolayer graphite is grown on various metal substrates by disso-ciation of hydrocarbons[137]. The substrate metals may be pure transition metals such as Ni and Pt, and transition-metal carbides such as TiC, TaC, and HfC. Except for Ni(111) surface, the monolayer graphite is incommen-surate with the substrate. In-plain lattice of the monolayer graphite on metal substrates is expanded than that of the bulk graphite. Depending

on kind of the substrate, C-C bond length of the monolayer graphite varies from 1.42 Å up to 1.46 Å, which is larger at maximum by 3 % than that of the bulk graphite. Degree of the expansion is fairly large comparing with that in graphite intercalation compounds (GIC's) where the lattice expansion of the graphite layer is less than 1 %[138].

The distance between the monolayer graphite and substrates has been de-termined experimentally by extended-energy-loss fine-structure spectroscopy [139] or dynamical-LEED analysis[140] only for Ni(111) and Pt(111) sub-strates. In the case of the Ni(111) substrate, the distance is 2.8 Å which is much smaller than the interlayer distance of 3.35 Å in the bulk graphite[139]. This suggests that the binding between the monolayer graphite and the Ni(111) surface may be qualitatively different from the weak van der Waals binding of bulk graphite layers[141]-[144].

In contrast with the Ni(111) case, the distance between the monolayer graphite and the Pt(111) surface is 3.7 Å which is fairly longer than the bulk value[140]. Since it is hard to suppose that the graphite layer is supported above the substrate at a height much larger than the interlayer distance of bulk graphite, the anomalous large distance is explained by introducing an additional adsorbate-like carbon layer between the graphite layer and the Pt(111) surface. For other substrates than Ni(111) and Pt(111), the dis-tance between the graphite layer and the substrate has not been determined experimentally at present.

Recently, phonon structure of the monolayer graphite on metal sur-faces has been measured extensively, where interesting properties have been found[145]-[149]. Figure 6.2 shows experimental phonon structures of the monolayer graphite on TiC(111) surface and of bulk graphite. From an analysis of the phonon structures, it has been found that the C-C bond of the monolayer graphite is generally much weaker than that of the bulk graphite and that the binding of the monolayer graphite to the substrate is stronger than the interlayer binding of the bulk graphite. Degree of the deviation of the phonon bands from those of the bulk graphite depends on kind of the substrate material and the surface direction of the substrate. For example, phonon dispersion of the monolayer graphite on TaC(111)
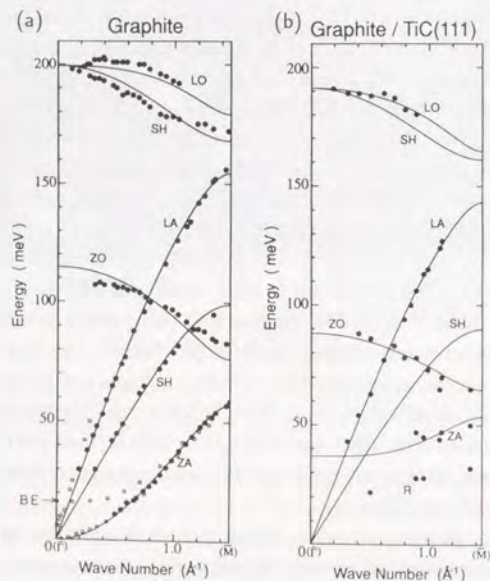
Figure 6.2: Experimental phonon structure of (a) bulk graphite and (b) monolayer graphite on TiC(111) surface by Aizawa *et al.*[145].

surface is fairly deformed, but that on TaC(100) surface is almost the same as the bulk graphite.

So far, the weakening of the C-C bond in the monolayer graphite has been explained in terms of a rigid band model with electronic charge transfer from the substrate to the graphite layer[145,150]. Unoccupied π^* band of graphite is partially filled with the transferred charge, which causes the weakening of the C-C bond.

Similar phenomena have been observed in graphite intercalation compounds (GIC's)[138]. The GIC's are made by intercalating a material into the interlayer gap of graphite. Electronic properties of the GIC's are explained by the rigid band model with charge transfer between the graphite layer and the intercalant. In a donor-type GIC, electrons in the intercalant transfer to the graphite. The C-C bond of the graphite layer is weakened, and the lattice constant expands. A first-principles electronic structure calculation shows a relation between the amount of the transferred charge and the expansion of the graphite lattice, which reproduces well experimental results[151]. For the monolayer graphite on TiC(111) surface, the charge transfer estimated from the lattice constant via the above relation is 0.4 electrons per C atom which is considerably larger than those of the GIC's. In other words, the lattice constant of the monolayer graphite on metal surfaces is anomalously expanded.

Since carbon is electro-negative species comparing to transition metals, charge transfer between carbon atoms and transition metals occurs in transition-metal carbides. The transition-metal carbides form a rock-salt structure like alkali halides as shown in Fig. 6.3. However, different from alkali halides, they are metals. Figure 6.4 shows the band structure of TiC crystal. The bands near the Fermi level consist of the hybridized Ti $3d$ and C $2p$ orbitals.

Because of the rock-salt structure, surface electronic structure of the transition-metal carbide is strongly dependent on a cut plane. The electronic structure of (100) surface is similar to that of the bulk, showing no remarkable feature. In contrast to the (100) surface, (111) surface shows distinctive features. The (111) surface is a polar surface consisting of either
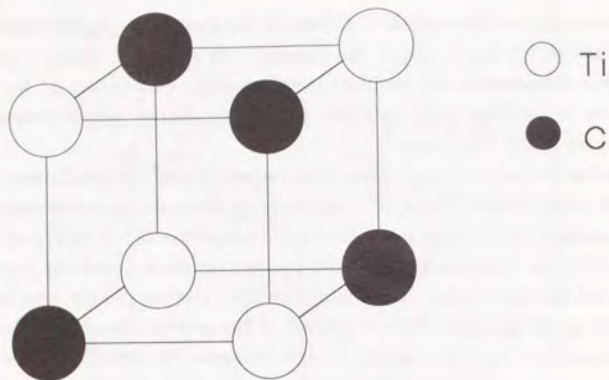
Figure 6.3: Atomic structure of TiC crystal.

a carbon layer or a transition-metal layer, and surface states localized in the outermost layer appear around the Fermi level. Figure 6.5 shows the band structures of the TiC (111) and (100) surface. The (111) surface shows surface bands localized in the outermost Ti layer around the Fermi level, but the (100) surface does not show in the same energy region.

One of features of the polar surface is that amount of the charge transfer in outer layers is much reduced comparing to that in inner layers. This has been explained by a depolarization effect which is a screening effect of surface electric field induced by the polar layers[152]-[154]. Since the outer layer of the (111) surface of the transition-metal carbides is usually the transition-metal layer, the charge transfer between the monolayer graphite and the substrate also has been expected.

Angle-resolved ultraviolet photoelectron spectroscopy (ARUPS) of the monolayer graphite on TiC(111) surface shows a distinct band dispersion which is similar to the occupied π band of the bulk graphite but shifts to a lower energy region by a few eV as shown in Fig. 6.6[155]. This suggests
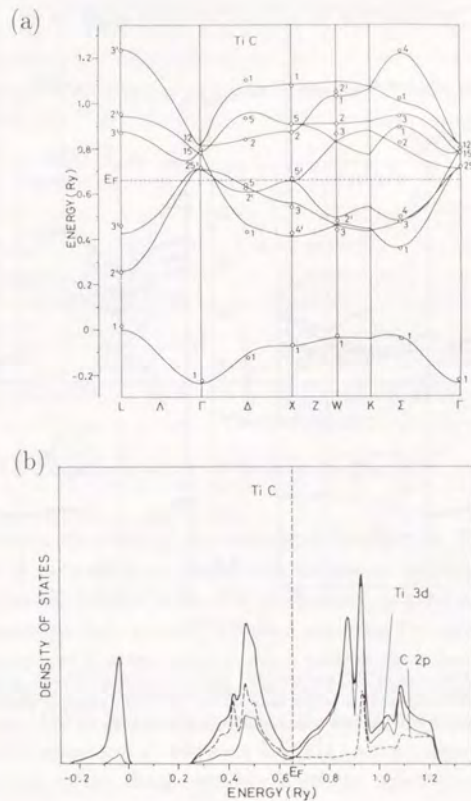
Figure 6.4: (a) Band structure and (b) density of states of TiC crystal[152].
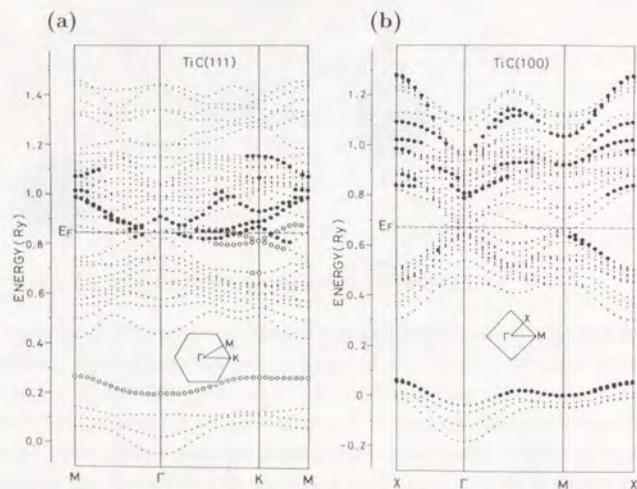
Figure 6.5: Band structures of TiC surface[152]. (a) (111) surface. Closed circles show the states whose surface component is larger than 50 %. (b) (100) surface. Open and closed circles show the states whose surface component is larger than 80 %.
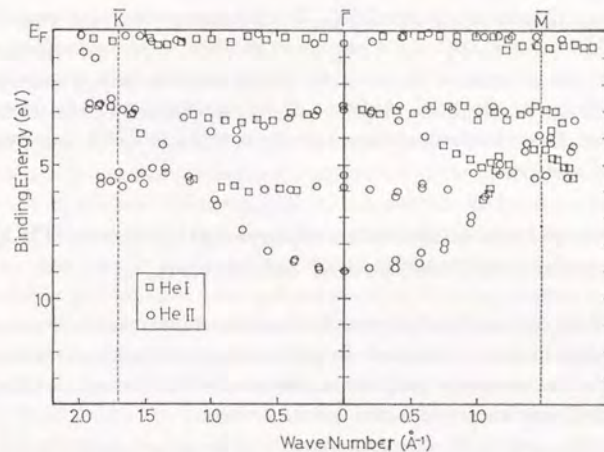
Figure 6.6: Experimental ARUPS of monolayer graphite on TiC(111) surface[155].

that electronic structure of the monolayer graphite on TiC(111) may be explained by the rigid band model with the charge transfer to the graphite layer in the same manner as the GIC's. However, amount of the transferred charge estimated from the ARUPS data assuming the rigid band model is 0.02 electrons per C atom which is much smaller than that estimated from the lattice constant expansion via the result of the first-principles calculation for the GIC's. Moreover, peaks of X-ray photoelectron spectroscopy (XPS) of the monolayer graphite on TiC(111) surface does not show a shift corresponding to the charge transfer from the substrate to the graphite layer[155].

Disagreement of the amounts of the charge transfer estimated from the several experiments shows that the electronic structure of the monolayer graphite on TiC(111) surface cannot be explained by the simple rigid band

model with the charge transfer. Small difference of work functions between the bulk graphite surface and the TiC(111) surface also does not support the charge transfer mechanism[155]. Recent experiments of plasmon[156] and STM images[84,136] of the monolayer graphite on metal surfaces suggest that the influence of the substrate on the graphite layer is important. For clarifying the electronic structure of the monolayer graphite on metal substrates, theoretical calculations have been performed[157] as presented in this chapter.

6.2 Structure model of monolayer graphite on TiC(111) surface and method of calculation

In this chapter, calculated electronic structure of the monolayer graphite on TiC(111) surface is presented. In performing an electronic structure calculation of the monolayer graphite on transition metal surfaces, a difficulty arises from their incommensurate atomic structure.

Electronic structures of incommensurate systems have been studied extensively. Using an one-dimensional tight-binding model with an external potential which has a period incommensurate to the lattice, Aubry and André studied wavefunctions of the system and showed that metal-insulator transition occurs when the strength of the external modulation potential coincides with transfer energy of the tight-binding model[158,159]. The localization problem in incommensurate systems was studied also with a Kronig-Penny model, and results similar to those by Aubry and André were obtained[160]. Beyond these model calculations, no method for calculating the electronic structure of realistic incommensurate systems has been established. At present, two approximate methods are practical for dealing with the realistic incommensurate system.

One is a cluster method, where an infinite incommensurate system is modeled by a finite size cluster. If we can use an extremely large cluster so that energy spacing of the cluster levels is negligibly small, this method is effective. In practice, the size of the cluster is limited by computational capacity. The recursion formula is useful for extracting bulk properties

from a calculation using a relatively small cluster[161,162]. However, the application of the recursion method is restricted to the tight-binding model. Therefore, the cluster method is not suitable for the purpose of the present calculation.

Another approach for obtaining an electronic structure of a realistic incommensurate system is to perform a band calculation by changing the lattice constant so that the system becomes commensurate. If the change of the lattice constant is small and the problem of the localization is not interested in, this rational approximation is a practical and useful method. A merit of this method is that band dispersions are obtained. By an analysis of the character of wavefunctions, the obtained dispersions can be projected into an extended zone and compared with an experimental one. In the present thesis, band calculations of the monolayer graphite on TiC(111) surface are performed by changing slightly the lattice constant of graphite so as to be commensurate with the substrate. This change influences quantitatively such values as a band width, but it has been verified by performing the band calculation for several lattice constants that the results do not change qualitatively. When an incommensurate substrate-overlayer system is rationally approximated by changing the lattice constant, lateral position of the overlayer relative to the substrate is not well-defined. In this thesis, the band calculation is performed for two cases of different lateral positions.

It has been known experimentally by an analysis of the LEED pattern[84] that the lattice constants of the TiC(111) surface and the monolayer graphite on TiC(111) surface are 3.06 Å and 2.50 Å, respectively, and the directions of the unit lattice vectors are rotated by 30° each other. When the lattice constant of graphite is expanded by about 6 %, the monolayer graphite becomes commensurate with the substrate. Figure 6.7 shows structure models of the monolayer graphite on TiC(111) surface. The unit cell of the present models corresponds to that of a $\sqrt{3} \times \sqrt{3}$ structure for TiC(111) surface and of a 2×2 structure for the graphite layer. The lattice constant of the unit cell is chosen as 5.30 Å. First Brillouin zone corresponding to the unit cell is shown in Fig. 6.8.

The present unit cell is too small to discuss the moiré pattern observed

(a)

Graphite
Ti
C
Ti
C

Side View

(b)
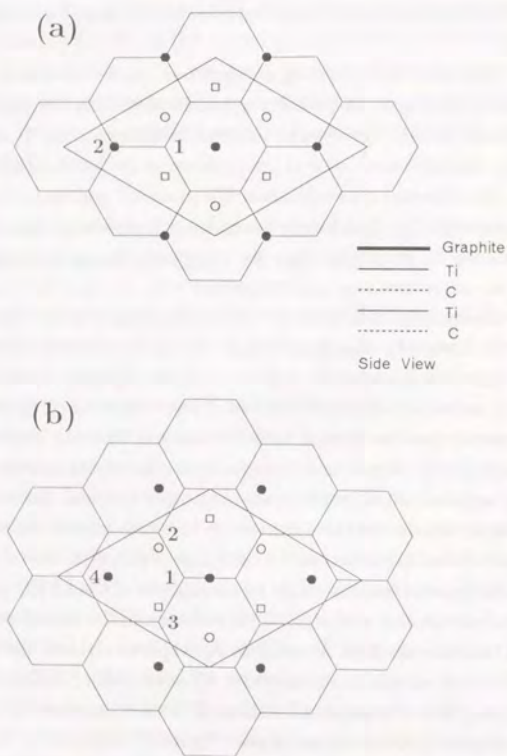
Figure 6.7: Structure models for the monolayer graphite on TiC(111) surface: (a) model A and (b) model B. Graphite lattice is expressed by the honeycomb structure. Closed circles indicate first layer Ti atoms and fourth layer C atoms of the TiC(111) surface. Open circles and open squares indicate second layer C atoms and third layer Ti atoms, respectively. Rhombus shows the unit cell. Numbers in the figure distinguish the inequivalent C atoms in the graphite layer.
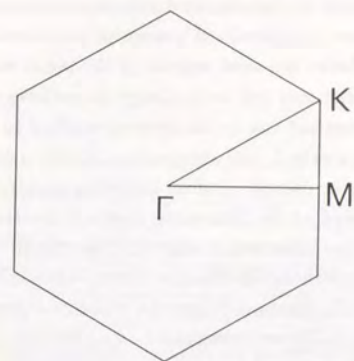
Figure 6.8: Brillouin zone for the unit cell of the structure models for the monolayer graphite on TiC(111) surface shown in Fig. 6.7.

in the STM image, the period of which is as long as 21 Å. It is difficult to perform a first-principles band calculation of a system with such a large unit cell. Therefore, in this thesis, two steps are taken to approach to discussion of the moiré pattern.

First, electronic structure of the small unit cell shown in Fig. 6.7 is solved by the first-principles band calculation, where amount of the charge transfer is determined self-consistently. In the second step, electronic structure of the system with a large unit cell and STM image are calculated with a tight-binding model. Parameters of the tight-binding model are determined to reproduce the band structure obtained by the first-principles calculation with the small unit cell.

In the band calculation, a slab model is used. The slab is consisting of one graphite layer and four TiC(111) layers. The unit cell contains 14 carbon atoms and 6 Ti atoms. The height of the graphite layer measured from the top layer of the TiC(111) surface has not been determined exper-

imentally. It would be desirable to determine the height theoretically by a first-principles total energy calculation. However, it is difficult to deal with both C and Ti atoms by the standard pseudo-potential method with plane wave bases, because of a localized nature of the atomic orbitals[163,164]. Even if Gaussian bases are used instead of the plane waves, number of the atoms in the present unit cell is too large to perform a band calculation. Only the DV-Xα method can be moderately applied to the present system.

In the DV-Xα method, the integration of the matrix elements is replaced by a sum over pseudo-random sampling points. Numerical error of the method is typically 1 %. This error does not matter in discussing band structures, but is too large to calculate a total energy of the system where higher precision is demanded. In this thesis, the band calculation is performed by the DV-Xα method, where the graphite-substrate distance is not determined theoretically but is regarded as a parameter. Plausible value of the parameter is determined by comparing the calculated results with the experiments.

The band calculation is performed for three different heights. One is 2.16 Å which is the same as the C-Ti bond length in a bulk TiC. Second one is 3.42 Å which is determined from the experimental value for the monolayer graphite on Ni(111) surface with consideration of the difference of atomic radius between Ti and Ni. This is almost the same value as the interlayer distance in the bulk graphite. Finally, 2.8 Å is selected which is the mean value of 2.16 Å and 3.42 Å. The band calculation is performed with all electrons. Basis atomic orbitals from $1s$ up to $2s$, $2p$ for C and up to $3d$, $4s$, $4p$ for Ti are used. Self-consistency is checked by the Mulliken population analysis[165]. Criterion of the self-consistency is that inconsistency of each atomic orbital charge between iterations is less than 0.01 electrons.

6.3 Calculated band structure and electronic charge

Figure 6.9 shows a calculated band structure of the monolayer graphite on TiC(111) surface. The band calculation is performed for the model A in Fig. 6.7. The graphite-substrate distance is 2.16 Å. In this figure, two
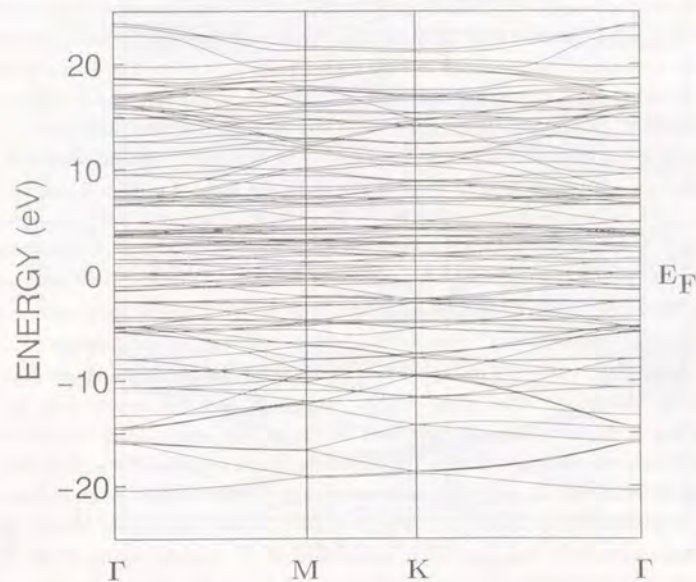
Figure 6.9: Calculated band structure of the monolayer graphite on TiC(111) surface for the model A, when the graphite-substrate distance is 2.16 Å. Origin of the energy is chosen as the Fermi energy.

types of bands are seen. Many bands are concentrated near the Fermi level without significant dispersions, which are mainly the $3d$ bands of Ti. Bellow these bands, several bands are seen with relatively large dispersions, which are the σ bands of the graphite. The π bands of the graphite are mixed with the bands of the substrate, and it is difficult to distinguish them.

To make clear the π band structure of graphite, bands with comparatively large π orbital component of graphite are picked out. The bands, whose graphite $2p_z$ component is larger than 25 %, are represented by open circles in Fig. 6.10. From the figure, distinct band dispersions are grasped. The occupied π bands in an energy region from -10 eV to the Fermi level correspond well to those of the bulk graphite projected into the 2×2 unit cell. It is known that the Fermi level of the bulk graphite is located at a K point in the unfolded Brillouin zone[107]. The K point in the unfolded Brillouin zone is folded to a K point in the Brillouin zone of the 2×2 unit cell as indicated by an arrow in Fig. 6.10. The energy at about 2.5 eV below the Fermi level corresponds to the Fermi level of the bulk graphite. Namely, the original Fermi level of the bulk graphite is lowered by about 2.5 eV relative to the Fermi level of the monolayer graphite on TiC(111) surface, and the originally unoccupied π^* band of the bulk graphite is partially occupied.

In contrast with the occupied bands, the unoccupied π^* bands are drastically deformed. The most striking feature is that the bands with the strong π character are scarcely seen in the energy region from 0 to 5 eV above the Fermi level. In this region, the π bands are strongly mixed with the $3d$ bands of Ti and distribute over many bands. This is evident from Figs. 6.10(b), 6.11, and 6.12. Figure 6.10(b) shows the bands, whose $3d$ component of the top layer Ti is larger than 25 %. The $3d$ bands of the Ti layer are concentrated in the region from -1 to $+5$ eV. Figure 6.11 shows the $2p_z$ components of the graphite and the $3d$ component of the top layer Ti in the total density of states. The occupied region of the partial density of states (PDOS) of the graphite shows the π band structure similar to that of the bulk graphite. However, the unoccupied region is deformed by the mixing with the $3d$ bands of the Ti. The feature of the energy dependent mixing is also evident in Fig. 6.12, which shows LDOS on a plane containing

(a)

(b)
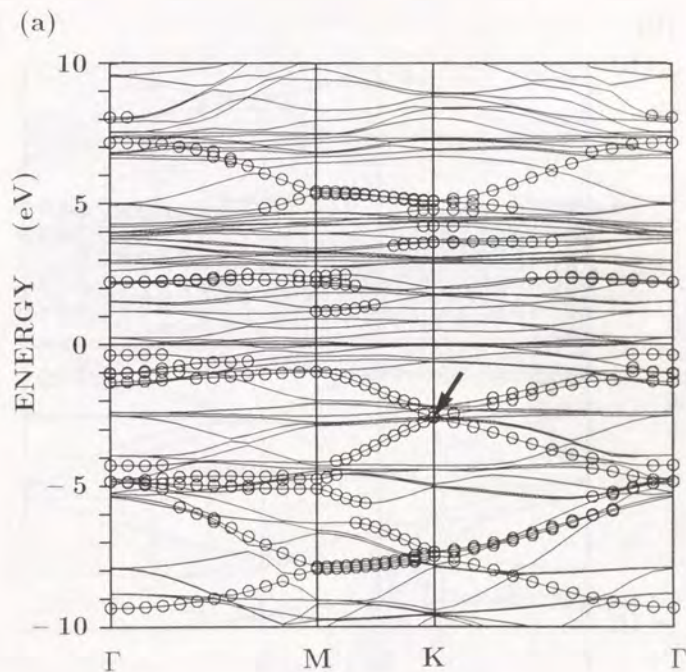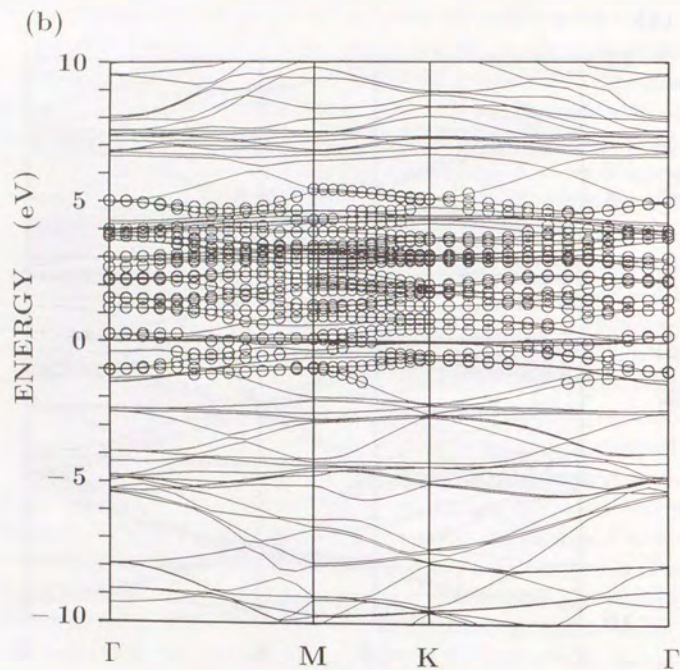
Figure 6.10: Calculated (a) π band and (b) $3d$ band structure of the monolayer graphite on TiC(111) surface for the model A, when the graphite-substrate distance is 2.16 Å. Open circles indicate the bands, whose (a) $2p_z$ component of the graphite layer and (b) $3d$ component of the first layer Ti are larger than 25 %. The arrow indicates the point corresponding to the Fermi level of an isolated monolayer graphite.

72
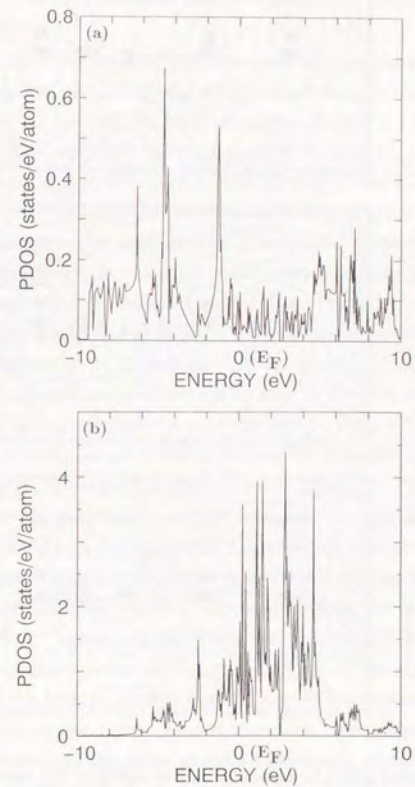
Figure 6.11: Calculated PDOS of the monolayer graphite on TiC(111) surface for the model A, when the graphite-substrate distance is 2.16 Å: (a) π component of the graphite layer and (b) $3d$ component of the top layer Ti of TiC(111) surface. Origin of the energy is chosen as the Fermi level.

73
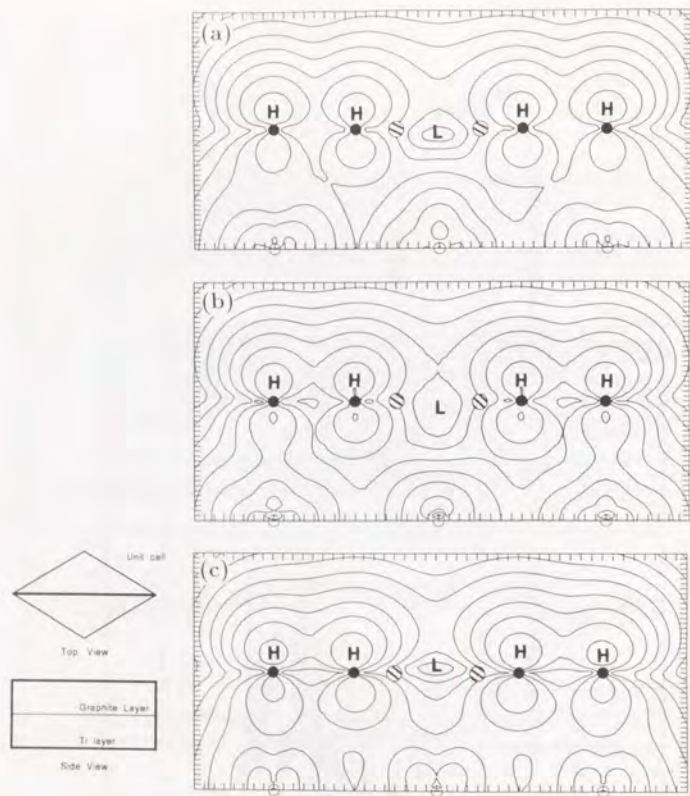
Figure 6.12: Calculated LDOS in a plane normal to surface of the monolayer graphite on TiC(111) for the model A. The graphite-substrate distance is 2.16 Å. The energy of LDOS is selected for (a) 1.0 eV, (b) 0.0 eV, and (c) −3.0 eV. H and L denote maximum and minimum positions of the LDOS. Closed and open circles indicate position of the C atoms of the graphite layer and the top layer Ti atoms of the TiC(111) surface, respectively. These are situated on the cut plane. Hatched circles indicate the position of the C atoms of the graphite layer which are situated out of the cut plane. The cut plane is illustrated by heavy lines at the bottom of the left-hand side.

the C atoms of graphite and the Ti atoms perpendicular to the surface. The mixing of the wavefunctions between the graphite layer and the substrate is weaker for the occupied states and is stronger for the unoccupied states near the Fermi level.

When the graphite-substrate distance is as long as the interlayer spacing of the bulk graphite, the electronic structure of the graphite layer becomes almost the same as that of the bulk graphite. Figure 6.13 shows the band structures for cases with the distance (a) 2.8 Å and (b) 3.42 Å. When the graphite-substrate distance is 3.42 Å, the mixing of the π bands and the $3d$ bands is much reduced, and the unoccupied π bands are well distinguished. As the distance increases, the original Fermi level of the bulk graphite is lifted toward the Fermi level of the monolayer graphite on the substrate. The distance dependence of the energy shift of the π bands relative to the Ti d bands suggests that the orbital hybridization between the graphite layer and the substrate is important in this system. In contrast to the π band structure, the $3d$ band structure of the Ti layer is not so changed as the increase of the graphite-substrate distance. Figure 6.13(c) shows the bands, whose $3d$ component of the top layer Ti is larger than 25 % for the case that the graphite-substrate distance is 3.42 Å.

To determine the graphite-substrate distance, the calculated band structure is compared with an experimental dispersion obtained from ARUPS[155]. Figure 6.14 shows the band structure projected from the 2×2 to the 1×1 Brillouin zone of the bulk graphite for the case that the graphite-substrate distance is 2.16 Å. Agreement between the theory and the experiment is fairly good. Important point is that the K point of the experiment, which corresponds to the original Fermi level of the bulk graphite, is also located at about 3 eV below the Fermi level of the monolayer graphite on TiC(111) surface. In the case of the large graphite-substrate distance, the lowering of the K point is about 1 eV as shown in Fig. 6.13(b). This result shows that the graphite-substrate distance is not so large as 3.42 Å, but is fairly small as 2.16 Å.

The fact that the original Fermi level of the bulk graphite is lowered below the Fermi level in the monolayer graphite on the substrate seems to

(a)

(b)

(c)
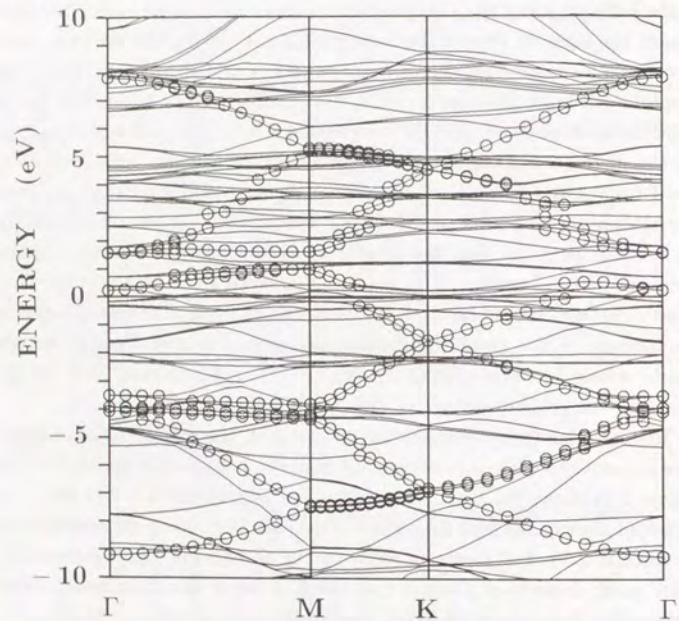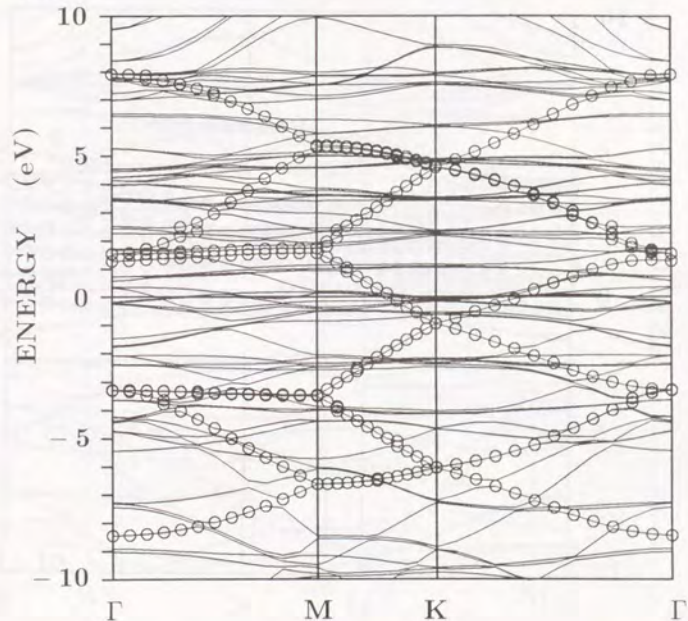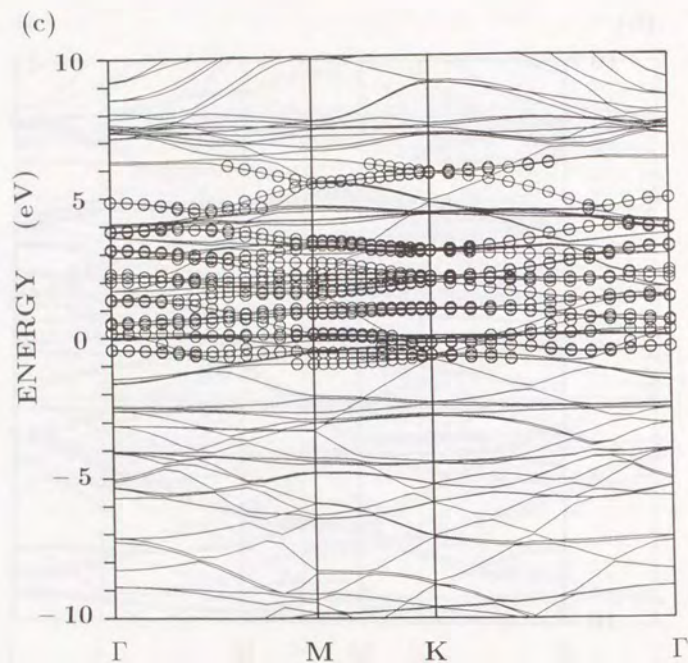
Figure 6.13: Calculated (a), (b) π band and (c) $3d$ band structure of the monolayer graphite on TiC(111) surface for the model A, when the graphite-substrate distance is (a) 2.8 Å and (b), (c) 3.42 Å. Open circles indicate the bands, whose (a), (b) $2p_z$ component of the graphite layer and (c) $3d$ component of the first layer Ti are larger than 25 %.
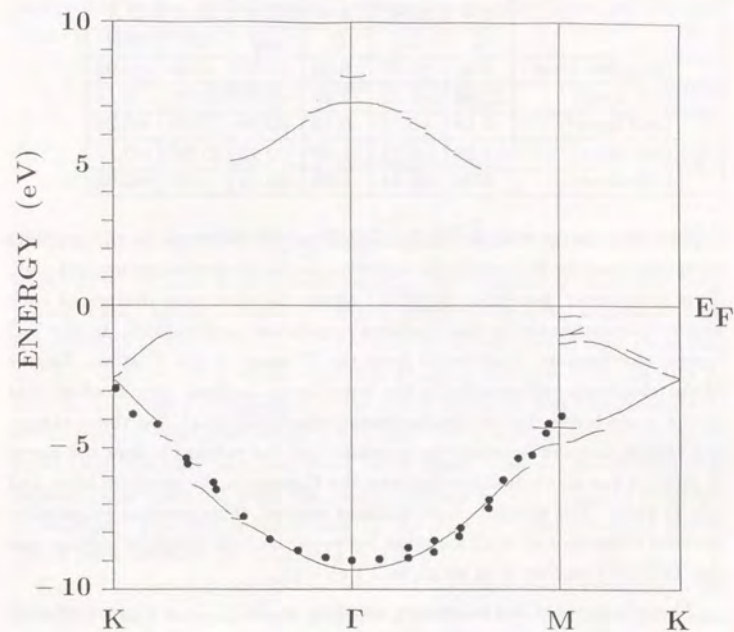

Figure 6.14: Comparison of calculated π band structure of the monolayer graphite on TiC(111) surface with experimental data. Solid lines indicate the calculated band which are obtained from the data shown in Fig. 6.3(a) projected into 1×1 Brillouin zone of the bulk graphite. Closed circles show the experimental dispersions obtained from ARUPS data by Nagashima et al.[155].

Table 6.1: Electron numbers of atoms in each layer for the model A and B estimated by Mulliken population analysis. The surface-substrate distance d is 2.16 Å and 3.42 Å. ΔQ denotes difference of the electron number from the neutral.

		model A $d = 2.16$ Å		model B $d = 2.16$ Å		model A $d = 3.42$ Å	
		Q	ΔQ	Q	ΔQ	Q	ΔQ
C	(graphite layer)	6.00	±0.00	6.00	±0.00	6.00	±0.00
Ti	(1st layer)	21.88	−0.12	21.89	−0.11	21.86	−0.14
C	(2nd layer)	6.18	+0.18	6.19	+0.19	6.20	+0.20
Ti	(3rd layer)	21.88	−0.12	21.88	−0.12	21.90	−0.10
C	(4th layer)	6.04	+0.04	6.04	+0.04	6.03	+0.03

support the charge transfer mechanism from the substrate to the graphite layer proposed for explaining the softening in the phonon structure[145,146]. This is, however, not true. Table 6.1 shows the electronic charges at each atomic site estimated by the Mulliken population analysis[165]. In the TiC layers, electrons are transferred from the Ti atom to the C atom. Degree of the electronic polarization in the outer layers is small compared to that in the inner layers due to depolarization effect[152]-[154]. On the contrary, the charge transfer between the graphite and the substrate does not occur in spite of the short distance between the C atom in the graphite layer and the Ti atom. The graphite layer remains neutral. This result is reasonable, because difference of work function between the bulk graphite surface and the TiC(111) surface is as small as 0.1 eV[155].

These features of the monolayer graphite on TiC(111) are quite different from those of many donor GIC's[138]. In the many donor GIC's, intercalants act merely as a donor of electrons, and the orbital mixing between the graphite and the intercalants can be neglected. In such a case, the rigid band model is valid, where the Fermi level shifts according to the amount of the charge transfer.

In contrast with the GIC's, the charge transfer between the graphite layer and the substrate does not occur in the monolayer graphite on TiC(111) surface. The orbital mixing between the graphite and the substrate results

in the lowering of the π bands. Mechanism of the lowering is change of electronic occupation in the graphite layer from the occupied σ and π states to the unoccupied π^* states as explained below.

By a simple tight-binding calculation, amount of change in electronic charge due to the orbital mixing between the graphite layer and the substrate is estimated as

$$\Delta n_\sigma = -\sum_{\sigma,S}(1-\tilde{\lambda}_S)\left(\frac{t_{\sigma S}}{\varepsilon_S - \varepsilon_\sigma}\right)^2, \tag{6.1}$$

$$\Delta n_\pi = -\sum_{\pi,S}(1-\tilde{\lambda}_S)\left(\frac{t_{\pi S}}{\varepsilon_S - \varepsilon_\pi}\right)^2, \tag{6.2}$$

$$\Delta n_{\pi^*} = \sum_{\pi^*,S}\tilde{\lambda}_S\left(\frac{t_{\pi^* S}}{\varepsilon_S - \varepsilon_{\pi^*}}\right)^2 + \sum_{\pi^*}\tilde{\lambda}_{\pi^*}, \tag{6.3}$$

where σ, π, π^*, and S are labels denoting the occupied σ state, the occupied π state, the unoccupied π^* state of graphite, and the substrate state, respectively. In the above, ε_σ, ε_π, ε_{π^*}, and ε_S are energies of each state, and $t_{\sigma S}$, $t_{\pi S}$, and $t_{\pi^* S}$ are graphite-substrate transfer energies. The quantity λ_S and λ_{π^*} represents occupation of the substrate state and the graphite π^* state, respectively. The values $\lambda = 0$ and $\lambda = 1$ correspond to the unoccupied and the fully occupied state, respectively. The quantities with tilde express those changed from the original values by the graphite-substrate interaction. The sum is taken over all the σ, π, π^*, and substrate states. These are schematically illustrated in Fig. 6.15.

Eqs. (6.1) and (6.2) express reduction of the electronic occupation in the occupied σ and π states of the graphite layer due to the orbital mixing with the unoccupied substrate states. On the other hand, the first term of the right hand side in eq. (6.3) expresses increase of the electronic occupation in the unoccupied π^* states due to the mixing with the occupied substrate states. In the case of the TiC(111) substrate, the substrate band near the Fermi level is the Ti $3d$ band which is metallic and partially occupied as shown in Fig. 6.10(b). This causes the reduction of the electronic charge in the occupied σ and π bands, and the increase in the unoccupied π^* band. Furthermore, the $3d$ bands of the substrate are concentrated in the higher

$t_{\pi^* S}$

ε_{π^*}

E_F

$t_{\pi S}$

ε_S

ε_π

$t_{\sigma S}$

ε_σ

Graphite   Substrate
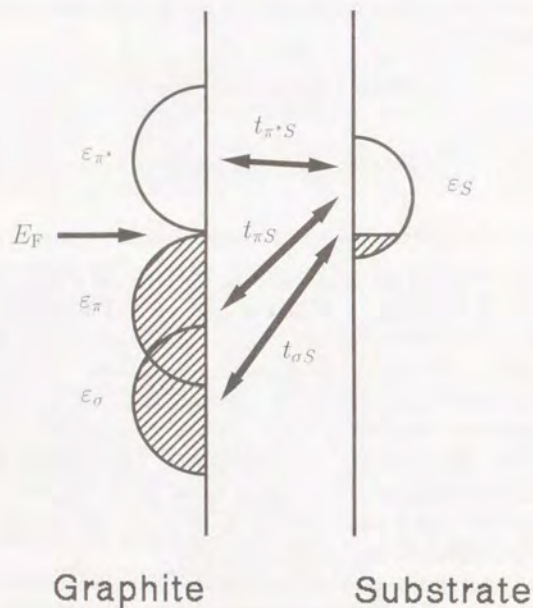
Figure 6.15: Schematic energy levels of graphite and substrate for the monolayer graphite on TiC(111) surface.

energy region above the Fermi level. This favors the lowering of the orbital energy in the lower energy region of the π^* band as

$$\tilde{\varepsilon}_{\pi^*} = \varepsilon_{\pi^*} - \sum_S \frac{t_{\pi^* S}^2}{\varepsilon_S - \varepsilon_{\pi^*}}. \tag{6.4}$$

On the other hand, since the band width of the graphite is wider than that of the substrate $3d$ band, the lowering in the substrate orbital energy due to the mixing with the higher energy part of the graphite band is compensated by the increase due to the mixing with the lower energy part of the graphite band. The orbital energy of the substrate does not change so much. Indeed, this can be verified by comparing Figs. 6.10(b) and 6.13(c). Therefore, the lower energy part of the unoccupied π^* band is lowered under the original Fermi level, and the electronic charge transfers from the occupied substrate bands to the unoccupied π^* band. The second term of the right hand side in eq. (6.3) expresses the increase of the occupation in the π^* band due to this direct charge transfer. These features are seen in the orbital components of the calculated Mulliken charge shown in Table 6.2. Comparing with the bulk graphite, the occupancy in the σ states is reduced, and that of the π states increases in the monolayer graphite. The reduction of the electronic charge in the occupied σ and π bands is compensated by the increase in the unoccupied π^* band, and the graphite layer remains neutral. This is the mechanism of the lowering of the π band without a significant charge transfer from the substrate.

The reduction of the energy in the system due to the graphite-substrate mixing is estimated as

$$\Delta E = - \sum_{\sigma, S} (1 - \lambda_S) \frac{(t_{\sigma S})^2}{\varepsilon_S - \varepsilon_\sigma} - \sum_{\pi, S} (1 - \lambda_S) \frac{(t_{\pi S})^2}{\varepsilon_S - \varepsilon_\pi} - \sum_{\pi^*, S} \lambda_S \frac{(t_{\pi^* S})^2}{\varepsilon_{\pi^*} - \varepsilon_S}$$
$$+ \sum_{\pi^*} (\tilde{\varepsilon}_{\pi^*} - \tilde{\varepsilon}_F) \Delta \lambda_{\pi^*} + \sum_S (\tilde{\varepsilon}_S - \tilde{\varepsilon}_F) \Delta \lambda_S, \tag{6.5}$$

where $\Delta \lambda_{\pi^*}$ and $\Delta \lambda_S$ are difference in the electronic occupation of the π^* and the substrate states, respectively. The first three terms of the right hand side in eq. (6.5) express stabilization due to the orbital mixing between the graphite and the substrate. The fourth and fifth terms express stabilization

Table 6.2: Orbital component of electron numbers in the graphite layer for the model A and B estimated by the Mulliken population analysis. The surface-substrate distance d is 2.16 Å for (a), (b) and 3.42 Å for (c). Types of the C atoms correspond to the numbers in Figure 6.1. ΔQ denotes difference of the electron number from the neutral. For comparison, orbital component calculated for the isolated monolayer graphite without the substrate is shown in (d).

(a) model A ($d = 2.16$ Å)

	$2s$	$2p_\sigma$	$2p_\pi$	σ $(= 2s + 2p_\sigma)$	total $(= 2s + 2p_\sigma + 2p_\pi)$	(ΔQ)
type 1	1.18	1.81	1.01	2.99	3.99	(-0.01)
type 2	1.14	1.75	1.13	2.89	4.02	$(+0.02)$
average	1.17	1.79	1.04	2.96	4.00	(± 0.00)

(b) model B ($d = 2.16$ Å)

	$2s$	$2p_\sigma$	$2p_\pi$	σ $(= 2s + 2p_\sigma)$	total $(= 2s + 2p_\sigma + 2p_\pi)$	(ΔQ)
type 1	1.16	1.78	1.07	2.94	4.01	$(+0.01)$
type 2	1.18	1.81	1.00	2.98	3.98	(-0.02)
type 3	1.18	1.81	1.01	2.99	4.00	(± 0.00)
type 4	1.16	1.79	1.07	2.95	4.01	$(+0.01)$
average	1.17	1.80	1.04	2.96	4.00	(± 0.00)

(c) model A ($d = 3.42$ Å)

	$2s$	$2p_\sigma$	$2p_\pi$	σ $(= 2s + 2p_\sigma)$	total $(= 2s + 2p_\sigma + 2p_\pi)$	(ΔQ)
type 1	1.19	1.81	1.00	3.00	4.01	$(+0.01)$
type 2	1.19	1.81	1.00	2.99	4.00	(± 0.00)
average	1.19	1.81	1.00	3.00	4.00	(± 0.00)

(d) isolated monolayer graphite

	$2s$	$2p_\sigma$	$2p_\pi$	σ $(= 2s + 2p_\sigma)$	total $(= 2s + 2p_\sigma + 2p_\pi)$	(ΔQ)
graphite	1.19	1.82	1.00	3.00	4.00	(± 0.00)

due to the charge transfer from the substrate to the graphite. The latter terms contribute to the stabilization, because $\Delta\lambda_{\pi^*} > 0$ and $\bar{\varepsilon}_{\pi^*} - \bar{\varepsilon}_F < 0$ for the graphite, and $\Delta\lambda_S < 0$ and $\bar{\varepsilon}_S - \bar{\varepsilon}_F > 0$ for the substrate. Since the energy difference $\varepsilon_{\pi^*} - \varepsilon_S$ is smaller and the transfer energy $t_{\pi^* S}$ is larger compared with other terms in the case of the monolayer graphite on TiC(111) surface, the third term is the main term of the stabilization by the orbital mixing.

This mechanism explains also the anomalous expansion of the C-C bond length in the monolayer graphite comparing to the GIC's. In the GIC, the mechanism of the bond-length expansion is the π-bond weakening due to the charge transfer into the unoccupied π^* band[151]. The σ bond is not so much influenced by the charge transfer. In the case of the monolayer graphite on metal substrates, the mechanism of the bond-length expansion is the reduction of the electronic occupation in the σ states due to the coupling with the substrate. The electron extraction from the σ states weakens the σ bond. Influence of the σ bond on the bond-length expansion would be much stronger than that of the π bond, which explains the fact that the bond length expansion of the monolayer graphite is anomalously larger than that of GIC's. This is similar to the donation and back-donation mechanism of CO chemisorption on transition-metal surfaces[166,167]. The present system has some relation to the alkali-metal chemisorption on metal surfaces in the point that the orbital bonding between the overlayer and the substrate is more important than the charge transfer[168].

Due to the relatively strong interaction with the substrate, the C atom of the graphite layer is changed from the sp^2 configuration. Since the π-Ti interaction is stronger than the σ-Ti interaction, the graphite-substrate interaction favors the stabilization of the orbital energy of the π states rather than the σ states. In a sense, the C atom of the graphite layer becomes like a carbidic atom in the TiC. In this respect, the fairly short distance between the graphite layer and the substrate compared with the interlayer spacing in the bulk graphite is not so unreasonable. The interaction, however, is not so strong as the C-C interaction in the graphite layer, and the band dispersion similar to the bulk graphite still remains.

The stable structure is determined by a balance between the energy gain by the graphite-substrate mixing and the energy loss by the weakening of the C-C bond in the graphite layer caused by the graphite-substrate mixing. For the case of the monolayer graphite on TiC(100) surface, the energy gain by the graphite-substrate mixing is small, since the surface bands of TiC(100) surface near the Fermi level are empty as can be seen in Fig. 6.5[152]. In such a case, the λ_S is zero and the charge transfer from the substrate to the graphite does not occur. The energy gain by the third, fourth, and fifth terms in eq. (6.5) is lost. This explains that the phonon structure of the monolayer graphite on TiC(100) surface does not show the softening and the lattice constant is almost the same as the bulk graphite[145,146].

It may be supposed that since the bonding between the graphite layer and the substrate is essential, the obtained results may depend on the lateral position of the graphite layer relative to the substrate. The band calculation for the model B shown in Fig. 6.7(b) is also performed. Figure 6.16 shows the calculated band structure for the case that the graphite-substrate distance is 2.16 Å. Contrary to the above anticipation, the obtained band structure is almost the same as that of the model A shown in Fig. 6.10(a). As shown in Table 6.1, the calculated Mulliken charges also do not differ from those of the model A within computational accuracy. The reason for these results is explained as follows.

Not all the C atoms in the graphite layer of both the model A and the model B are equivalent. For model A, there are two kinds of C atoms. One is situated just above the substrate Ti atom and the other is above the middle of two Ti atoms. The former is the position where the interaction with the Ti atom is strongest, and the latter is the weakest position. On the other hand, the C atoms in the model B are positioned where the strength of the interaction with the Ti atom is middle of the two kind of atoms in the model A. On an average over the atoms, the strength of the interaction with the substrate is roughly equal among these models, and the overall features of the band structures are not so different. This is also seen in the calculated Mulliken charges as shown in Table 6.2, where the charges are site-dependent and are different between the two models, but the averaged
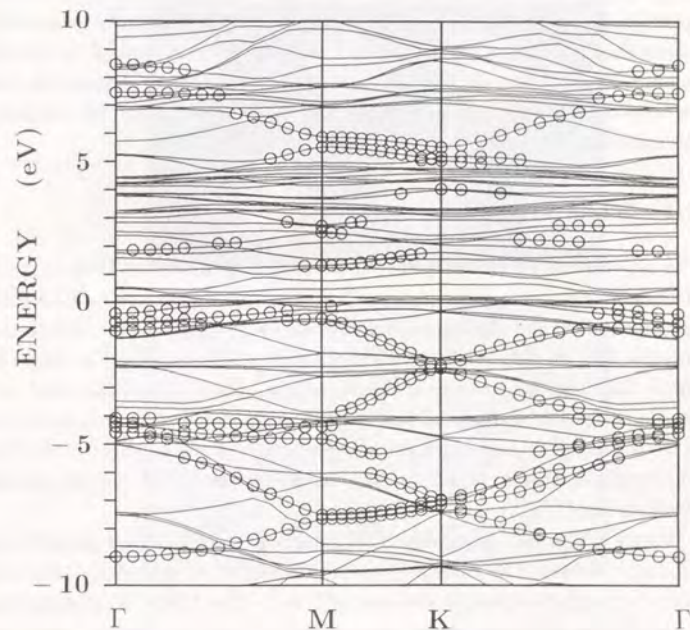
Figure 6.16: Calculated π band structure of the monolayer graphite on TiC(111) surface for the model B, when the graphite-substrate distance is 2.16 Å. Open circles indicate the bands, whose $2p_z$ component of the graphite layer is larger than 25 %.

values over the unit cell do not differ. Appearance of this averaging effect even with such a relatively small unit cell is ascribed to the lattice mismatch between the overlayer and the substrate. This is because the relative positions of atoms between the overlayer and the substrate tend to be random as the degree of the mismatch increases. The small difference of the calculated band dispersions between the different graphite-substrate geometries means that broadening of the ARUPS peaks of graphite caused by the incommensurate substrate is small, and that distinct band dispersions can be observed even in the present system with the strong substrate-overlayer interaction.

6.4   STM image

The experimental STM image of the monolayer graphite on TiC(111) surface shows not the atomic image of carbons but the superstructure with two kinds of period which are different from the lattice constant of both the graphite and the substrate[84]. To investigate what is observed in the STM image, the tunneling current is calculated from the results of the band calculations. In the present calculation, the microscopic electronic structure of tip is not considered, since the superstructure is not an effect of the tip. The tunneling current is calculated from the surface LDOS via the formula shown in eq. (2.7).

Figure 6.17 shows calculated STM images of the monolayer graphite on TiC(111) surface. The calculation is performed for the model A in Fig. 6.7 with the graphite-substrate distance of 2.16 Å. The LDOS is calculated at points 5.3 Å above the graphite layer. The tunneling current is calculated for the sample bias voltage (a) +0.5 V and (b) −0.5 V. The calculated STM image of the monolayer graphite on TiC(111) surface shows the triangular pattern, which is different from the honeycomb atomic structure of graphite. This is similar to the STM image of the bulk graphite. However, the peak regions of the tunneling current forms a 2×2 structure of the original graphite unit cell. The period of the pattern is 5.3 Å. The calculated STM image reproduces well the features of the experimental STM images showing

(a)
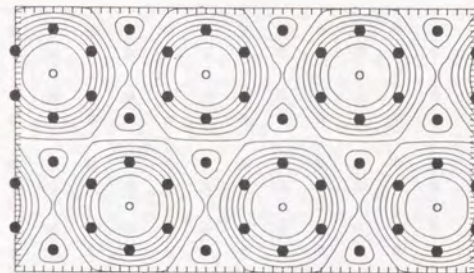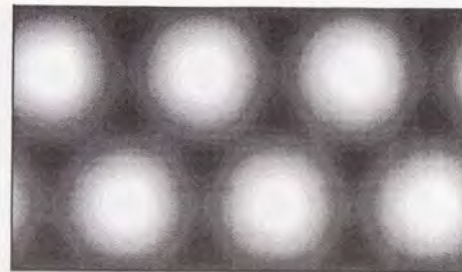
(b)
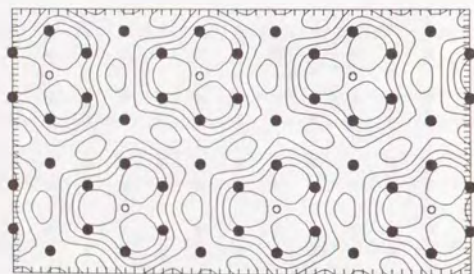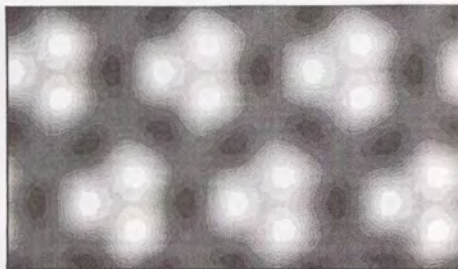
(a)
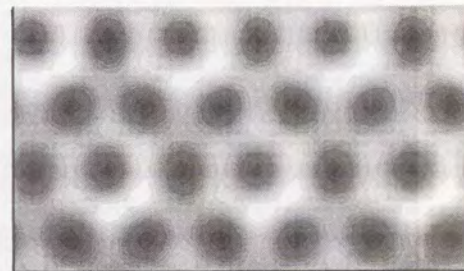
Figure 6.17: Calculated STM image of the monolayer graphite on TiC(111) surface for the model A, when the graphite-substrate distance is 2.16 Å. Tunneling current is calculated for the sample bias voltage (a) +0.5 V and (b) −0.5 V. Upper and lower part of the figures are a gray-scale image and a contour map, respectively. Spacing of the contours is 1/10 of current maximum. Closed and open circles indicate the position of the C atoms of the graphite layer and the Ti atoms of the first substrate layer. The images show a triangular-lattice pattern.

(b)
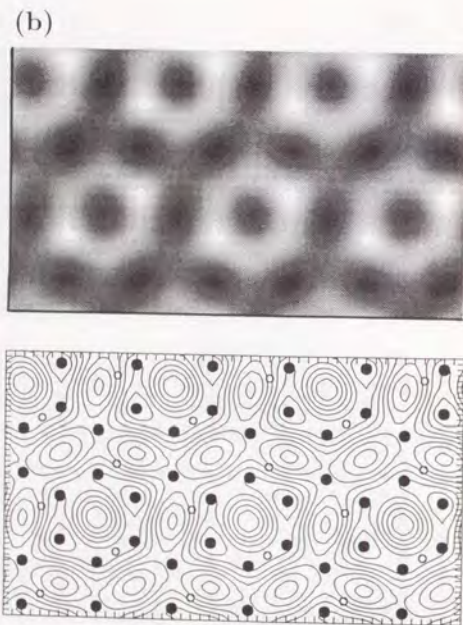
Figure 6.18: Calculated STM image of the monolayer graphite on TiC(111) surface for the model B, when the graphite-substrate distance is 2.16 Å. Tunneling current is calculated for the sample bias voltage (a) +0.5 V and (b) −0.5 V. Other conditions are the same as Fig. 6.17. The images changes from a honeycomb-lattice to a triangular-lattice structure depending on the bias voltage.

the triangular pattern with period of about 5 Å[84].

An interesting feature of this image is that the peaks are located not at the C atomic sites but at the hollow sites surrounded by the six C atoms. The individual atomic image of the C atoms is not seen, which is similar to the STM image of benzene molecule[169]-[173]. The feature of the STM image depends on the height of the view point from the surface. When the height is taken as 2.6 Å, the intensity at the hollow site decreases and the region with large current intensity is located at the C atomic sites. The STM image becomes like a doughnut.

The tunneling current takes the minimum value at the remaining two C sites. Hereafter, the two C sites and the other bright sites are called minor site and major site, respectively. The site dependence of the tunneling current reflects the site dependence of interaction strength with the substrate. The Ti atoms of the substrate are located just below the minor sites, but are not located below the major sites. The orbital hybridization between the C atoms and the Ti atoms forms the bonding and the anti-bonding orbitals, and tends to reduce number of states near the Fermi level. Since interaction of the minor site with the substrate is stronger than that of the major sites, the tunneling current at the minor sites is smaller. These features do not show a significant energy dependence within about ±1 eV around the Fermi level as shown in Fig. 6.17(b).

On the contrary, the STM image for the model B shows an energy dependence as shown in Fig. 6.18. The STM image of the unoccupied states shows a honeycomb structure which is the lattice image of graphite, and the image of the occupied states shows the 2×2 structure similar to that of the model A. However, the regions of the weakest tunneling current in the model B are located not above the C atomic sites but above the hollow sites. Comparing the model A and B, it is reasonable that the 2×2 structure tends to appear for the model A, because the site difference of interaction between the graphite C atoms and the substrate is larger in the model A.

The experimental STM images of the monolayer graphite on TiC(111) surface depend on the polarity of the applied bias voltage[84]. The image of the unoccupied states shows only the triangular structure with the period

of about 5 Å. In the image of the occupied states, a modulation with a period as long as 21 Å is added to the triangular structure, and the STM image shows the moiré pattern as shown in Fig. 6.1. The calculated STM images of the unoccupied states show the 2×2 triangular pattern both for the model A and B, and the images of the occupied states change depending on the models. This may indirectly explain the fact that the moiré pattern is seen in the occupied state and is not seen in the unoccupied state, but it is not so clear by the present small unit cell. To discuss the moiré pattern explicitly, an electronic structure calculation with a large unit cell is needed. At present, it is difficult to perform a first-principles band calculation with such a large unit cell. Instead, a tight-binding calculation is performed as shown in the next section.

6.5 Tight-binding calculation of STM image of monolayer graphite: moiré pattern

6.5.1 Structure model and method of calculation

In this section, the superstructure in the STM image of the monolayer graphite on TiC(111) is discussed. There are two standpoints for explaining the superstructure. One is superposition of the tunneling currents from the overlayer and the substrate. In this view, electrons tunnel directly from the substrate as well as from the overlayer. The other view is that the electronic structure of the overlayer is modulated by interaction with the substrate. Superstructures in the STM image reflect change in the electronic structure of the overlayer. Since tunneling current exponentially depends on the tip-sample distance, the tunneling current flowing between the substrate and the tip would be much less than that between the overlayer and the tip. Therefore, the latter view seems to be more plausible than the former.

To discuss the superstructures, an electronic calculation of a system with a large unit cell is necessary. However, it is difficult to perform a first-principles band calculation for such a large system. In the preceding section, the electronic structure of the monolayer graphite on TiC(111) surface has

Table 6.3: Tight-binding parameters of monolayer graphite on TiV(111) surface used in the present study. The values are expressed in unit of t_{GR} which corresponds to 2.67 eV.

ε_{GR}	ε_{Ti}	t_{GR}	t_{Ti}	t_{GR-Ti}
0.0	1.2	1.0	0.1	0.5

been investigated with the 2×2 super cell, where it has been shown that the results obtained do not change qualitatively against the lateral shift of the graphite layer over the substrate. This allows to apply the results obtained with the small unit cell to a large system. Based on this reason, a tight-binding calculation of the monolayer graphite on TiC(111) surface has been performed.

Parameters for the tight-binding calculation is determined so as to reproduce the band structure obtained by the first-principles calculation. For the graphite layer, only the π orbital is taken into account and the σ orbital is neglected, because the electronic states of graphite near the Fermi level consist of only the π state. For the TiC(111) substrate, only the top layer Ti is taken into account, because present interest focuses on change of the electronic states of the graphite layer caused by interaction with the substrate. Moreover, only the $d_{3z^2-r^2}$ orbital of the Ti atom is taken into account, because the orbital mixing between the graphite π component and the Ti $d_{3z^2-r^2}$ component is strongest.

Unit cell and parameters used in the present tight-binding calculation are shown in Fig. 6.19 and Table 6.3, respectively. The unit cell corresponds to a 7×7 super cell of the TiC(111) substrate and to a $5\sqrt{3} \times 5\sqrt{3}$ super cell of the pristine graphite. The unit cell contains 150 C atoms and 49 Ti atoms. Lattice constant of the cell is 21.7 Å. In the preceding first-principles calculation, the band calculation has been performed by changing the lattice constant of the overlayer graphite by 6 % and by using a 2×2 unit cell of pristine graphite. In the tight-binding calculation, the change of the lattice constant of the graphite layer is reduced to be less than 1 % by using the large unit cell.

The tight-binding parameters are determined as follows. From Fig. 6.13(b)
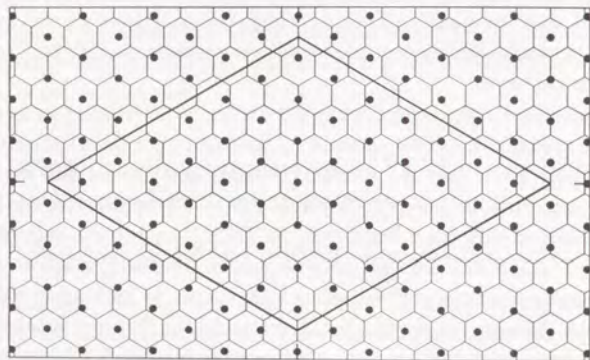
Figure 6.19: Unit cell of the monolayer graphite on TiC(111) surface used in the tight-binding calculation. The graphite lattice is expressed by the honeycomb structure. Closed circles indicate the first layer Ti atoms. Rhombus shows the unit cell.

which shows the band structure of the monolayer graphite on TiC(111) surface when the graphite-substrate interaction can be neglected, band widths of the graphite π band and the Ti d band are estimated as 16 eV and 4 eV, respectively. The center of the Ti d band is situated at about 2 eV above the K point of graphite. From the band widths, transfer energies of the graphite t_{GR} and the Ti t_{Ti} are determined as 2.67 eV and 0.44 eV, respectively. The on-site energy of the Ti orbital ε_{Ti} is 2.67 eV measured from that of the graphite. Hereafter, energy is expressed in unit of the transfer energy of graphite. In this unit, the parameters t_{GR}, t_{Ti}, ε_{Ti} are 1.0, 0.16, 1.0, respectively. The transfer energy between the graphite and the Ti is determined so as to reproduce well the first-principles band structure shown in Fig. 6.10(a) which is one for the case that the graphite-substrate distance is small and their interaction is strong. The parameters shown in Table 6.3 are optimal ones.

The determined transfer t_{GR-Ti} is fairly large. It is larger than the transfer energy of the Ti, and is about half of that of the graphite. The selected parameter is justified by a calculated band structure shown in Fig. 6.20. This band structure is obtained by a tight-binding calculation using the above parameters for the 2×2 unit cell used in the first-principles calculation. The calculated band structure qualitatively reproduces one obtained by the first-principles calculation. PDOS of this band structure is also shown in Fig. 6.21.

In performing a tight-banding calculation for the large unit cell, the transfer energy between Ti and C should vary depending on the Ti-C distance. In the present calculation, the transfer energy is calculated by a formula:

$$t_{GR-Ti} = 0.5 \exp[-1.9(d - 4.09)], \tag{6.6}$$

where d is the C-Ti distance. Length is expressed in the atomic unit (a.u.). The decay constant 1.9 a.u. is an average value of 1.7 a.u. and 2.1 a.u. which are decay constants of radial wavefunctions of C $2p$ and Ti $3d$ orbitals, respectively. They are determined by fitting to numerical radial wavefunctions obtained in the first-principles calculation.
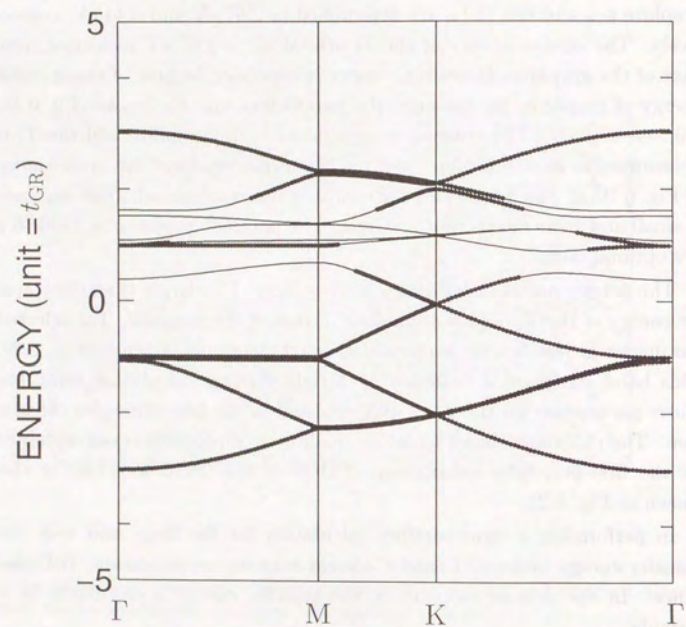
Figure 6.20: Band structure of the monolayer graphite on TiC(111) surface obtained by a tight-binding calculation for the 2×2 unit cell of pristine graphite shown in Fig. 6.7. Open circles indicate the bands whose π component of the graphite layer is larger than 25 %.
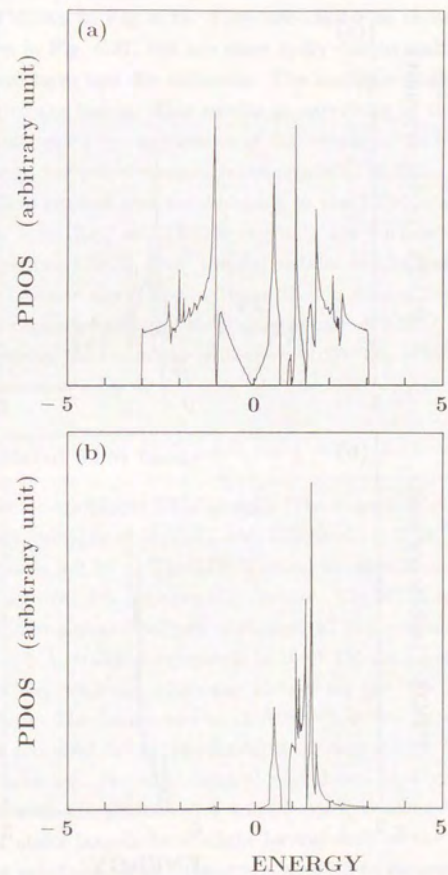

Figure 6.21: PDOS obtained by the tight-binding calculation for the 2×2 unit cell shown in Fig. 6.7; (a) graphite π component (b) substrate Ti component. Energy is expressed in unit of transfer energy T_{GR} of graphite.
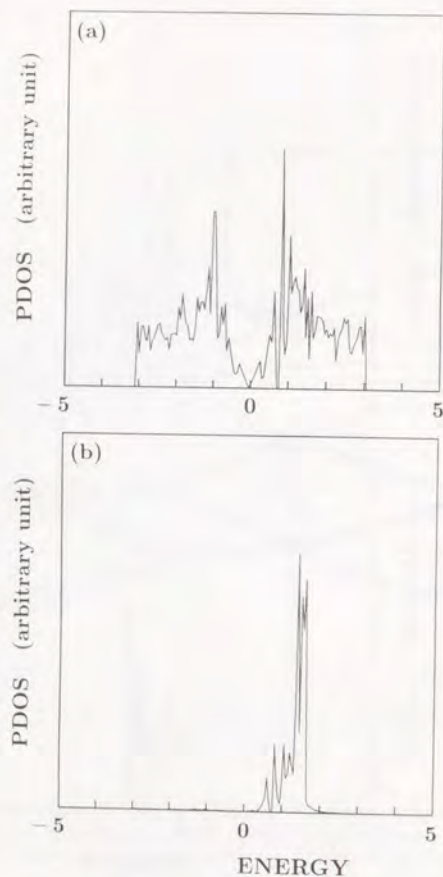
Figure 6.22: PDOS obtained by the tight-binding calculation for the large unit cell shown in Fig. 6.19; (a) graphite π component (b) substrate Ti component. Energy is expressed in unit of transfer energy T_{GR} of graphite.

Figure 6.22 shows calculated PDOS's at the C and the Ti site for the large unit cell shown in Fig. 6.19. They are similar to those for the small unit cell shown in Fig. 6.21, but are more spiky due to multiple-scattering between the overlayer and the substrate. The multiple-scattering acts also as broadening of the bands. This results in narrowing of the width of the band gaps which open by interaction of the overlayer and the substrate. This is similar to the pseudo-gap in quasi-crystals[174,175].

The tunneling current and conductance in the STM are calculated by the formula of eqs. (2.6) and (2.7) using only the surface LDOS. In calculating the surface LDOS, only the $2p_z$ orbital of the graphite is taken into account, because the tunneling from the outermost layer of the surface mainly contributes to the tunneling current. A Slater type orbital is used for expressing the radial wavefunction of the $2p_z$ orbital. The decay constant is chosen as 1.7 a.u.

6.5.2 Calculated STM image

Figure 6.23 shows calculated STM images. The tunneling current is calculated at surface voltages of (a) 0.25, (b) 1.75, and (c) 0.25. The graphite-substrate distance is 2.16 Å. The LDOS image is calculated at positions of (a) (b) 5.3 Å and (c) 2.6 Å above the surface. The STM image shown in Fig. 6.23(a) shows a moiré pattern consisting of two periods. The shorter period is about 5 Å, which corresponds to the STM image obtained by the first-principles electronic-structure calculation for the 2×2 super cell of pristine graphite. The longer one is 21 Å which is the lattice constant of the large unit cell used in the present tight-binding study. The calculated image reproduces well the experimental one shown in Fig. 6.1(a), where moiré pattern with the periods of 5 and 21 Å[84] is seen. The calculated moiré pattern shifts largely by a slight lateral shift of the graphite layer parallel to the substrate. This property is specific to incommensurate and large unit cell systems[87].

When the bias voltage is changed, a different type of super-structure is obtained. Figure 6.23(b) shows a calculated image when the bias voltage

(a)
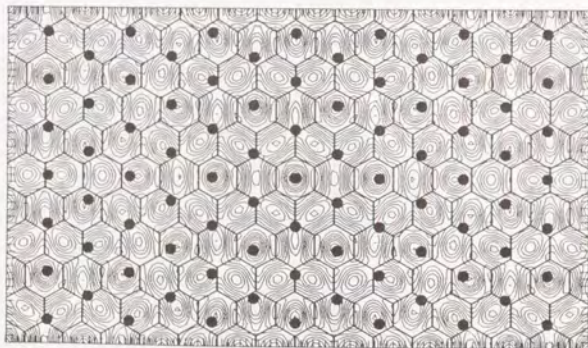
(b)
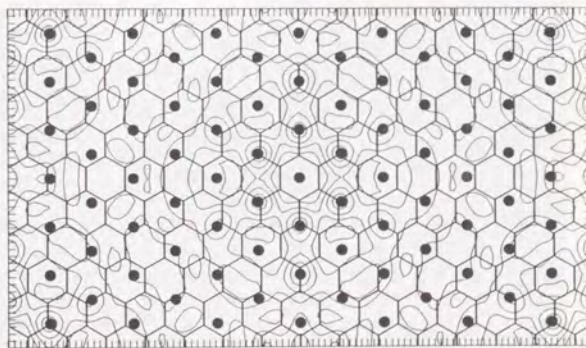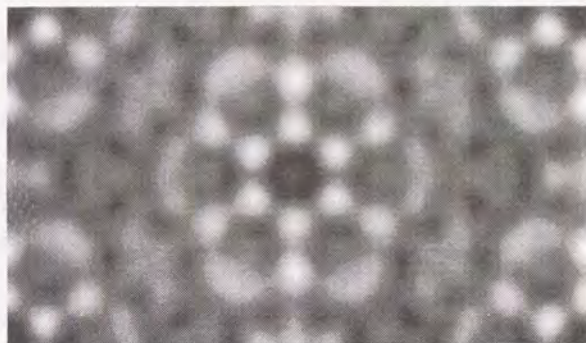
(c)
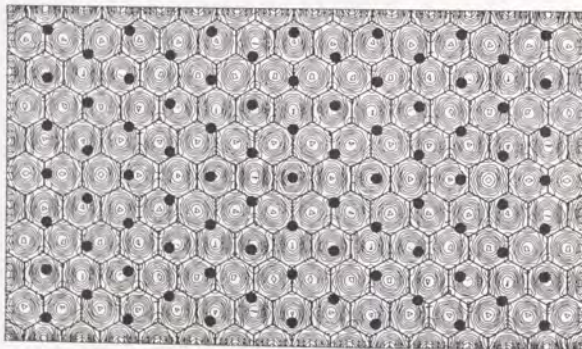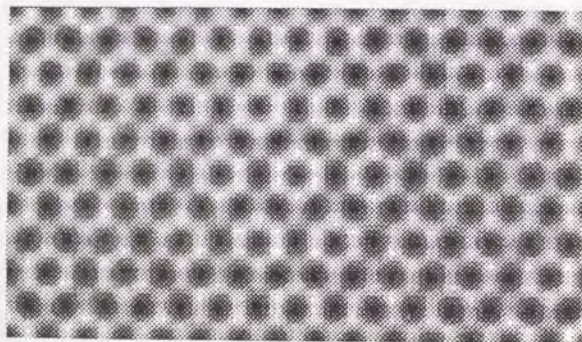
Figure 6.23: Calculated STM images of the monolayer graphite on TiC(111) surface. Bias voltage is (a) 0.25, (b) 1.75, and (c) 0.25. The LDOS is evaluated at positions of (a) (b) 5.3 Å and (c) 2.6 Å above the surface. The graphite-substrate distance is 2.16 Å. Hexagonal lattice and open circles in the lower part indicate the atomic structure of the graphite layer and the positions of the substrate Ti atoms, respectively.

is 1.75. This image can be interpreted as an image of a hexagonal lattice modulated with the period of the unit cell. Period of the hexagonal lattice is about 5.4 Å, and position of the bright spots is atomic site of the substrate Ti. Since the atomic image of the substrate is obtained, this image can be regarded as an example of transparency of substrates through adsorbed layers[77].

The moiré pattern disappears when the tip is scanned near the surface. Figure 6.23(c) shows a STM image when the LDOS is calculated at positions of 2.6 Å above the surface. The bias voltage is the same as that of the image shown in Fig. 6.23(a). The calculated image shows a hexagonal pattern of the graphite atomic lattice, and the influence of the substrate is not seen. This result may be explained intuitively by an ordinary fact that a smaller structure tends to be hardly observed as the distance from the surface increases. More precisely, it is explained by a general fact that higher two-dimensional Fourier components parallel to surface decay faster in vacuum region shown as follows.

A wavefunction of surface is expanded in terms of two-dimensional reciprocal vectors as

$$\Psi_{\mathbf{k}_{\parallel},z}(\mathbf{r}_{\parallel}) = e^{i\mathbf{k}_{\parallel} \cdot \mathbf{r}_{\parallel}} \sum_{\mathbf{G}_{\parallel}} A_{\mathbf{G}_{\parallel}}(z) e^{i\mathbf{G}_{\parallel} \cdot \mathbf{r}_{\parallel}}. \tag{6.7}$$

In the vacuum region, the coefficient $A_{\mathbf{G}_{\parallel}}(z)$ decays as

$$A_{\mathbf{G}_{\parallel}}(z) \sim e^{-\lambda_{\mathbf{G}_{\parallel}} z}, \tag{6.8}$$

where the decay constant is given as

$$\lambda_{\mathbf{G}_{\parallel}} = \sqrt{\frac{2m|E|}{\hbar^2} + \mathbf{G}_{\parallel}^2}. \tag{6.9}$$

Since higher Fourier components decay faster, structures with longer wavelength tend to be magnified as the distance from the surface increases. The observation of the moiré pattern means that the STM tip is scanned at positions not near the surface. Relation between the distance of the tip from the surface and the size of the observed structures provides information on operating conditions of STM.

Even when the tip is situated at positions of 5.3 Å above the surface, some calculated STM images show the hexagonal pattern of the graphite atomic structure. Calculated images at large negative surface voltage show patterns similar to that of Fig. 6.23(c). Around this energy region, orbital mixing between the π orbital of graphite and the d orbital of substrate Ti is weak, and the electronic states of the graphite layer is not much influenced by the substrate. The STM image depends strongly on the bias voltage. The strongly bias-dependent STM images have been reported for benzene molecules on layered materials[169]-[173].

The STM image depends also on the graphite-substrate distance. STM images are calculated for the case that the graphite-substrate distance is 3.42 Å. This value is almost the same as the interlayer distance of pristine graphite. The calculated STM images show a hexagonal pattern of the graphite atomic structure similar to Fig. 6.23(c). When the distance is large and the graphite-substrate interaction is small, the hexagonal pattern is obtained independent of the bias voltage. Since the hexagonal pattern is not observed in the experimental STM image of the monolayer graphite on TiC(111) surface, this result suggests that the graphite-substrate distance is not so large as 3.42 Å, and supports the results of the first-principles calculation.

Since the current image is obtained by summing up electronic states over a finite energy range as shown in eq. (2.7), the conductance image is not necessarily the same as the current image. Figure 6.24 shows calculated conductance images. The LDOS is calculated at positions of 5.3 Å above the surface. The energy of the LDOS is (a) 0.5 and (b) 1.5. The graphite-substrate distance is 2.16 Å. At low bias voltage, conductance images are similar to current images. As the bias voltage increases, difference between current images and conductance images tends to be large. For example, calculated current images at large negative surface bias show the hexagonal pattern of the graphite atomic structure, but conductance images at the same bias show moiré patterns. In the current image, the hexagonal pattern is recovered by superposition of the conductance images which show various types of moiré pattern peaking at different points in the unit cell. The

conductance image is more convenient for discussing the electronic structure at a specific energy.

In the present calculation, the transfer energy between the graphite and the Ti is taken as a half of that between the graphite π orbitals, because it reproduces well the first-principles band calculation. Apart from realistic values for the parameters, STM images are calculated for the case that the transfer energy between the graphite and the Ti is the same as that of the graphite π orbitals. Figure 6.25 shows calculated conductance images. The bias voltage is (a) -1.0, (b) 1.25, and (c) 2.0. The LDOS is calculated at points of 5.3 Å above the surface. Figure 6.25(a) shows a moiré pattern similar to Fig. 6.23(a). Influence of the stronger graphite-substrate interaction appears in amplification of the structure with longer wavelength. The moiré pattern becomes more distinct. The images in Fig. 6.25(b) and (c) have no trace of the atomic structure of graphite. The peak of the image in Fig. 6.25(c) is localized at a localized region in the unit cell. This result can be explained by the strong multiple scattering between the graphite layer and the substrate. The localized feature is not clear in the current image at the same bias voltage as shown in Fig. 6.26, because the current image is superposition of the conductance images.

These features are more evident in Fourier spectra of these STM images. The Fourier spectrum is defined as

$$\tilde{I}(m,n) = \frac{1}{\Omega} \int_{\text{unit cell}} dx dy \, I(x,y) e^{i\mathbf{G}_\parallel \cdot \mathbf{r}_\parallel}, \qquad (6.10)$$

$$\mathbf{G}_\parallel = m\mathbf{g}_1 + n\mathbf{g}_2, \qquad (6.11)$$

where $\mathbf{g}_1$ and $\mathbf{g}_2$ are two-dimensional primitive reciprocal vectors. Figure 6.27 shows two-dimensional Fourier spectra. As shown in Fig. 6.27(a), the Fourier spectrum corresponding to the hexagonal STM image has distinct peaks at the positions of the reciprocal lattice of graphite. In the spectrum corresponding to the moiré pattern shown in Fig. 6.27(b), peaks of the longer wavelength are comparable to those of the graphite lattice. As shown in Fig. 6.27(c), the spectrum corresponding to the localized image has peaks at various wavelengths which have nothing to do with the graphite lattice.
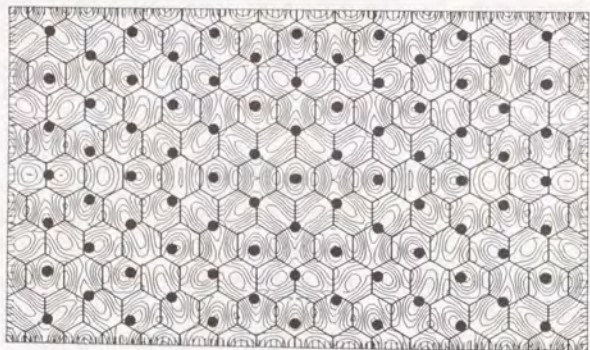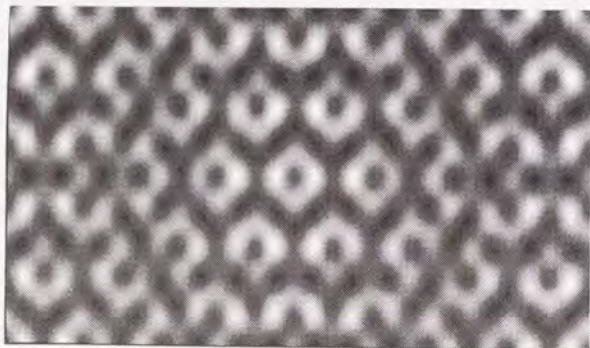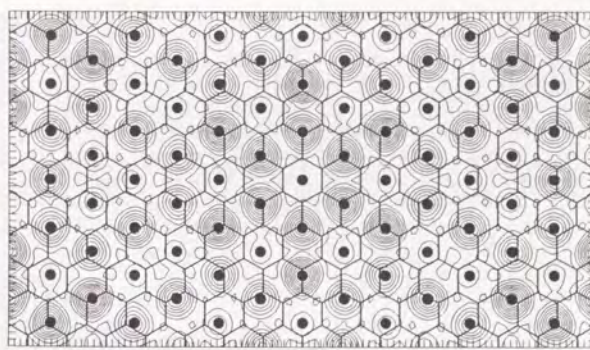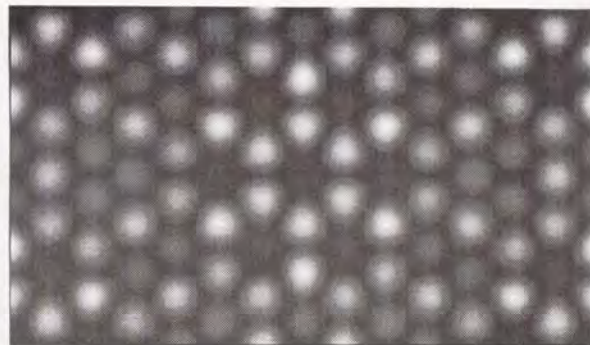
Figure 6.24: Calculated conductance images of the monolayer graphite on TiC(111) surface. Bias voltage is (a) 0.5 and (b) 1.5. The LDOS is evaluated at positions of 5.3 Å above the surface. The graphite-substrate distance is 2.16 Å. Hexagonal lattice and open circles in the lower part indicate the atomic structure of the graphite layer and the positions of the substrate Ti atoms, respectively.

(a)
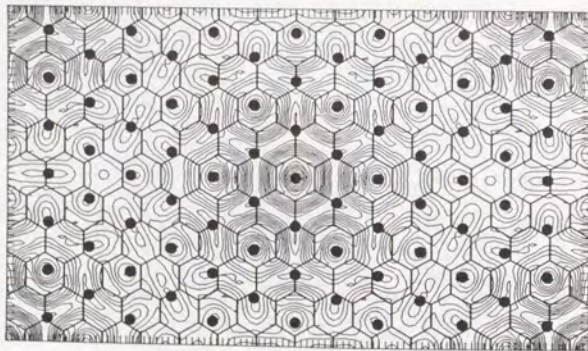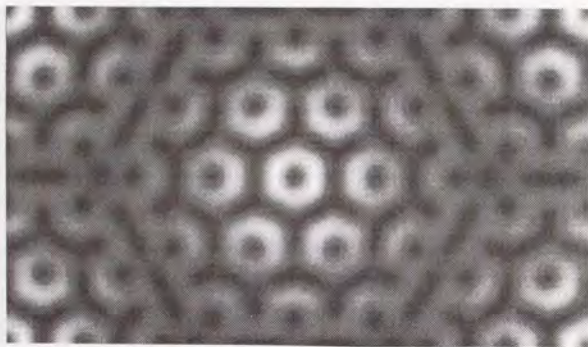
(b)
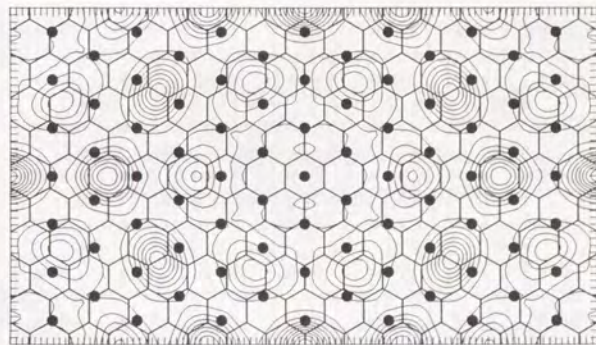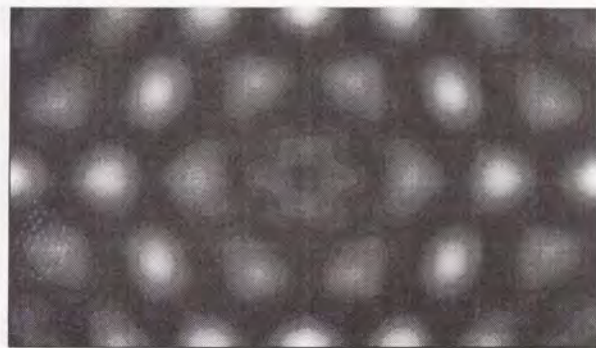
(c)
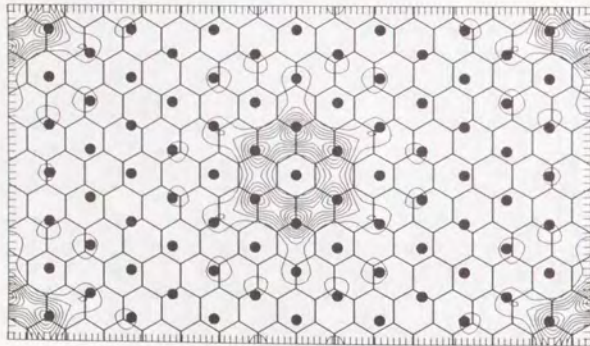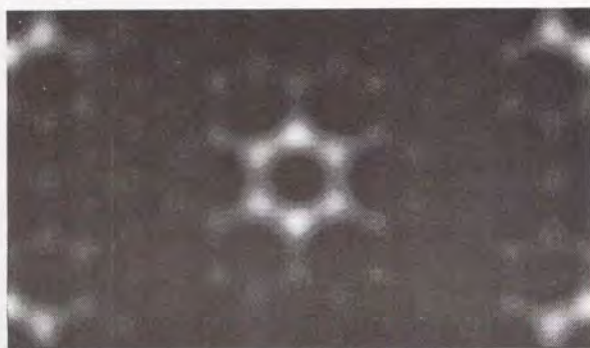
Figure 6.25: Calculated conductance images of the monolayer graphite on TiC(111) surface when the graphite-substrate transfer t_{GR-Ti} is taken to be the same as the π band transfer of graphite. Bias voltage is (a) -1.0, (b) 1.25, and (c) 2.0. The LDOS is evaluated at positions of 5.3 Å above the surface. The graphite-substrate distance is 2.16 Å. Hexagonal lattice and open circles in the lower part indicate the atomic structure of the graphite layer and the positions of the substrate Ti atoms.
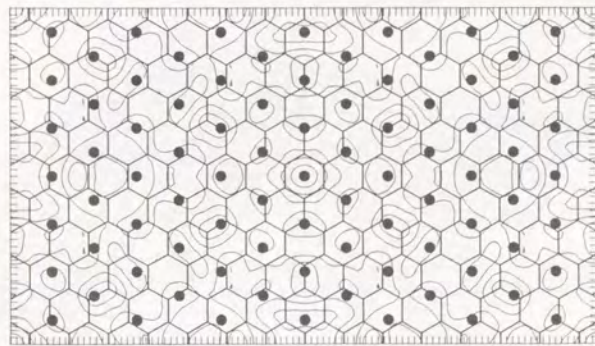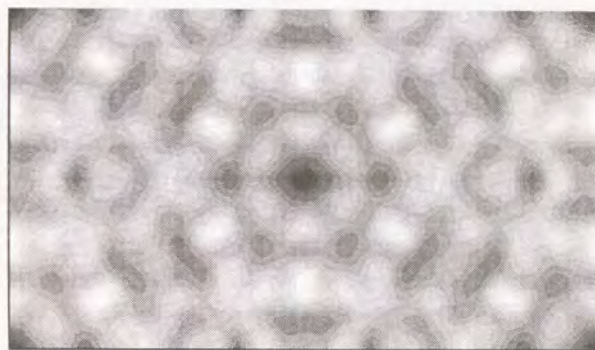
Figure 6.26: Calculated current images of the monolayer graphite on TiC(111) surface when the graphite-substrate transfer t_{GR-Ti} is taken to be the same as the π band transfer of graphite. Bias voltage is 3.0. The LDOS is evaluated at positions of 5.3 Å above the surface. The graphite-substrate distance is 2.16 Å. Hexagonal lattice and open circles in the lower part indicate the atomic structure of the graphite layer and the positions of the substrate Ti atoms.

(a)

$\tilde{I}(m, n)$

arb. unit

15

m 0

15

0 n

−15

−15

(b)

$\tilde{I}(m, n)$

arb. unit

15

m 0

15

0 n

−15

−15

(c)

$\tilde{I}(m, n)$

arb. unit

15

m 0

15

0 n

−15

−15
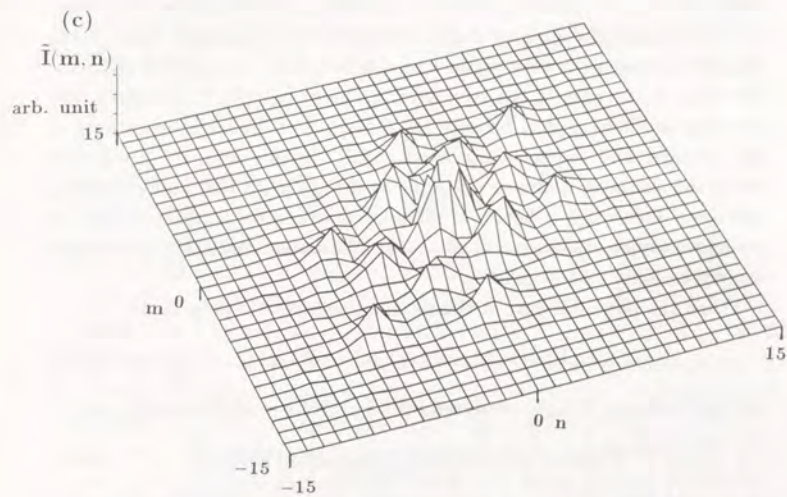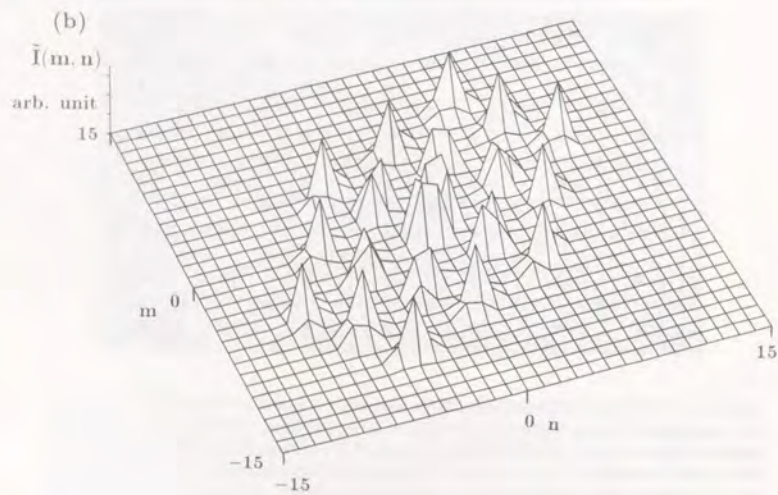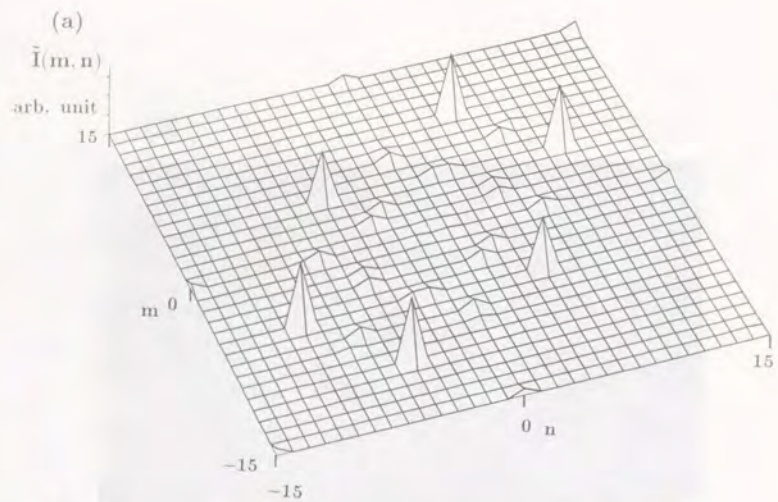
Figure 6.27: Intensity maps of two-dimensional Fourier spectrum calculated from the STM images. The Fourier spectra of (a), (b), and (c) are corresponding to the STM images shown in Fig. 6.23(c), Fig. 6.25(a), and Fig. 6.25(c), respectively.

Moiré patterns may be interpreted intuitively in terms of a beat of two waves:

$$\cos(k_1 x) + \cos(k_2 x) = 2\cos(\delta k x)\cos(k x), \tag{6.12}$$

where $\delta k \equiv (k_1 - k_2)/2$ and $k \equiv (k_1 + k_2)/2$. When the difference of the wave vectors δk is small compared to the average k, right-hand side of eq. (6.12) expresses a wave with wave vector k modulated with a long period of $2\pi/\delta k$. However, in the case of the monolayer graphite on TiC(111) surface, the situation is not so simple, because the difference of the lattice constants of the overlayer and the substrate is not small. In this case, the 2×2 unit cell of the overlayer is almost the same as the $\sqrt{3} \times \sqrt{3}$-R30 unit cell of the substrate. Generally, behavior of modulated structures is not so simple as the above simple case shown in eq. (6.12). We demonstrate this by a simple one-dimensional case as follows.

When the potential part of Hamiltonian consists of two periods:

$$V(x) = V_1 \cos(k_1 x) + V_2 \cos(k_2 x), \tag{6.13}$$

the wavefunction $\Psi(x)$ is expressed in the nearly free approximation as

$$\Psi(x) \sim 1 - C_1 \cos(k_1 x) - C_2 \cos(k_2 x) \equiv F(x). \tag{6.14}$$

In the above, V_1, V_2, C_1, C_2 are constants. As an example, we consider a case that the period of the potential V_2 is about twice of that of V_1, i.e., $k_2 \sim k_1/2$. When k_2 is exactly equal to $k_1/2$, $\Psi(x)$ expresses a wave with a period of $2\pi/k_1 \cdot 2$ as shown in Fig. 6.28(a). This wave has local minima at

$$x = \frac{2\pi}{k_1} \cdot 2n, \quad n : \text{integer}, \tag{6.15}$$

and

$$x = \frac{2\pi}{k_1} \cdot (2n + 1), \quad n : \text{integer}. \tag{6.16}$$

When k_2 is slightly different from $k_1/2$ as $k_2 = k_1/2 + \varepsilon$, $F(x)$ has following values at the above local minima

$$F(x) = 1 - C_1 - C_2 \cos(\varepsilon x) \quad \text{for } x = \frac{2\pi}{k_1} \cdot 2n, \tag{6.17}$$

116
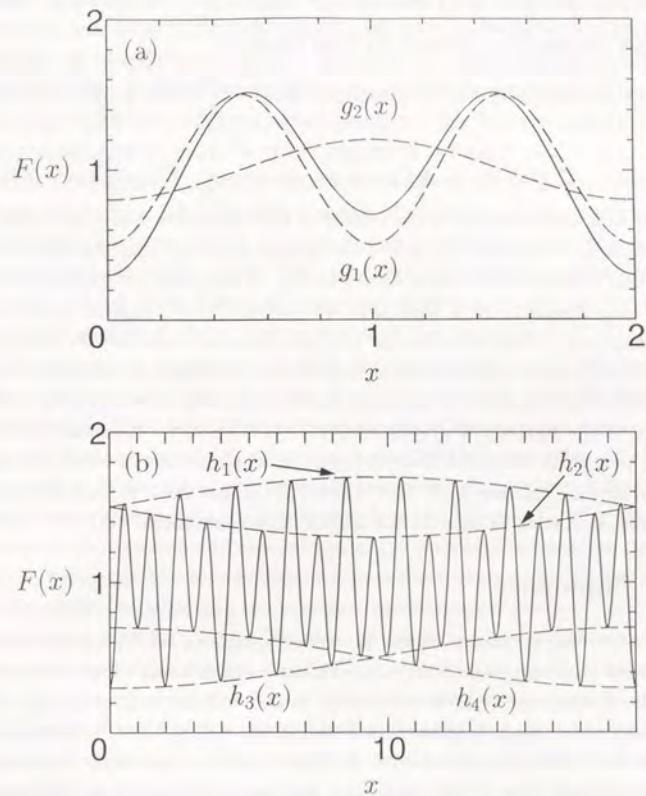
Figure 6.28: Waves expressed by a function $F(x) = 1 - C_1 \cos(k_1 x) - C_2 \cos(k_2 x)$. The parameters are chosen as $C_1 = 0.5$, $C_2 = 0.2$, $k_1 = 2\pi$, and $k_2 = k_1/2 + \varepsilon$, where ε is (a) 0.0 and (b) $k_1/38$. Broken lines show following functions: (a) $g_1(x) = 1 - C_1 \cos(k_1 x)$ and $g_2(x) = 1 - C_2 \cos(k_2 x)$; (b) $h_1(x) = 1 + C_1 + C_2 \sin(\varepsilon x)$, $h_2(x) = 1 + C_1 - C_2 \sin(\varepsilon x)$, $h_3(x) = 1 - C_1 - C_2 \cos(\varepsilon x)$, and $h_4(x) = 1 - C_1 + C_2 \cos(\varepsilon x)$.

117

and

$$F(x) = 1 - C_1 + C_2 \cos(\varepsilon x) \quad \text{for } x = \frac{2\pi}{k_1} \cdot (2n + 1). \qquad (6.18)$$

Similar equations are obtained for local maxima

$$F(x) = 1 + C_1 - C_2 \sin(\varepsilon x) \quad \text{for } x = \frac{2\pi}{k_1} \cdot (2n + \frac{1}{2}), \qquad (6.19)$$

and

$$F(x) = 1 + C_1 + C_2 \sin(\varepsilon x) \quad \text{for } x = \frac{2\pi}{k_1} \cdot (2n + \frac{3}{2}). \qquad (6.20)$$

These four waves are envelope curves of the composite wave as shown in Fig. 6.28(b). Therefore, eq. (6.14) can be interpreted as that the local maxima and minima of the wave shown in Fig. 6.28(a) are modulated with a long wave length of $2\pi/\varepsilon$ with different phases. Since brightest spots, i.e., the maximum points are observed in STM, two waves with about twice period of $2\pi/k_1$ and with the long period of $2\pi/\varepsilon$ are simultaneously observed in STM. This explains the structure with two periods observed in the STM image of the monolayer graphite on TiC(111) surface. Generally, modulated structures would be observed in STM when lattices of overlayers and substrates are mismatched. But, the STM images show various patterns, and interpretation of them is not simple, as demonstrated here.

6.6   Summary

The electronic structure of the monolayer graphite on TiC(111) surface has been studied by the first-principles band calculations. The occupied π bands of the graphite layer are similar to those of the bulk graphite. The K point which is the original Fermi level in the bulk graphite is lowered by about 2 eV below the Fermi level. The unoccupied π^* bands are drastically deformed from those of the bulk. This has been explained by hybridization of the π orbitals of the graphite with the d orbitals of the substrate Ti layer. The calculated band dispersion reproduces well the experimental ARUPS spectrum.

The electronic charge at each site has been calculated, which shows no charge transfer between the graphite layer and the substrate. The lowering

of the π bands has been explained by the change of electronic occupation in the graphite layer from the occupied σ and π states to the unoccupied π^* states due to hybridization with the substrate. The present mechanism explains the anomalous expansion of the lattice constant of the monolayer graphite. The obtained results do not depend on the lateral position of the monolayer graphite relative to the substrate. This has been explained by the averaging effect in the lattice-mismatched system.

The STM images has been calculated with the results of the first-principles band calculations. The calculated images show the 2×2 superstructure of the graphite lattice, which explains the superstructure with the shorter period observed in the STM. The calculated STM images depend on the lateral position of the monolayer graphite relative to the substrate, which indirectly explained the superstructure with the longer period.

To discuss the superstructure with the longer period, tight-binding calculations have been performed based on the results of the first-principles calculations. The calculated STM images show two periods which reproduce the features observed in the experimental STM. The condition for the appearance of the superstructure has been discussed, where it has been found that three factors are important, that is, (1) strength of interaction between the overlayer and the substrate, (2) distance between the tip and the surface, and (3) bias voltage which reflects the energy region where bands of the overlayer and the substrate are strongly mixed.

In this study, the distance between the graphite layer and the substrate has not been determined by the first-principles total energy calculation. This should be performed in future. The unit cell used in the first-principles band calculation has been small. For more precise discussion, it would be desirable to use a more large unit cell. It would be useful also in discussing the moiré patterns which have been calculated by the tight-banding model in this study.

Present work could be extended to investigations of the electronic structure of the monolayer graphite on other metal substrates such as TiC(110), TaC(111), and Pt(111) surface. This is important to know general natures of the monolayer graphite on metal substrates. First-principles calcula-

tion of the phonon structure of the monolayer graphite on the substrates is interesting to clarify the mechanism of the softening observed in the experimental phonon dispersion. The discussion of the moiré structure in the STM should be extended to other surfaces of layered materials such as $MoSe_2$ layers on MoS_2 substrate, where the moiré pattern is observed even when more than five overlayers are accumulated[85].

Chapter 7

Conclusion

In this thesis, a method of calculation for STM images and STS spectra has been developed based on the first-principles calculations of the electronic structures for the sample surface and the tip. This method has been applied to the graphite surface and the $Si(111)\sqrt{3} \times \sqrt{3}$-B surface, and it has been found that the effect of the tip is important in explaining various STM images and STS spectra observed on these surfaces.

The STM image of the graphite surface has been calculated with various models for the tip. First, a H_2 molecule has been used as a model of the tip. In the case of the bonding orbital of the tip, the obtained STM image has been a normal one consisting of a triangular lattice, which is similar to the LDOS image of the surface. In the case of the anti-bonding orbital of the tip, however, the STM images show anomalous structures. By an analytical calculation, it has been proved that these anomalous images are caused by the interference effect of the wavefunctions of the surface and the tip. More realistic calculations have been performed using the $W_{10}[111]$ cluster model for the tip. The calculated image also has shown the anomalous structures when the tunnel-active orbital of the tip has no $d_{3z^2-r^2}$ component. The most plausible origin for the anomalous images is the nodal structure of the wavefunctions of such tips as $W_{13}[110]$ without the apex atom. The STS spectra of the graphite surface also have been calculated with various models for the tip. The calculated STS spectra depend sensitively on the atomic structure of the tip apex.

The method of calculation of the STM and STS has been applied to the

Si(111)$\sqrt{3} \times \sqrt{3}$-B/defect surface. The NDR in the STS of the Si(111)$\sqrt{3} \times \sqrt{3}$-B/defect surface has been reproduced by the calculation using the realistic cluster model for the tip. It has been found that the appearance of the NDR depends crucially on the electronic structure around the apex of the tip and that a favorable condition for the appearance of the NDR is a presence of both a localized state for the sample surface and a tunnel-active orbital for the tip near the Fermi level. This condition has been satisfied for the $W_{10}[111]$ tip, but not for the $W_{14}[110]$ and the $Pt_{10}[111]$ tip. From the results of the present calculations, it has been concluded that the appearance of the NDR is not a special phenomenon limited to only the Si(111)$\sqrt{3} \times \sqrt{3}$-B surface. Exploring the NDR for other surfaces would be very important from view points of basic physics as well as application to micro-devices.

The electronic structure and the STM image of the monolayer graphite on TiC(111) surface have been studied by the first-principles band calculation. The calculated band structure reproduces well the experimental result. The calculated electronic charge shows no charge transfer between the graphite layer and the substrate. The obtained electronic structure has been explained by the change of electronic occupation in the graphite layer from the occupied σ and π states to the unoccupied π^* states due to the hybridization with the substrate. The present mechanism explains the anomalous expansion of the lattice constant of the monolayer graphite. The obtained results do not depend on the lateral position of the monolayer graphite relative to the substrate, which has been explained by the averaging effect in the lattice-mismatched system.

The STM images of the monolayer graphite on TiC(111) surface has been calculated with the results of the first-principles band calculations. The calculated images show the 2×2 structure of the graphite lattice, which explains the superstructure with the shorter period observed in the STM. The calculated STM images depend on the lateral position of the monolayer graphite relative to the substrate, which indirectly explained the superstructure with the longer period.

To discuss the superstructure with the longer period, tight-binding cal-

culations have been performed based on the results of the first-principles calculations. The calculated STM images reproduce the features observed in the experimental STM. It has been found that the appearance of the superstructure is governed by three factors, that is, the strength of the interaction between the overlayer and the substrate, the distance between the tip and the surface, and the bias voltage which reflects the energy region of the tunneling current where the bands of the overlayer and the substrate are strongly coupled. Present work should be extended to investigations of the STM image of the monolayer graphite on other metal substrates. The discussion of the moiré pattern in the STM could be extended to other surfaces of layered materials such as transition-metal dichalcogenides.

As mentioned in the introduction, nowadays it has become possible to modify various surfaces in atomic scale by using the STM tip. The STM is expected to continue to play an important role in surface physics, chemistry and technology as well as biology for finding new physical phenomenon, microfabrication, and development of new devices. For these purposes, theoretical support in both interpretations and predictions is indispensable. To treat complicated and large-scale systems consisting various kind of atoms with electronic field, electronic current, aqueous solution, photon, and so on, development of new theoretical formalisms as well as of computational algorithm and facilities is necessary, which should be achieved in future.

Appendix A

A derivation of eq. (2.12) is presented in this appendix. The surface integral of the matrix element in eq. (2.8) is transformed into a volume integral in the tip region Ω_T as

$$M_{\mu\nu} = \frac{\hbar^2}{2m} \int_{\Omega_T} d\mathbf{r} (\psi_\mu^* \bigtriangleup \psi_\nu - \psi_\nu \bigtriangleup \psi_\mu^*). \tag{A.1}$$

Using schrödinger equations for the surface and tip expressed as

$$-\frac{\hbar^2}{2m} \bigtriangleup \psi_\mu + V_S \psi_\mu = E_\mu \psi_\mu, \tag{A.2}$$

$$-\frac{\hbar^2}{2m} \bigtriangleup \psi_\nu + V_T \psi_\nu = E_\nu \psi_\nu, \tag{A.3}$$

and the condition of energy conservation

$$E_\mu - E_\nu + eV = 0, \tag{A.4}$$

the tunneling matrix element is expressed as

$$M_{\mu\nu} = \int_{\Omega_T} d\mathbf{r} \psi_\mu^* (V_T - V_S - eV) \psi_\nu \tag{A.5}$$

$$\simeq \int_{\Omega_T} d\mathbf{r} \psi_\mu^* V_T \psi_\nu. \tag{A.6}$$

The last approximation is justified taking them into account that V_S is negligibly small in the tip region and that the bias voltage in usual STM experiments also is negligibly small comparing with the tip potential. By expanding the wavefunctions of surface and tip in terms of atomic orbitals shown in eqs. (2.10) and (2.11), the tunneling matrix element is rewritten as

$$|M_{\mu\nu}|^2 = \sum_{ii'} \sum_{jj'} \sum_{pp'} \sum_{qq'} a_{ip}^{\mu*} a_{i'p'}^{\mu} a_{j'q'}^{\mu*} a_{jq}^{\mu} C_{ipjq} C_{i'p'j'q'}^*. \tag{A.7}$$

125

Using the definition of Green's functions shown in eqs. (2.13) and (2.14), the tunneling current is expressed as eq. (2.12).

Appendix B

A derivation of eq. (4.3) is shown in this appendix. The wavefunction and potential of the H_2 tip are expressed respectively as

$$\psi_{\mathrm{T}} = \frac{1}{\sqrt{2}}[\phi(\mathbf{r} - \mathbf{r}_0 - \frac{\mathbf{d}}{2}) \pm \phi(\mathbf{r} - \mathbf{r}_0 + \frac{\mathbf{d}}{2})], \tag{B.1}$$

$$V_{\mathrm{T}} = V_0(\mathbf{r} - \mathbf{r}_0 - \frac{\mathbf{d}}{2}) + V_0(\mathbf{r} - \mathbf{r}_0 + \frac{\mathbf{d}}{2}), \tag{B.2}$$

where $\phi(\mathbf{r})$ and $V_0(\mathbf{r})$ are the $1s$ orbital and potential of hydrogen atom, respectively. The vectors $\mathbf{r}_0$ and $\mathbf{d}$ are center of the two hydrogens and displacement of a hydrogen measured from the other one, respectively. The sign $+$ and $-$ denote the bonding and anti-bonding orbital of H_2 molecule, respectively. In the above, the potential of the H_2 molecule is approximated by superposition of potentials of the hydrogen atom. By expanding the surface wavefunction as shown in eq. (4.1), the tunneling matrix element is calculated as

$$M = \int_{\Omega_{\mathrm{T}}} d\mathbf{r}\, \psi_{\mathrm{S}} V_{\mathrm{T}} \psi_{\mathrm{T}} \tag{B.3}$$

$$\simeq \frac{1}{\sqrt{2}} \sum_{\mathbf{G}_\parallel} F(\mathbf{k}_\parallel + \mathbf{G}_\parallel) A(\mathbf{G}_\parallel) \tag{B.4}$$

$$\times [e^{i(\mathbf{k}_\parallel + \mathbf{G}_\parallel)\cdot(\mathbf{r}_{0\parallel} + \frac{\mathbf{d}_\parallel}{2})} \pm e^{i(\mathbf{k}_\parallel + \mathbf{G}_\parallel)\cdot(\mathbf{r}_{0\parallel} - \frac{\mathbf{d}_\parallel}{2})}], \tag{B.5}$$

where

$$F(\mathbf{q}_\parallel) \equiv \int d\mathbf{r}\, e^{i\mathbf{q}_\parallel \cdot \mathbf{r}_\parallel} V_0(\mathbf{r})\phi(\mathbf{r}). \tag{B.6}$$

In the above, the cross terms of the atomic orbital and potential are neglected, because they are small compared with the on-site terms. Using

eq. B.5, the tunneling current is expressed as

$$I \propto |M|^2 \tag{B.7}$$

$$= I_S(\mathbf{r}_{0\parallel}, \mathbf{d}_\parallel) \pm I_T(\mathbf{r}_{0\parallel}, \mathbf{d}_\parallel), \tag{B.8}$$

where

$$I_S(\mathbf{r}_{0\parallel}, \mathbf{d}_\parallel) \equiv \sum_{\mathbf{G}_\parallel, \mathbf{G}'_\parallel} F(\mathbf{k}_\parallel + \mathbf{G}_\parallel) F(\mathbf{k}_\parallel + \mathbf{G}'_\parallel) A(\mathbf{G}_\parallel) A(\mathbf{G}'_\parallel) \tag{B.9}$$

$$\times e^{i(\mathbf{G}_\parallel - \mathbf{G}'_\parallel) \cdot \mathbf{r}_{0\parallel}} \cos[(\mathbf{G}_\parallel - \mathbf{G}'_\parallel) \cdot \frac{\mathbf{d}_\parallel}{2}], \tag{B.10}$$

$$I_T(\mathbf{r}_{0\parallel}, \mathbf{d}_\parallel) \equiv \sum_{\mathbf{G}_\parallel, \mathbf{G}'_\parallel} F(\mathbf{k}_\parallel + \mathbf{G}_\parallel) F(\mathbf{k}_\parallel + \mathbf{G}'_\parallel) A(\mathbf{G}_\parallel) A(\mathbf{G}'_\parallel) \tag{B.11}$$

$$\times e^{i(\mathbf{G}_\parallel - \mathbf{G}'_\parallel) \cdot \mathbf{r}_{0\parallel}} \cos[(2\mathbf{k}_\parallel + \mathbf{G}_\parallel + \mathbf{G}'_\parallel) \cdot \frac{\mathbf{d}_\parallel}{2}]. \tag{B.12}$$

The term I_S is expressed as

$$I_S(\mathbf{r}_{0\parallel}, \mathbf{d}_\parallel) = \frac{1}{2}[I^0(\mathbf{r}_{0\parallel} + \frac{\mathbf{d}_\parallel}{2}) + I^0(\mathbf{r}_{0\parallel} - \frac{\mathbf{d}_\parallel}{2})], \tag{B.13}$$

in terms of the tunneling current I^0 defined as

$$I^0(\mathbf{r}_\parallel) \equiv \sum_{\mathbf{G}_\parallel, \mathbf{G}'_\parallel} F(\mathbf{k}_\parallel + \mathbf{G})_\parallel F(\mathbf{k}_\parallel + \mathbf{G}'_\parallel) A(\mathbf{G}_\parallel) A(\mathbf{G}'_\parallel) e^{i(\mathbf{G}_\parallel - \mathbf{G}'_\parallel) \cdot \mathbf{r}_\parallel}, \tag{B.14}$$

which is the expression of tunneling current for a single atom tip. Therefore, the term I_S is a simple sum of the contributions from each atom of H_2 molecule. The term I_T expresses interference of the tip and surface wavefunctions.

If the two-dimensional primitive lattice vectors of graphite are taken as

$$\mathbf{R}_{1\parallel} = a(\frac{\sqrt{3}}{2}, \frac{1}{2}), \tag{B.15}$$

$$\mathbf{R}_{2\parallel} = a(\frac{\sqrt{3}}{2}, -\frac{1}{2}), \tag{B.16}$$

the primitive reciprocal lattice vectors are given as

$$\mathbf{G}_{1\parallel} = g(\frac{1}{2}, \frac{\sqrt{3}}{2}), \tag{B.17}$$

$$\mathbf{G}_{2\parallel} = g(\frac{1}{2}, -\frac{\sqrt{3}}{2}), \tag{B.18}$$

$$g \equiv \frac{4\pi}{\sqrt{3}a}, \tag{B.19}$$

where a is the lattice constant of graphite. The Fermi energy of graphite is located at K points of Brillouin zone, and the wavefunction is composed of C $2p_z$ orbital ($z \perp$ surface). Since the $2p_z$ orbital is symmetric around the z axis and

$$A(\mathbf{G}_\parallel) \propto \int e^{-i(\mathbf{k}_\parallel + \mathbf{G}_\parallel) \cdot \mathbf{r}_\parallel} \phi_{2p_z}(\mathbf{r}) d\mathbf{r}, \tag{B.20}$$

the quantity $A(\mathbf{G}_\parallel)$ is a function of only $|\mathbf{k}_\parallel + \mathbf{G}_\parallel|$. When a K point

$$\mathbf{k}_\parallel = g(\frac{1}{2}, \frac{\sqrt{3}}{6}), \tag{B.21}$$

is chosen, absolute values of the three vectors given by eq. (4.2) are the same. Since $V_0(\mathbf{r})$ and $\phi(\mathbf{r})$ for a hydrogen atom are spherically symmetric, the quantity $F(\mathbf{q}_\parallel)$ in eq. (B.6) is also a function of $|\mathbf{q}_\parallel|$. Therefore, if all reciprocal vectors are neglected except for those given by eq. (4.2), the tunneling current is expressed as

$$I_S(\mathbf{r}_{0\parallel}, \mathbf{d}_\parallel) = F^2 A^2 \sum_{\mathbf{G}_\parallel, \mathbf{G}'_\parallel} e^{i(\mathbf{G}_\parallel - \mathbf{G}'_\parallel) \cdot \mathbf{r}_{0\parallel}} \cos[(\mathbf{G}_\parallel - \mathbf{G}'_\parallel) \cdot \frac{\mathbf{d}_\parallel}{2}], \tag{B.22}$$

$$I_T(\mathbf{r}_{0\parallel}, \mathbf{d}_\parallel) = F^2 A^2 \sum_{\mathbf{G}_\parallel, \mathbf{G}'_\parallel} e^{i(\mathbf{G}_\parallel - \mathbf{G}'_\parallel) \cdot \mathbf{r}_{0\parallel}} \tag{B.23}$$

$$\times \cos[(2\mathbf{k}_\parallel + \mathbf{G}_\parallel + \mathbf{G}'_\parallel) \cdot \frac{\mathbf{d}_\parallel}{2}], \tag{B.24}$$

which is shown to be equivalent with eq. (4.3) by substituting the three reciprocal vectors of eq. (4.2). Even if other equivalent K points are chosen instead of one shown in eq. (B.21), the result is the same.

Bibliography

[1] G. Binnig, H. Rohrer, Ch. Gerber, and E. Weibel, Phys. Rev. Lett. **49**, 57 (1982).

[2] G. Binnig, H. Rohrer, Ch. Gerber, and E. Weibel, Phys. Rev. Lett. **50**, 120 (1983).

[3] K. Takayanagi, Y. Tanishiro, M. Takahashi, and S. Takahashi, Surf. Sci. **164**, 367 (1985).

[4] R. M. Tromp, R. J. Hamers, and J. E. Demuth, Phys. Rev. **34**, 1388 (1986).

[5] P. Hansma and J. Tersoff, J. Appl. Phys. **61**, R1 (1987).

[6] For reviews of recent progress, see proceedings of International Conference of STM published in following journals; J. Vac. Sci. Technol. A**8** (1990) and B**9** (1991), Ultramicroscopy **42-44** (1992).

[7] R. J. Hamers, Ph. Avouris, and F. Bozso, Phys. Rev. Lett. **59**, 2071 (1987).

[8] R. Wolkow and Ph. Avouris, Phys. Rev. Lett. **60**, 1049 (1988).

[9] Ph. Avouris and R. Wolkow, Phys. Rev. B**39**, 5091 (1989).

[10] Ph. Avouris, In-Whan Lyo, F. Bozso, and E. Kaxiras, J. Vac. Sci. Technol. A**8**, 3405 (1990).

[11] In-Whan Lyo and Ph. Avouris, J. Chem. Phys. **93**, 4479 (1990).

[12] Ph. Avouris and In-Whan Lyo, Surf. Sci. **242**, 1 (1991).

[13] Ph. Avouris, In-Whan Lyo, and F. Bozso, J. Vac. Sci. Technol. B**9**, 424 (1991).

[14] A. J. Hoeven, J. M. Lenssinck, D. Dijkamp, ijk, E. J. van Loenen, and J. Dieleman, Phys. Rev. Lett. **63**, 1830 (1989).

[15] Y.-W. Mo, B. S. Swartzentruber, R. Kariotis, M. B. Webb, and M. G. Lagally, Phys. Rev. Lett. **63**, 2393 (1989).

[16] B. S. Swartzentruber, Y.-W. Mo, M. G. Lagally, and M. B. Webb, Phys. Rev. Lett. **65**, 1913 (1990).

[17] E. Ganz, S. K. Theiss, I.-S. Hwang, J. Golovchenko, Phys. Rev. Lett. **68**, 1567 (1992).

[18] H. J. W. Zandvliet, H. B. Elswijk, E. J. van Loenen, and D. Dijkamp, Phys. Rev. B**45**, 5965 (1992).

[19] H. J. W. Zandvliet, H. B. Elswijk, and E. J. van Loenen, Surf. Sci. **272**, 264 (1992).

[20] Sang-il Park and C. F. Quate, Appl. Phys. Lett. **48**, 112 (1986).

[21] R. Sonnenfeld and P. K. Hansma, Science **232**, 211 (1986).

[22] K. Sashikata, N. Furuya, and K. Itaya, J. Vac. Sci. Technol. B**9**, 457 (1991).

[23] T. P. Beebe, T. E. Wilson, D. F. Ogletree, J. E. Katz, R. Balhorn, M. B. Salmeron, and W. J. Siekhaus, Science **243**, 370 (1989).

[24] P. G. Arscott, G. Lee, V. A. Bloomfield, and D. F. Evans, Nature **339**, 484 (1989).

[25] S. M. Lindsay, T. Thundat, L. A. Nagahara, U. Knipping, and R. L. Rill, Science **244**, 1063 (1989).

[26] D. D. Dunlap and C. Bustamante, Nature **342**, 204 (1989).

[27] A. Cricenti, S. Selici, A. C. Felici, R. Generosi, E. Gori, W. Djaczenko, and G. Chiarotti, Science **245**, 1266 (1989).

[28] R. J. Driscoll, M. G. Youngquist, and J. D. Baldeschwieler, Nature **346**, 294 (1990).

[29] G. Binnig, C. F. Quate, and Ch. Gerber, Phys. Rev. Lett. **56**, 930 (1986).

[30] J. H. Coombs, J. K. Gimzewski, B. Reihl, J. K. Sass, and R. R. Schlittler, J. Microscopy **152**, 325 (1988).

[31] M. Tsukada, T. Schimizu, and K. Kobayashi, Ultramicroscopy **42-44**, 360 (1992).

[32] T. Schimizu, K. Kobayashi, and M. Tsukada, Appl. Surf. Sci. **60/61**, 454 (1992).

[33] M. Völcker, W. Krieger, T. Suzuki, and H. Walther, J. Vac. Sci. Technol. B**9**, 541 (1991).

[34] K. Kobayashi, T. Suzuki, and M. Tsukada, Surf. Sci. **285**, 181 (1993).

[35] D. M. Eigler and E. K. Schweizer, Nature **344**, 524 (1990).

[36] D. M. Eigler, C. P. Lutz, and W. E. Rudge, Nature **352**, 600 (1991).

[37] J. A. Stroscio, D. M. Eigler, Science **254**, 1319 (1991).

[38] D. M. Eigler, P. S. Weiss, E. K. Schweizer, and N. D. Lang, Phys. Rev. Lett. **66**, 1189 (1991).

[39] In-Whan Lyo and Ph. Avouris, Science **253**, 173 (1991).

[40] Ph. Avouris and In-Whan Lyo, Appl. Surf. Sci. **60/61**, 426 (1992).

[41] Y. Hasegawa and Ph. Avouris, Science **258**, 1763 (1992).

[42] S. Hosoki, S. Hosaka, T. Hasegawa, Appl. Surf. Sci. **60/61**, 643 (1992).

[43] H. Uchida, D. Huang, F. Grey, and M. Aono, Phys. Rev. Lett. **70**, 2040 (1993).

[44] H. Uchida, D. H. Huang, J. Yoshinobu, and M. Aono, Surf. Sci. **287**, 1056 (1993).

[45] J. Tersoff and D. R. Hamann, Phys. Rev. Lett. **50**, 1998 (1983); Phys. Rev. B**31**, 805 (1985).

[46] A. Selloni, P. Carnevali, E. Tosatti, and C. D. Chen, Phys. Rev. B**31**, 2602 (1985).

[47] D. Tománek, S. G. Louie, H. J. Mamin, D. W. Abraham, E. Ganz, R. E. Thomson, and J. Clarke, Phys. Rev. B**35**, 7790 (1987).

[48] D. Tománek and S. G. Louie, Phys. Rev. B**37**, 8327 (1988).

[49] D. Lawunmi and M. C. Payne, J. Phys. Condens. Matter **2**, 3811 (1990).

[50] Y. G. Ding, C. T. Chan, and K. M. Ho, Phys. Rev. Lett. **67**, 1454 (1991).

[51] S. Watanabe, M. Aono, M. Tsukada, Phys. Rev. B**44**, 8330 (1991).

[52] N. D. Lang, Phys. Rev. Lett. **55**, 230 (1985).

[53] N. D. Lang, Phys. Rev. Lett. **56**, 1164 (1986).

[54] N. D. Lang, Phys. Rev. B**34**, 5947 (1986).

[55] N. D. Lang, Phys. Rev. Lett. **58**, 45 (1987).

[56] N. D. Lang, Phys. Rev. B**36**, 8173 (1987).

[57] N. D. Lang, Phys. Rev. B**37**, 10395 (1988).

[58] N. D. Lang, Comments Condens. Matter Phys. **14**, 253 (1989).

[59] C. J. Chen, J. Vac. Sci. Technol. A**6**, 319 (1988).

[60] C. J. Chen, Phys. Rev. B**42**, 8841 (1990).

[61] C. J. Chen, Phys. Rev. Lett. **65**, 448 (1990).

[62] C. J. Chen, Phys. Rev. Lett. **69**, 1656 (1992).

[63] S. Ciraci and I. P. Batra, Phys. Rev. B**36**, 6194 (1987).

[64] I. P. Batra, S. Ciraci, J. Vac. Sci. Technol. A**6**, 313 (1988).

[65] S. Ciraci, A. Baratoff, I. P. Batra, Phys. Rev. B**41**, 2763 (1990).

[66] S. Ciraci, A. Baratoff, I. P. Batra, Phys. Rev. B**42**, 7618 (1990).

[67] K. Kobayashi and M. Tsukada, J. Phys. Soc. Jpn. **58**, 2238 (1989).

[68] K. Kobayashi, N. Isshiki, and M. Tsukada, Solid State Commun. **74**, 1187 (1990).

[69] M. Tsukada, K. Kobayashi, and S. Ohnishi, J. Vac. Sci. Technol. A**8**, 160 (1990).

[70] K. Kobayashi and M. Tsukada, J. Vac. Sci. Technol. A**8**, 170 (1990).

[71] N. Isshiki, K. Kobayashi, and M. Tsukada, Surf. Sci. **238**, L439 (1990); J. Vac. Sci. Technol. B**9**, 475 (1991).

[72] M. Tsukada, K. Kobayashi, and N. Isshiki, Surf. Sci. **242**, 12 (1991).

[73] M. Tsukada, K. Kobayashi, N. Shima, and N. Isshiki, J. Vac. Sci. Technol. B**9**, 492 (1991).

[74] M. Tsukada, K. Kobayashi, N. Isshiki, and H. Kageshima, Surf. Sci. Rep. **13**, 265 (1991).

[75] In-Whan Lyo and Ph. Avouris, Science **245**, 1369 (1989).

[76] P. Bedrossian, D. M. Chen, K. Mortensen, and J. A. Golovchenko, Nature **342**, 258 (1989).

[77] W. Mizutani, M. Shigeno, M. Ono, and K. Kajimura, Appl. Phys. Lett. **56**, 1974 (1990).

[78] M. Tsukada, T. Schimizu, S. Watanabe, N. Isshiki, and K. Kobayashi, Jpn. J. Appl. Phys. **32**, 1352 (1993).

[79] M. Weimer, J. Kramar, C. Bai, and J. D. Baldeschwieler, Phys. Rev. B**37**, 4292 (1988).

[80] T. R. Coley, W. A. Goddard III, J. D. Baldeschwieler, J. Vac. Sci. Technol. B**9**, 470 (1991).

[81] X. Qin and G. Kirczenow, Phys. Rev. B**39**, 6245 (1989).

[82] S. P. Kelty and C. M. Lieber, Phys. Rev. B**40**, 5856 (1989).

[83] C. H. Olk, J. Heremans, M. S. Dresselhaus, J. S. Speck, and J. T. Nicholls, Phys. Rev. B**42**, 7524 (1990).

[84] H. Itoh, T. Ichinose, C. Oshima, and T. Ichinokawa, Surf. Sci. **254**, L437 (1991).

[85] B. A. Parkinson, F. S. Ohuchi, K. Ueno, and A. Koma, Appl. Phys. Lett. **58**, 472 (1991).

[86] T. Mori, K. Saiki, and A. Koma, Jpn. J. Appl. Phys. **31**, L1370 (1992).

[87] T. Mori, H. Abe, K. Saiki, and A. Koma, Jpn. J. Appl. Phys. **32**, 2945 (1993).

[88] J. Bardeen, Phys. Rev. Lett. **6**, 57 (1961).

[89] M. Tsukada and N. Shima, J. Phys. Soc. Jpn. **56**, 2875 (1987).

[90] M. Tsukada, H. Kageshima, N. Isshiki, and K. Kobayashi, Surf. Sci. **266**, 253 (1992).

[91] H. Kageshima and M. Tsukada, Phys. Rev. B**46**, 6928 (1992).

[92] N. D. Lang, A. Yacoby, and Y. Imry, Phys. Rev. Lett. **63**, 1499 (1989).

[93] J. Tersoff and N. D. Lang, Phys. Rev. Lett. **65**, 1132 (1990).

[94] N. D. Lang, Phys. Rev. B**45**, 13599 (1992).

[95] N. D. Lang, Solid State Commun. **84**, 155 (1992).

[96] U. Landman, W. D. Luedtke, N. A. Burnham, and R. J. Colton, Science **248**, 454 (1990).

[97] U. Landman and W. D. Luedtke, J. Vac. Sci. Technol B**9**, 414 (1991).

[98] S. Ciraci, E. Tekman, A. Baratoff, and I. P. Batra, Phys. Rev. B**46**, 10411 (1992).

[99] J. C. Slater, T. M. Wilson, and J. H. Wood, Phys. Rev. **179**, 29 (1969).

[100] R. Srinivasan and G. Lakshmi, Surf. Sci. **43**, 617 (1974).

[101] A. Zunger and A. J. Freeman, Phys. Rev. B**15**, 4716 (1977).

[102] M. Tsukada, H. Adachi, and C. Satoko, Prog. Surf. Sci. **14**, 113 (1983).

[103] P. Hohenberg and W. Kohn, Phys. Rev. **136**, B864 (1964).

[104] W. Kohn and L. J. Sham, Phys. Rev. **140**, A1133 (1965).

[105] G. Binnig, H. Fuchs, Ch. Gerber, H. Rohrer, E. Stoll, and E. Tosatti, Europhysics, Lett. **1**, 31 (1986).

[106] S. A. C. Gould, K. Burke, P. K. Hansma, Phys. Rev. B**40**, 5363 (1989).

[107] G. S. Painter and D. E. Ellis, Phys. Rev. B**1**, 4747 (1970).

[108] A. Zunger, Phys. Rev. B**17**, 626 (1978).

[109] R. C. Tatar and S. Rabii, Phys. Rev. B**25**, 4126 (1982).

[110] N. A. W. Holzwarth, S. G. Louie, and S. Rabii, Phys. Rev. B**26**, 5382 (1982).

[111] J. W. McClure, Phys. Rev. **119**, 606 (1960).

[112] M. P. Sharma, L. G. Johnson, and J. W. McClure, Phys. Rev. B**9**, 2467 (1974).

[113] K. Kobayashi and M. Tsukada, Phys. Rev. B**35**, 2963 (1987).

[114] J. Tersoff, Phys. Rev. Lett. **57**, 440 (1986).

[115] J. M. Soler, A. M. Baro, N. Garcia, and H. Rohrer, Phys. Rev. Lett. **57**, 444 (1986).

[116] H. J. Mamin, E. Ganz, D. W. Abraham, R. E. Thomson, and J. Clarke, Phys. Rev. B**34**, 9015 (1986).

[117] K. Sattler, Int. J. Mod. Phys. B**6**, 3603 (1992).

[118] M. Kuwabara, D. R. Clarke, and D. A. Smith, Appl. Phys. Lett. **56**, 2396 (1990).

[119] H. A. Mizes and W. A. Harrison, J. Vac. Sci. Technol. A**6**, 300 (1988).

[120] T. R. Albrecht, H. A. Mizes, J. Nogami, Sang-il Park, and C. F. Quate, Appl. Phys. Lett. **52**, 362 (1988).

[121] K. Kobayashi, Phys. Rev. B**48**, 1757 (1993).

[122] H. A. Mizes, Sang-il Park, and W. A. Harrison, Phys. Rev. B**36**, 4491 (1987).

[123] Sang-il Park, J. Nogami, and C. F. Quate, Phys. Rev. B**36**, 2863 (1987).

[124] Sang-il Park, J. Nogami, H. A. Mizes, and C. F. Quate, Phys. Rev. B**38**, 4269 (1988).

[125] R. J. Colton, S. M. Baker, R. J. Driscoll, M. G. Youngquist, J. D. Baldeschwieler, and W. J. Kaiser, J. Vac. Sci. Technol. A**6**, 349 (1988).

[126] T. Sakurai, T. Hashizume, I. Kamiya, Y. Hasegawa, T. Ide, M. Miyao, I. Sumita, A. Sakai, and S. Hyodo, J. Vac. Sci. Technol. A, **7**, 1684 (1989).

[127] T. Hashizume, Y. Hasegawa, I. Kamiya, T. Ide, I. Sumita, S. Hyodo, T. Sakurai, H. Tochihara, M. Kubota, and Y. Murata, J. Vac. Sci. Technol. A, **8**, 233 (1990).

[128] P. J. Feibelman, Phys. Rev. B**35**, 2626 (1987).

[129] A. A. Lucas, H. Morawitz, G. R. Henry, J.-P. Vigneron, Ph. Lambin, P. H. Culter, and T. E. Feuchtwang, Phys. Rev. B**37**, 10708 (1988).

[130] W. Mizutani, M. Shigeno, K. Saito, N. Morita, T. Yoshioka, M. Ono, and K. Kajimura, J. Microscopy **152**, 547 (1988).

[131] P. Bedrossian, R. D. Meade, K. Mortensen, D. M. Chen, J. A. Golovchenko, and D. Vanderbilt, Phys. Rev. Lett. **63**, 1257 (1989).

[132] In-Whan Lyo, E. Kaxiras, and Ph. Avouris, Phys. Rev. Lett. **63**, 1261 (1989).

[133] E. Kaxiras, K. C. Pandey, F. J. Himpsel, and R. M. Tromp, Phys. Rev. B**41**, 1262 (1990).

[134] R. L. Headrick, I. K. Robinson, E. Vlieg, and L. C. Feldman, Phys. Rev. Lett. **63**, 1253 (1989).

[135] H. Huang, S. Y. Tong, J. Quinn, and F. Jona, Phys. Rev. B**41**, 3276 (1990).

[136] T. A. Land, T. Michely, R. J. Behm, J. C. Hemminger, and G. Comsa, Surf. Sci. **264**, 261 (1992); J. Chem. Phys. **97**, 6774 (1992).

[137] A. Ya. Tontegode, Prog. Surf. Sci. **38**, 201 (1991).

[138] M. S. Dresselhaus and G. Dresselhaus, Adv. Phys. **30**, 139 (1981).

[139] R. Rosei, M. De Crescenzi, F. Sette, C. Quaresima, A. Savoia, and P. Perfetti, Phys. Rev. B**28**, 1161 (1983).

[140] Hu Zi-pu, D. F. Ogletree, M. A. van Hove, and G. A. Somorjai, Surf. Sci. **180**, 433 (1987).

[141] C. F. McConville and D. P. Woodruff, Surf. Sci. **171**, L447 (1986).

[142] J. Nakamura, H. Hirano, M. Xie, I. Matsuo, T. Yamada, and K. Tanaka, Surf. Sci. **222**, L809 (1989).

[143] R. W. Joyner and G. R. Darling, Surf. Sci. **205**, 513 (1988).

[144] G. R. Darling, J. B. Pendry, and R. W. Joyner, Surf. Sci. **221**, 69 (1989).

[145] T. Aizawa, R. Souda, S. Otani, Y. Ishizawa, and C. Oshima, Phys. Rev. Lett. **64**, 768 (1990); Phys. Rev. B**42**, 11469 (1990).

[146] T. Aizawa, R. Souda, Y. Ishizawa, H. Hirano, T. Yamada, and K. Tanaka, Surf. Sci. **237**, 194 (1990).

[147] T. Aizawa, Y. Hwang, W. Hayami, R. Souda, S. Otani, and Y. Ishizawa, Surf. Sci. **260**, 311 (1992).

[148] Y. Hwang, T. Aizawa, W. Hayami, S. Otani, Y. Ishizawa, and S. J. Park, Solid State Commun. **81**, 397 (1992).

[149] Y. Hwang, T. Aizawa, W. Hayami, S. Otani, and Y. Ishizawa, Surf. Sci. **271**, 299 (1992).

[150] K. Yamamoto, M. Fukushima, T. Osaka, and C. Oshima, Phys. Rev. B**45**, 11358 (1992).

[151] C. T. Chen, W. A. Kamitakahara, K. M. Ho, and P. C. Eklund, Phys. Rev. Lett. **58**, 1528 (1987).

[152] A. Fujimori, F. Minami, and N. Tsuda, Surf. Sci. **121**, 199 (1982).

[153] M. Tsukada and T. Hoshino, J. Phys. Soc. Jpn. **51**, 2562 (1982).

[154] T. Hoshino and M. Tsukada, J. Mag. and Mag. Materials **31-34**, 901 (1983).

[155] A. Nagashima, K. Nuka, H. Itoh, T. Ichinokawa, C. Oshima, and S. Otani, Surf. Sci. **291**, 93 (1993).

[156] A. Nagashima, K. Nuka, H. Itoh, T. Ichinokawa, C. Oshima, S. Otani, and Y. Ishizawa, Solid State Commun. **83**, 581 (1992).

[157] K. Kobayashi, Y. Souzu, N. Isshiki, and M. Tsukada, Appl. Surf. Sci. **60/61**, 443 (1992).

[158] J. B. Sokoloff, Phys. Rep. **126**, 189 (1985).

[159] T. Janssen and A. Janner, Adv. Phys. **36**, 519 (1987).

[160] C. de Lange and T. Janssen, Phys. Rev. B**28**, 195 (1983); Physica **127A**, 125 (1984).

[161] R. Haydock, V. Heine, and M. J. Kelly, J. Phys. C **5**, 2845 (1972).

[162] V. Heine, R. Haydock, and M. J. Kelly, *Solid State Physics* vol. 35 (1980) (Academic, New York).

[163] D. R. Hamann, M. Schlüter, and C. Chiang, Phys. Rev. Lett. **43**, 1494 (1979).

[164] G. B. Bachelet, D. R. Hamann, and M. Schlüter, Phys. Rev. B**26**, 4199 (1982).

[165] R. S. Mulliken, J. Chem. Phys. **23**, 1841 (1955).

[166] G. Blyholder, J. Phys. Chem. **68**, 2772 (1964).

[167] G. Doyen and G. Ertl, Surf. Sci. **43**, 197 (1974).

[168] H. Ishida, Phys. Rev. B**38**, 8006 (1988).

[169] H. Ohtani, R. J. Wilson, S. Chiang, and C. M. Mate, Phys. Rev. Lett. **60**, 2398 (1988).

[170] M. Tsukada, N. Shima, S Ohnishi, and Y. Chiba, J. Phys. Colloq. **48**, C6-91 (1987).

[171] S. Ohnishi and M. Tsukada, Solid State Commun. **71**, 391 (1989).

[172] A. J. Fisher and P. E. Blöchl, Phys. Rev. Lett. **70**, 3263 (1993).

[173] M. Tsukada, T. Schimizu, S. Watanabe, N. Isshiki, and K. Kobayashi, Jpn. J. Appl. Phys. **32**, 1352 (1993).

[174] A. P. Smith and N. W. Ashcroft, Phys. Rev. Lett. **59**, 1365 (1987).

[175] T. Fujiwara and T. Yokokawa, Phys. Rev. Lett. **66**, 333 (1991).